

# **Design and Analysis of Microwave Devices Based on Gap Waveguide Technology**

**Mohamed Abdelaziz Mohamed Abdelaal**

A Thesis  
in  
The Department  
of  
Electrical and Computer Engineering

Presented in Partial Fulfillment of the Requirements  
For the Degree of  
Doctor of Philosophy (Electrical and Computer Engineering) at  
Concordia University  
Montréal, Québec, Canada

December 2018

**©Mohamed Abdelaziz Mohamed Abdelaal, 2018**

# **CONCORDIA UNIVERSITY**

## **SCHOOL OF GRADUATE STUDIES**

This is to certify that the thesis prepared

By: Mohamed Abdelaziz Mohamed Abdelaal

Entitled: Design and Analysis of Microwave Devices Based on Gap  
Waveguide Technology

and submitted in partial fulfillment of the requirements for the degree of

Doctor of Philosophy (Electrical and Computer Engineering)

complies with the regulations of this University and meets the accepted standards with respect to originality and quality.

Signed by the final examining committee:

Chair

Dr. Govind Gopakumar

External Examiner

Dr. Pedram Mousavi

External to Program

Dr. Amr Yousef

Examiner

Dr. Tayeb A. Denidni

Examiner

Dr. Christopher W. Trueman

Thesis Supervisor

Dr. Ahmed A. Kishk

Approved by: \_\_\_\_\_

Dr. Mustafa K. Mehmet Ali, Graduate Program Director

December 17, 2018 \_\_\_\_\_

Dr. Amir Asif, Dean

Gina Cody School of Engineering and Computer Science

# Abstract

Design and Analysis of Microwave Devices Based on Gap Waveguide Technology

Mohamed Abdelaziz Mohamed Abdelaal, Ph.D.  
Concordia University, 2018

Among state-of-the-art guiding structures, the Ridge Gap Waveguide (RGW) is a promising technology, as it minimizes the losses in high-frequency applications and supports wide operating bandwidth. There is another form of the guiding structures that utilize the idea of the Artificial Magnetic Conductor (AMC) surfaces such as Groove Gap Waveguide (GGWG). It has the same advantages as the RGW in terms of losses, and immunity to leakages without the need for electrical contacts, but with different dispersion characteristics. The RGW supports a quasi-TEM mode while the GGWG supports TE modes as it's a different form of the rectangular waveguide. Therefore, GGWG has high power capability comparable to the standard waveguides. As currently, interest is increasing of millimeter wave and microwave applications, the RGW and GGWG are excellent candidates for these applications due to their low loss. It is quite essential to develop microwave components with superior electrical characteristics for such applications.

The anisotropic materials have useful physical properties that can benefit the microwave devices, due to their enormous advantages such as high stability and wide bandwidth in the millimeter wave band. Ferrite is an example of such anisotropic materials. Their properties can be deployed to improve the performance of the millimeter microwave devices in terms of higher stability, wider band, and high power handling.

Taking advantages of the above characteristics, the research work in this thesis is focusing on their use for microwave and millimeter wave frequencies. The presented devices are responsible for the feeding of the antenna systems. Moreover, they can be deployed in different applications such as antenna beamforming. In this thesis, the differential phase shifters and the orthomode transducers (OMTs) are realized by different technologies that are suitable for both of the microwave and the millimeter wave bands that serve different applications of the wireless communication systems.

The research work done can also be summarized in two parts. The first part starts with the study and investigation of the ferrite material properties and their role in the microwave

devices. Then, later providing a new accurate model with mathematical formulas for the differential ferrite phase shifter. Moreover, a new design methodology for those phase shifters is presented. Later, the ferrite is applied in the conventional waveguide, Substrate Integrated Waveguide (SIW), and RGW technologies.

In the second part, study, design, and analysis of different types of the orthomode transducers are presented. They are devices responsible for combining and separation of two orthogonal polarizations. The presented OMTs has a compact size with excellent performance. Several OMT types are considered such as the one-fold symmetry, asymmetric, and two-fold symmetry. The first mentioned two OMTs are realized by deploying the waveguide technology, while the two-fold symmetry OMT is based on the GGWG technology. It has the ability to design a feeding network for an array of antennas based on the GGWG technology. Moreover, this OMT is fabricated using 3D printed technology that uses the carbonated plastic material, in which two copper layers are covering all the structure surfaces by electroplating. This fabrication is a new promising technology that is not expensive, lightweight and less complex than traditional machining. However, there are some concerns about power handling and high temperature withstanding. Such problems might have a solution in the future with a more accurate 3D metallic printers.

# Acknowledgments

I would like to express my sincere gratitude to my supervisor, Dr. Ahmed A. Kishk for his guidance, patience and invaluable comments. Thanks are also due to Dr. Christopher W. Trueman, Dr. Tayeb A. Denidni, and Dr. Amr Yousef for their valuable comments and for serving in my examining committee. Also, I would like to thank the external examiner Dr. Pedram Mousavi and all the committee members.

I would also like to thank Dr. Mohamed Hassan, Dr. Shokry Shamseldin, Concordia University technical staff, Mr. Jeffrey Landry, and Mr. Vincent Mooney-Chopin for their assistance to build and measure some of the presented prototypes in this work.

Lastly, I offer my love, regards, and blessings to my father, my mother, my sister, and my brothers for their unlimited support during the compilation of this work.

*To my parents*

# Contents

<b>List of Figures</b>	<b>x</b>
<b>List of Tables</b>	<b>xiv</b>
<b>List of Acronyms</b>	<b>xv</b>
<b>List of Symbols</b>	<b>xvi</b>
<b>Chapter 1 Introduction</b>	<b>1</b>
1.1 Historical Overview of Guiding Structures . . . . .	1
1.1.1 Basic Idea of Conventional Guiding Structures . . . . .	2
1.1.2 Guiding Structures Based on New Technologies . . . . .	2
1.2 Motivations . . . . .	2
1.3 Objectives . . . . .	3
1.4 Thesis Outlines . . . . .	4
<b>Chapter 2 Literature Review</b>	<b>6</b>
2.1 Substrate Integrated Waveguide . . . . .	6
2.2 Ridge Gap Waveguide . . . . .	7
2.3 Groove Gap Waveguide . . . . .	10
2.4 Brief Review of Some Essential Microwave Components and Devices . . . . .	11
2.4.1 Power Dividers . . . . .	11
2.4.2 Couplers . . . . .	11
2.4.3 Phase Shifters . . . . .	12
2.4.4 Orthomode Transducer . . . . .	13
<b>Chapter 3 Investigation and Analysis of Ferrite Material</b>	<b>15</b>
3.1 Rectangular Waveguide Differential Phase Shifter Based on Horizontal Ferrite Tiles: Accurate Model for Full-band Operation . . . . .	17
3.1.1 Ferrite Differential Phase Shifter Configuration Description . . . . .	17
3.1.2 Traditional Design Methodology Limitations . . . . .	19
3.1.3 Proposed Model . . . . .	20
3.1.3.1 Homogeneous Case Transcendental Equation . . . . .	21
3.1.3.2 In-homogeneous Case Adjustment . . . . .	25
3.1.4 Validation and Experimental Results . . . . .	27
3.2 Compact Ultra-Flat RGW Differential Phase Shifter for Millimeter-Wave Applications . . . . .	36
3.2.1 Ferrite Slab Operation . . . . .	36
3.2.2 RGW Differential Phase Shifter Design . . . . .	37

3.2.2.1	Unit Cell Design . . . . .	37
3.2.2.2	RGW DPS Configuration . . . . .	39
3.3	90° Phase Shifter Based on Substrate Integrated Waveguide Technology for Ku-band Applications . . . . .	40
3.3.1	SIW Phase Shifter Configuration . . . . .	40
3.3.2	Ku-Band Phase Shifter Example . . . . .	40
3.4	Circularly Polarized RGW Slot Antenna Fed by Ferrite Based Phase Shifter . . . . .	43
3.4.1	Ferrite Based RGW Differential Phase Shifter . . . . .	44
3.4.2	Circularly Polarized Antenna Design . . . . .	45
<b>Chapter 4</b>	<b>Design and Analysis of Orthomode Transducers</b>	<b>47</b>
4.1	Compact Full Band OMT Based on Dual Mode Double Ridge Waveguide . . . . .	48
4.1.1	OMT Design Concept . . . . .	49
4.1.1.1	Design Interfaces . . . . .	49
4.1.1.2	Double Ridge Waveguide Modal Analysis . . . . .	50
4.1.2	OMT Design Description . . . . .	51
4.1.2.1	OMT Core . . . . .	52
4.1.2.2	Assembly Elements . . . . .	53
4.1.2.3	Entire OMT . . . . .	54
4.1.3	Validation and Experimental Results . . . . .	57
4.1.4	Higher Frequency bands Validation . . . . .	59
4.2	Asymmetric Compact OMT . . . . .	61
4.2.1	Physical Alignment of OMT Ports . . . . .	61
4.2.2	Combined OMT Design Methodology . . . . .	62
4.2.2.1	OMT Description . . . . .	63
4.2.2.2	Offset OMT Design . . . . .	64
4.2.3	Validation and Experimental Results . . . . .	67
4.2.3.1	Back-to-Back . . . . .	68
4.2.3.2	Back-to-Back with 90° . . . . .	69
4.2.3.3	Non-standard Matched Load . . . . .	69
4.2.4	Evaluation of Proposed OMT . . . . .	70
4.2.5	Validation at 30 GHz Band . . . . .	72
4.3	3D-Printed Wideband Groove Gap Waveguide Orthomode Transducer . . . . .	75
4.3.1	Orthomode Transducer Core . . . . .	75
4.3.1.1	Proposed GGWG Transmission Line . . . . .	75
4.3.1.2	OMT Core Structure . . . . .	76
4.3.2	Assembly Elements . . . . .	77
4.3.2.1	GGWG to WR-28 Power Combiner and Transition . . . . .	77
4.3.2.2	GGWG to GGWG Multilayer Transition . . . . .	80
4.3.3	Overall OMT Structure . . . . .	80
4.3.4	Evaluation of Proposed GGWG OMT . . . . .	83
4.3.5	Fabrication and Measurements . . . . .	85

<b>Chapter 5 Conclusions and Future Work</b>	<b>89</b>
5.1 Conclusions . . . . .	89
5.2 Main Contributions . . . . .	91
5.2.1 Non-reciprocal Microwave Devices . . . . .	91
5.2.2 Reciprocal Microwave Devices . . . . .	92
5.3 Suggested Future Work . . . . .	92
<b>Bibliography</b>	<b>93</b>
<b>List of Publications</b>	<b>104</b>
<b>Appendices</b>	<b>106</b>
<b>Appendix A Ferrite Material Selection Criteria</b>	<b>107</b>
<b>Appendix B Mathematical Formulation of Dual Mode Double Ridge Waveguide OMT</b>	<b>109</b>
B.1 Square Waveguide Impedance Calculations . . . . .	109
B.2 Double Ridge Waveguide Impedance Calculations . . . . .	110

# List of Figures

2.1	Geometry of SIW line example and the signal propagation illustration. . . . .	7
2.2	Soft-hard surface ideal realization with respect to the wave propagation direction [15]. . . . .	8
2.3	Geometry of the nail unit cell example. . . . .	8
2.4	RGW one-row geometry and the signal propagation illustration. . . . .	9
2.5	RGW one-row propagating modes and its band gap. . . . .	9
2.6	GGWG one-row geometry and the signal propagation illustration. . . . .	10
2.7	GGWG one-row propagating modes and its band gap. . . . .	10
3.1	Ferrite slab internal and external fields. . . . .	16
3.2	Each channel of the ferrite differential phase shifter is deploying. (a) One vertical tile. (b) Two horizontal tiles. . . . .	19
3.3	Each channel of the ferrite differential phase shifter. (a) Actual structure. (b) Effective model. . . . .	22
3.4	Ferrite material distribution. (a) Four tiles. (b) Eight tiles.(c) Simulation results comparison (WR-650, $4\pi M_s = 300$ G, $H_0 = 120$ Oe, $\frac{\Delta S}{S} = 0.075$ ). . . . .	23
3.5	The effective model parameters in the case of WR-650 ( $4\pi M_s = 300$ G, $H_0 = 120$ Oe, $\frac{\Delta S}{S} = 0.075$ , $Fr_{asr} = 7$ ). (a) $\frac{\mu}{\mu_0}$ . (b) $\frac{\kappa}{\kappa_0}$ . (c) $\frac{\epsilon}{\epsilon_0}$ . . . . .	28
3.6	The effective model parameters in the case of WR-90 ( $4\pi M_s = 1880$ G, $H_0 = 752$ Oe, $\frac{\Delta S}{S} = 0.075$ , $Fr_{asr} = 7$ ). (a) $\frac{\mu}{\mu_0}$ . (b) $\frac{\kappa}{\kappa_0}$ . (c) $\frac{\epsilon}{\epsilon_0}$ . . . . .	29
3.7	The effective model parameters in the case of WR-28 ( $4\pi M_s = 6000$ G, $H_0 = 2400$ Oe, $\frac{\Delta S}{S} = 0.075$ , $Fr_{asr} = 7$ ). (a) $\frac{\mu}{\mu_0}$ . (b) $\frac{\kappa}{\kappa_0}$ . (c) $\frac{\epsilon}{\epsilon_0}$ . . . . .	30
3.8	$\beta \times \lambda_0$ components for WR-650 ( $4\pi M_s = 300$ G, $H_0 = 120$ Oe, $\frac{\Delta S}{S} = 0.075$ , $Fr_{asr} = 7$ ). (a) $\beta + \times \lambda_0$ and $\beta - \times \lambda_0$ . (b) $\Delta\beta \times \lambda_0$ . . . . .	31
3.9	Comparing proposed inhomogeneous. model with CST and Approx. model (WR-650, $4\pi M_s = 300$ G, $H_0 = 120$ Oe). (a) $\frac{\Delta S}{S} = 0.01$ , $Fr_{asr} = 5$ . (b) $\frac{\Delta S}{S} = 0.01$ , $Fr_{asr} = 7$ . (c) $\frac{\Delta S}{S} = 0.075$ , $Fr_{asr} = 5$ . (d) $\frac{\Delta S}{S} = 0.075$ , $Fr_{asr} = 7$ . . . . .	32
3.10	Comparing proposed inhomogeneous. model with CST and Approx. model (WR-90, $4\pi M_s = 1880$ G, $H_0 = 752$ Oe). (a) $\frac{\Delta S}{S} = 0.01$ , $Fr_{asr} = 5$ . (b) $\frac{\Delta S}{S} = 0.01$ , $Fr_{asr} = 7$ . (c) $\frac{\Delta S}{S} = 0.075$ , $Fr_{asr} = 5$ . (d) $\frac{\Delta S}{S} = 0.075$ , $Fr_{asr} = 7$ . . . . .	33
3.11	Comparing proposed inhomogeneous. model with CST and Approx. model (WR-28, $4\pi M_s = 6000$ G, $H_0 = 2400$ Oe). (a) $\frac{\Delta S}{S} = 0.01$ , $Fr_{asr} = 5$ . (b) $\frac{\Delta S}{S} = 0.01$ , $Fr_{asr} = 7$ . (c) $\frac{\Delta S}{S} = 0.075$ , $Fr_{asr} = 5$ . (d) $\frac{\Delta S}{S} = 0.075$ , $Fr_{asr} = 7$ . . . . .	34
3.12	Proposed inhomogeneous model percentage error as a function of $\frac{\Delta S}{S}$ and $Fr_{asr}$ . . . . .	34

3.13	Fabricated example. (a) Measurement setup. (b) Measured differential phase shift (dotted red) comparison with simulations (solid line: $\pm 10\%$ Tolerance: green, $\pm 7.5\%$ Tolerance: magenta, and $\pm 5\%$ Tolerance: cyan), approximate model (dashed black) and proposed model (dash-dotted blue). (c) S-parameters magnitudes simulation and measurement comparison. . . . .	35
3.14	Geometry of the nail unit cell. . . . .	37
3.15	RGW propagating modes and its band gap. . . . .	37
3.16	RGW differential phase shifter geometry. . . . .	38
3.17	Differential phase between the outputs of the proposed RGW DPS channels outputs. . . . .	38
3.18	Matching and transmission coefficients of the proposed RGW DPS. . . . .	38
3.19	SIW phase shifter geometry. . . . .	40
3.20	Differential phase between the two channels outputs. . . . .	41
3.21	Matching and transmission coefficients of the proposed phase shifter. . . . .	41
3.22	The geometry of the proposed antenna (Top ground is hidden). . . . .	44
3.23	Simulations of the RGW power divider connected to the differential phase shifter. (a) Matching and insertion loss. (b) Differential phase shift between the two channels outputs. . . . .	45
3.24	Simulations of the proposed antenna (Reflection coefficient magnitude and axial ratio). . . . .	46
3.25	Simulations of the proposed antenna (Radiation pattern at 30 GHz). . . . .	46
4.1	Block diagram for the proposed OMT. . . . .	49
4.2	The proposed OMT interface section configuration. (a) Square waveguide cross section. (b) Dual-mode double ridge waveguide cross section. . . . .	49
4.3	Proposed OMT interface section configuration. (a) Dispersion diagram of the dual-band double ridge waveguide. (b) Field mode patterns of the modes propagating within the operating bandwidth. . . . .	51
4.4	The proposed OMT 3D. (a) Vertical sectional view. (b) Horizontal sectional view with port numbers indicated. . . . .	52
4.5	The proposed OMT matching and transmission simulation results. . . . .	53
4.6	Assembly elements response. (a) Space eliminator and a power combiner. (b) 90° bend section. (c) Circular to the square waveguide. . . . .	54
4.7	OMT theoretical maximum power simulation results. (a) Standard rectangular waveguide WR-51. (b) Standard circular waveguide K1. (c) Whole OMT. . .	55
4.8	Whole OMT. (a) Vertical sectional view with port numbers indicated. (b) Horizontal Sectional view with port numbers indicated. (c) 3D structure with dimensions. (d) Simulation results. . . . .	56
4.9	OMT back-to-back setup with port numbers. (a) Without rotation angle. (b) With 90° rotation angle. . . . .	58
4.10	Proposed OMT Parts. (a) 3D view. (b) Top view. (c) After assembly. . . . .	58
4.11	OMT results using back-to-back setup. (a) Simulations and measurements without rotation angle (matching and insertion loss). (b) Simulations and measurements with 90° rotation angle (matching and insertion loss). (c) Simulations with 90° rotation angle (measured far coupling). . . . .	59

4.12	Proposed OMT at 30 GHz band. (a) Structure 3D sectional views with port numbering. (b) Dimensions of the 3D structure. (c) Simulation results. . . . .	60
4.13	Traditional OMT structure. (a) Side view of V-Pol. inline. (b) Side view of H-Pol. inline. (c) Plane view of Non-inline. . . . .	61
4.14	Bends sectional view. (a) E-plane. (b) H-plane. (c) E- and H-plane. . . . .	62
4.15	Block diagram of the proposed OMT methodology. . . . .	63
4.16	The proposed OMT without offset. (a) 3D horizontal sectional view. (b) Plane horizontal sectional view. (c) Simulation results. . . . .	64
4.17	The proposed OMT with offset. (a) 3D horizontal sectional view. (b) Plane horizontal sectional view. (c) Simulation results. . . . .	65
4.18	Comparison between the simulated isolation level of OMT with and without offset. . . . .	66
4.19	Fabricated OMT. (a) 3D view. (b) Sectional view. (c) Measurement setup of the back-to-back setup. . . . .	67
4.20	Simulated and measured S-parameters of the proposed OMT with an offset in back-to-back setup. (a) Reflection and transmission coefficients. (b) Isolation coefficients. . . . .	68
4.21	Simulated and measured S-parameters of the proposed OMT with an offset in a back-to-back setup with 90° rotation. (a) Reflection and transmission coefficients. (b) Isolation coefficients. . . . .	69
4.22	Designed matching load. (a) Sectional view of the fabricated prototype and its simulation results. (b) Connected to the OMT measured results (m) compared to simulation results (s). . . . .	70
4.23	Presented OMT at 30 GHz band. (a) Structure 3D sectional views with port numbering. (b) Dimensions of the OMT structure. (c) Simulation results. . . . .	74
4.24	GGWG structure. (a) 3D view (Top conducting cover is hidden). (b) GGWG cross-section with the geometrical parameters. (c) Reflection and transmission coefficients. (d) Dispersion diagram. . . . .	76
4.25	Block diagram of the proposed OMT. . . . .	77
4.26	Proposed OMT core, numbers are for ports. (a) 3D view. (b) Side cross-sectional view across Port 1, 3, and 5 on Plane A. (c) Planar view with top metallic cover and circular waveguide are removed. . . . .	78
4.27	Simulated results of the proposed OMT core. . . . .	79
4.28	GGWG to WR-28 power combiner and transition with port numbers. (a) 3D view of half the structure. (b) Front view. (c) Planar view with the top removed and the red rectangle indicating the position of the rectangular waveguide. . . . .	80
4.29	GGWG to WR-28 power combiner and transition simulation results. (a) Reflection and Transmission coefficients, indicating equal power division. (b) Phase indicating Port 1 and 2 are out of phase. (c) Magnetic field distribution at 30 GHz on the horizontal plane cut. . . . .	81
4.30	Transition between two stacked GGWG. (a) 3D view with the Top removed. (b) Cross-section on Plane B. (c) Cross-section on Plane A. . . . .	82
4.31	Transition between two GGWG layers simulation results (matching and insertion loss). . . . .	82

4.32 Simulation results of the overall OMT excited through the common port (m1 : mode 1, m2 : mode 2). . . . .	83
4.33 Photos of the Fabricated OMT different parts. (a) Lower part. (b) Middle part. (c) Top part. (d) Assembled OMT. . . . .	86
4.34 OMT back-to-back setup with port numbers. (a) Without rotation. (b) With 90° rotation angle. . . . .	86
4.35 (a) OMT back-to-back measurements setup. (b) WR-28 calibration kit and transitions. . . . .	87
4.36 OMT simulation and measurement results using a back-to-back setup. (a) Without rotation (matching and insertion loss). (b) With 90° rotation angle (matching and insertion loss). (c) Isolation coefficient magnitudes. . . . .	88
A.1 Normalized phase constant vs. frequency of ferrite sample ( $4\pi M_s = 300$ G, and $H_0 = 120$ Oe). . . . .	108

# List of Tables

3.1	Comparison Between Differential Phase Shifters Techniques. . . . .	19
3.2	Correction Factor Equation Constants. . . . .	27
4.1	Double Ridge Waveguide Dimensions. . . . .	50
4.2	Matching Transformers Dimensions. . . . .	52
4.3	Proposed OMT Dimensions. . . . .	66
4.4	Comparing the proposed OMT with different classes. . . . .	71
4.5	Comparing the proposed OMT with asymmetric OMTs. . . . .	72
4.6	Turnstile Dimensions. . . . .	79
4.7	Proposed OMT evaluation and comparison. . . . .	84

# List of Acronyms

<b>1G</b>	First Generation Network
<b>2G</b>	Second Generation Network
<b>3G</b>	Third Generation Network
<b>3GPP</b>	3G Partnership Project
<b>4G</b>	Fourth Generation Network
<b>5G</b>	Fifth Generation Network
<b>AMC</b>	Artificial Magnetic Conductor
<b>BDMA</b>	Beam Division Multiple Access
<b>CST</b>	Computer Simulation Technology Simulator
<b>DPS</b>	Differential Phase Shifter
<b>DRW</b>	Double Ridge Waveguide
<b>GGWG</b>	Groove Gap Waveguide
<b>GSM</b>	Global Systems for Mobile communications
<b>HFSS</b>	High Frequency Structure Simulator
<b>LTE</b>	Long Term Evolution
<b>OMT</b>	Orthomode Transducer
<b>PEC</b>	Perfect Electric Conductor
<b>PMC</b>	Perfect Magnetic Conductor
<b>RGW</b>	Ridge Gap Waveguide
<b>SIW</b>	Substrate Integrated Waveguide
<b>TE</b>	Transverse Electric
<b>TEM</b>	Transverse Electric Magnetic
<b>TM</b>	Transverse Magnetic
<b>WiMAX</b>	Mobile Worldwide Interoperability for Microwave Access

# List of Symbols

$\beta_0$	The propagation constant of the air filled guide
$\frac{\Delta S}{S}$	The ferrite filling factor
$\epsilon$	Permittivity
$\epsilon_r$	Relative permittivity of dielectric
$\epsilon_0$	Permittivity of free-space
$f_m$	The saturated magnetic frequency
$f_0$	The Larmor frequency
$\Omega$	Ohm
$\kappa, \mu$	The ferrite permeability tensor elements
$Z_0$	Characteristic impedance
$Z_{TE}$	Transverse electric wave impedance
$Z_{VI}$	Voltage current characteristic impedance
$Z_{PV}$	Power voltage characteristic impedance
$Z_{PI}$	Power current characteristic impedance
$\lambda$	Wavelength
$\lambda_0$	Free-space wavelength
$S$	S-parameter
$\Gamma$	Reflection coefficient

# Chapter 1

## Introduction

Wireless communication systems have been evolved from the first generation (1G) till the coming generation fifth generation (5G) [1–3]. Nowadays, the current generation of the cellular communication network (4G) will not be able to satisfy the rapid increase of the users' demands such as the capacity increase, improved data rate, decreased latency, and better quality of service. Therefore, the next generation of the communication system, 5G, aims to satisfy such demands by introducing improvements in the cellular network architecture.

5G will deploy the concept of the advanced access technology called Beam Division Multiple Access (BDMA). Such a concept can also be applied and deployed on other microwave wireless communication systems. In the BDMA, an orthogonal beam is allocated to each mobile station; the antenna beam will be divided according to the locations of the mobile stations. In other words, the antenna beam will follow the user, which will require a high gain scanning that will be based on the utilization of beamforming. This gives multiple accesses to the mobile stations, which increases the capacity of the system [4]. In addition to the above demands, there are other challenges such as massive device connectivity, reduced costs and consistent Quality of Experience provisioning [5].

### 1.1 Historical Overview of Guiding Structures

The most important and challenging area in microwave and millimeter wave region is the guiding structure in which the signal propagates. After Maxwell's equations, the basic idea of the guiding structures was discussed well [6, 7]. Moreover, solutions of many guiding structures are based on the wave equations that are obtained from the modified version of Maxwell's equation by Heinrich Hertz. These structures are many such as the parallel plate waveguide, rectangular waveguides, and circular waveguides [8].

### **1.1.1 Basic Idea of Conventional Guiding Structures**

Microwave signals can have a frequency range from 300 MHz to 300 GHz [8]. They are preferred to propagate as Transverse Electric Magnetic (TEM) waves by the guiding structure due to its advantages over TE and TM waves. The guided TEM waves are nondispersive with zero cutoff frequency. The guiding structure losses are directly proportional to the operating frequency. However, some guiding structures are low loss, such as the single conducting waveguides, which do not support a TEM wave, but rather a Transverse Electric (TE), Transverse Magnetic (TM) waves. For a single mode operation, waveguides have limited operating bandwidth with higher dispersion characteristics compared to the TEM guiding structures. However, the dominant mode of the waveguide could have a reasonably wideband that can reach 2:1, but practically the usable frequency range is usually less. Other waveguide structures such as the ridge waveguide have a much wider bandwidth.

### **1.1.2 Guiding Structures Based on New Technologies**

Recently, many guiding structures based on new technologies are introduced to replace the conventional ones. These structures are targeting mainly the high-frequency bands such as millimeter wave bands. The new technologies have many examples such as the Ridge Gap Waveguide (RGW), Groove Gap Waveguide (GGWG), and the Substrate Integrated Waveguide (SIW). More explanations and details about these technologies are presented in the next chapter. These guiding structures are yet to be standardized. The thesis focuses on RGW and GGGWG technologies due to their advantages over conventional types at the millimeter frequency bands. Later in the next chapter, more explanations regarding these technologies and the reasons for selecting them are presented. The motivations and objectives of this work are summarized in the following sections. At the end of this chapter, the outlines of the thesis are presented.

## **1.2 Motivations**

The demand for microwave devices with high performance is increasing exponentially due to the enormous upgrades required in the communication systems. Moreover, the demand for high data rates and better quality of service to serve users of the next fifth generation (5G) mobile communication system is increasing rapidly. 5G is targeting to reduce some of the limitations that exist in the current generation (4G). This needs developing new technologies able to solve some of the problems facing the microwave signals at the high-frequency bands such as the millimeter wave band.

The ridge gap waveguide is a promising structure for the high-frequency bands including the 5G network and other microwave communication systems since it minimizes the losses and dispersion problems, especially in the millimeter wave applications and is constructed without any need for any electrical contacts between its parts. Nevertheless, RGW structures have a high bandwidth ratio compared to the traditional waveguides. Although this technology is up-and-coming, it's still limited to the research work. RGWs are not competing actively yet with other technologies in the commercial market due to the need for some standardization. Moreover, they need to be easily integrated with other microwave components.

A similar concept to the RGW is the GGWG, which is similar in operation and characteristics to the rectangular waveguide. It is a rectangular waveguide without electrical contact with its top wall. It has some common properties with the RGW, as the guiding waveguide is surrounded by the band gap realized by the periodic cells, low losses, no leakage, and unnecessarily electrical contact. Moreover, the GGWG technologies can handle higher power, which is comparable to the standard waveguides.

The millimeter wave and microwave networks are expected to have enormous applications serving a huge number of users. Thus, the microwave devices in such networks need to be more efficient, and compact in order to make the size of the whole system more convenient. Moreover, not only the passive microwave devices need to be deployed in such a system, but also active microwave devices. Using such active devices will provide enhanced performance at the millimeter wave bands. An example of these active devices is the ferrite-based ones. Ferrite materials have enormous advantages over active elements in the millimeter wave band such as high stability and wide bandwidth. Nevertheless, only a few articles have addressed ferrite-based microwave components.

### 1.3 Objectives

This work introduces different types of microwave devices based on the technologies that deploy the Artificial Magnetic Conductor (AMC) surfaces such as the Ridge Gape Waveguide (RGW) and the Groove Gap Waveguide (GGWG). Such devices are suitable for the microwave and the millimeter wave applications. They should provide a wide operating bandwidth, which satisfies the requirements of such communication systems. The first part aims to study and investigate the ferrite materials and deploying them in the microwave devices to serve the targeted applications. Moreover, this work aims to build up equations that represent the performance of these materials in the conventional waveguides such as a rectangular waveguide. Then, use the gained experience to deploy the same idea in the AMC based guiding structures. Moreover, introducing a design methodology for such

materials to be deployed in the differential phase shifters. Such phase shifter is also realized by other technologies for the validation purposes of the idea.

The second part of this work aims to introduce microwave devices that can combine and separate two propagating polarizations such as Orthomode Transducers (OMTs). These devices maximize the use of the channel resources. The objective of this part is to improve the performance of the OMTs based on waveguide technology for high power applications by introducing a new design methodology. Another objective is to integrate the OMT with newer technologies such as GGWG technology. This integration facilitates the connection between the OMT and the other system components, and reduce the complexity of the overall system. Based on the authors' knowledge, no OMTs based on GGWG technology have been presented before in the literature.

## 1.4 Thesis Outlines

The thesis is organized into five chapters. The next chapter shows the literature review on the Substrate Integrated Waveguide (SIW), Ridge Gape Waveguide (RGW), and Groove Gap Waveguide (GGWG) technologies including their basic ideas. Moreover, how the unit cells are deployed to form an Artificial Magnetic Conductor (AMC) surface is presented. Nevertheless, reviews about some of the RGW and GGWG microwave devices are presented in the same chapter.

In chapter three, ferrite material and the associated design methodology are discussed. This chapter has three major parts. The first part introduces the analysis and investigation of ferrite materials and deploying them in microwave devices such as the differential phase shifter. Moreover, this part presents new equations that represent the response of such materials in the rectangular waveguide. The second part is using the gained experience in the first part to design differential phase shifters based on waveguide technology. The last part discusses the implementation of ferrite in the RGW and SIW to design differential phase shifters based on these technologies. Moreover, a circularly polarized antenna design deploying the differential phase shifter is presented as an application of such phase shifters.

Chapter four introduces passive devices responsible for separating and combining two orthogonally polarized signals that have the same frequency and sharing the same antenna. Such devices are the Orthomode Transducers (OMTs). New design methodologies to provide an improved design of the OMTs using waveguide technology are presented in the first part of this chapter. The size and performance of such OMTs are enhanced compared to the existing OMTs. Later, a new design of an OMT based on the GGWG technology is presented in the second part of this chapter, which is deployed for the first time in the OMT structures.

The last chapter presents conclusions, and future work that can benefit from this work is discussed in a separate section.

# Chapter 2

## Literature Review

The fifth generation, 5G, is the next communication system, which will offer a broad bandwidth that can provide high data rates. This will maximize the amount of data for transmission and reception compared to the current systems [9]. This will be done by the utilization of the millimeter wave band. The wavelengths of these waves are varying from 10 mm to 1 mm, which is corresponding to the frequency range of 30 to 300 GHz. The traditional guiding structures suffer from high losses in this frequency range. For example, the microstrip lines suffer from high radiation losses at this band, in addition to the dielectric losses. Therefore, the microstrip technology is not recommended or the millimeter wave bands; however, they support the Quasi-TEM mode.

In this chapter, a literature review of some examples of the recently introduced technologies, that overcome the problems of the traditional guiding structures of the 5G frequency band. Such examples include substrate integrated waveguides, ridge gap waveguides, and groove gap waveguides. Later, a brief review of some selected microwave components and devices that are essential in any communication system, such review includes their implementation technologies.

### 2.1 Substrate Integrated Waveguide

Rectangular waveguides are well-known structures that can handle high power with low losses compared to microstrip lines. Recently, Substrate Integrated Waveguide (SIW) technology became very popular as an integrated form of a rectangular waveguide. In other words, the SIW structure is the printed format of the rectangular waveguide. The side walls of the SIW are made of multiple vias that connects the upper and lower conductor forming a low-profile rectangular waveguide. This guiding structure supports a TE mode same as the traditional rectangular waveguide. The radiation losses of SIW are low compared to the microstrip line. Moreover, the fabrication of SIW is more comfortable than the traditional rectangular waveguides. SIW technology has the advantage of compatibility with the planar microwave

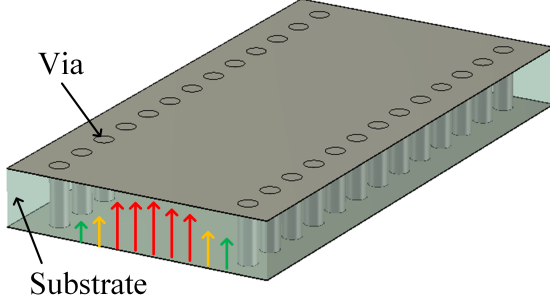


Figure 2.1: Geometry of SIW line example and the signal propagation illustration.

circuits and their fabrication cost are low [10]. Due to these advantages, the SIW technology is used in many microwave applications such as filters, couplers, and power dividers [11], [12]. This technology has also been deployed in antenna applications and its feeding structures [13]. The main disadvantages of SIW are the need of the substrate which contributes dielectric losses, and lower power handling since such a structure is low profile. An example of SIW line geometry is shown in Fig. 2.1.

## 2.2 Ridge Gap Waveguide

The Ridge Gap Waveguide (RGW) structure is very promising for the millimeter wave applications. This is because of its advantages over other structures, such as no dielectric losses, low radiation losses, and wideband operation. Since the RGW is an air-filled guiding structure, the dielectric loss is eliminated entirely. The RGW utilizes periodic cells to prevent the leakage out of the signal which minimizes the radiation losses. The RGW operating bandwidth depends mainly on the band gap of the unit cell, more details about these cells and how they are deployed will be presented in the next section. Later, some reviews about RGW based devices will be presented.

The Ridge gap waveguide structure was published by Kildal in 2009 [14]. This technology deploys the concept of the soft and the hard surface in a 2D periodicity [15]. This concept is simplified and shown in Fig. 2.2, the idea of this figure was introduced by [16], and its ideal implementation is by using PEC and PMC, their locations requirements with respect to the signal propagation are shown in the same figure as well. During the past few years, many articles have addressed this technology [17–19]. The idea is based on having quarter wavelength nails that form an AMC surface. A ground plane made of a conducting material is placed above these nails at a distance less than a quarter wavelength. A Perfect Electric Conductor (PEC) ridge is placed between these nails to form a guiding structure for the propagating signal. The closest ideal structure for this ridge gap waveguide is the parallel

plate structure.

Recently, RGWs have been considered as guiding structures for high-frequency applications. These guiding structures support Quasi TEM mode in the air gap between the ridge and the top round while the nails around the ridge prevent the leakage of the signal. Since the ridge gap waveguides are new structures, many studies are focusing on them due to their advantages. These guiding structures have lower losses since the signal is propagating inside the air region between the ridge and the top ground. In other words, ridge gap waveguides have lower losses than both microstrip lines and SIW since the signal in last mentioned structures pass through a dielectric substrate. Also, the electrical contacts between the upper and lower parts of the RGW structure are not needed. In the ridge gap waveguide technology, there are many possible components that can benefit from the use of ferrite material. Only a small number of published articles have addressed this topic.

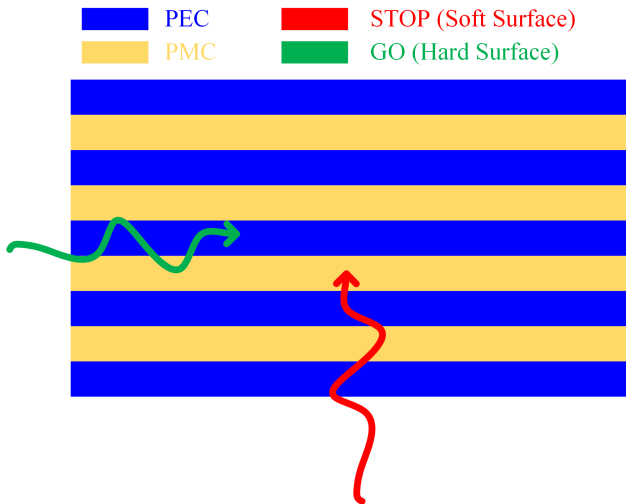


Figure 2.2: Soft-hard surface ideal realization with respect to the wave propagation direction [15].

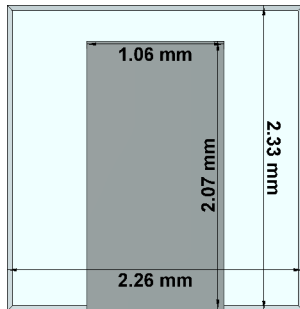


Figure 2.3: Geometry of the nail unit cell example.

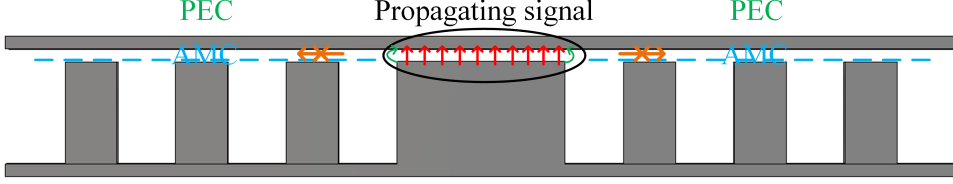


Figure 2.4: RGW one-row geometry and the signal propagation illustration.

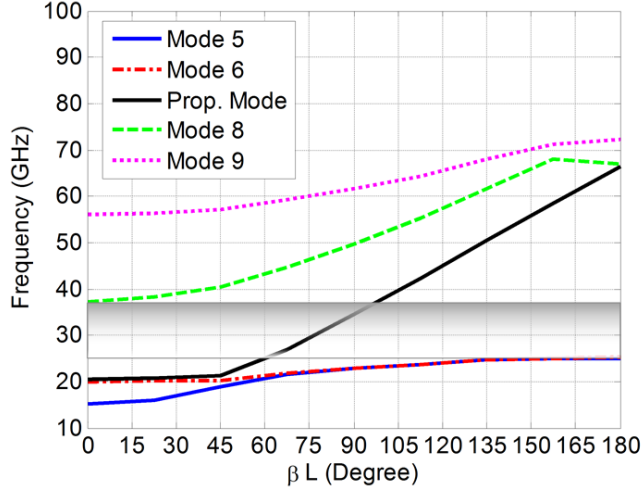


Figure 2.5: RGW one-row propagating modes and its band gap.

The primary element of RGW structures is the unit cell design that builds the AMC surface. The operating bandwidth of the RGW guiding structure is controlled by the stop band of the unit cell. A lot of research is done to introduce different unit cells of different shapes to widen the operating bandwidth [20, 21]. These cells can have many shapes to achieve the targeted band gap. The basic shape published is the nail with circular and rectangular cross-section area; such shape was called later by the bed nail unit cell. Other shapes were introduced to improve the operating band such as a pyramid shape and other shapes. As mentioned before the stop band of the unit cell which is equivalent also to the unit cell bandgap represents the bandwidth in which the structure inhibits the leakage outside the ridge. In other word, the stop band of the unit cell corresponds to the operating bandwidth of the whole ridge gap waveguide structure which is also known as the theoretical bandwidth.

An example of the nail unit cell with dimensions is shown in Fig. 2.3. Moreover, the geometry of one row utilizing the mentioned unit cell is shown in Fig. 2.4, while its bandgap and the propagating modes are shown in Fig. 2.5.

## 2.3 Groove Gap Waveguide

The Groove Gap Waveguide (GGWG) is another form of the guiding structures that use the soft and hard surfaces or in another word the AMC surface. In GGGW, the geometry of the RGW is the same except that the ridge is completely removed and replaced by a groove. The unit cells or pins are placed on both sides of the groove; such a structure is shown in Fig. 2.6. Moreover, an example of the propagating modes of the GGGW is presented in Fig. 2.7. The propagating mode of the GGGW is the TE/TM instead of the Quasi-TEM mode that propagates in the RGW. Thus the GGGW is operating close to the rectangular waveguides with an additional benefit of unnecessary of the electrical contact between the top and lower plates of the guide [22, 23]. In addition, the GGGW has fewer losses than the RGW since the volume or space left for the signal propagation is larger, this also increases the power capability of the GGGW compared with RGW. Thus the GGGW is recommended for the higher power applications that are working in the 5G frequency band.

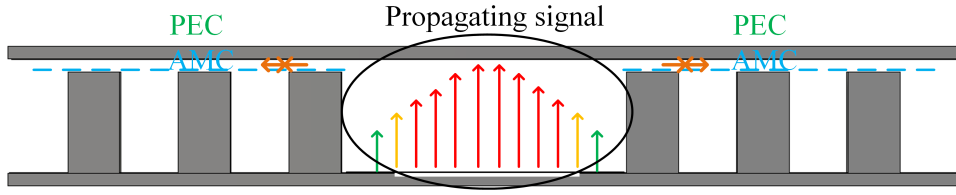


Figure 2.6: GGGW one-row geometry and the signal propagation illustration.

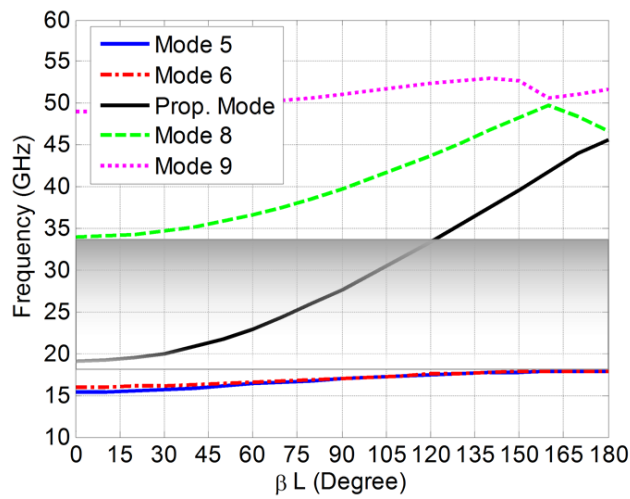


Figure 2.7: GGGW one-row propagating modes and its band gap.

## 2.4 Brief Review of Some Essential Microwave Components and Devices

Some essential microwave components and devices are discussed in the following subsections in brief to illustrate their progress in the recent era.

### 2.4.1 Power Dividers

The power divider is one of the most critical three port networks. It is used in many systems, mainly in the feeding structures of the antenna arrays. There are many configurations achieving equal or unequal power division with the same or different phase. Power dividers are reciprocal networks. Each configuration has a different use for some specific applications.

The RGWs based power dividers were presented by Kildal [24]. Here, only one type of power dividers was proposed which is the equal power with equal phase power divider. The presented device was a narrow band power divider. Many other RGW power dividers can be introduced such as the wideband dividers, the unequal power dividers and the series power dividers.

### 2.4.2 Couplers

One of the essential passive devices is the coupler. The coupler is a four passive port device that is reciprocal, internally matched, and lossless device. It is used to take a sample of the coupled port. Meanwhile, the rest of the signal is going out of the through port. The other two ports do not collect any power out of the input power. These two ports are called the input and the isolated ports. There are different types of the couplers based on the output phases of the signals at the coupled and the through ports. There are two types of couplers, the symmetric and the asymmetric. The case of having the same phase, at last, mentioned two ports is called the symmetric coupler while the case of having reversed phases of such ports is called the asymmetric coupler [8].

During the last decades, a lot of attention has been given to the couplers from the industry and research as well. The basic concepts of the couplers and their analysis were addressed in many publications [25, 26]. Many configurations of the hybrid coupler were introduced by scholars, such as the coupled line and branch lines [27]. Moreover, they were implemented by different technologies such as rectangular waveguides, stripline, and microstrip lines [28, 29].

Regarding the RGWs couplers, some trials were presented in [30]. Two different types of

the directional couplers were presented in that article. The first one was the hybrid coupler while the second was the coupled line directional coupler. They have a narrow bandwidth. However, they have proper matching and isolation levels. The isolation in both designs was around 24 dB. There is a need for more contributions to make the structure more compact couplers, also, to have a wide bandwidth.

### 2.4.3 Phase Shifters

The phase shifter can be deployed in 5G systems to facilitate beam scanning capability [31]. Moreover, another important application is utilizing them in the circularly polarized antenna systems [32–34]. There are many techniques to construct phase shifters, each of them has its own advantages over the others. Broadband phase shifters deploy the delay lines, but their drawback is a large size [35]. Meanwhile, active element based phase shifters have a compact size but at the expense of the operating bandwidth that is narrow [36,37]. In addition, active phase shifters do not affect well at high-frequency bands; especially, those deploy CMOS technology [38,39]. The anisotropic material based phase shifters show advantages over the other types as they can handle high power keeping the size compact. Moreover, they have a flat phase shift over the operating bandwidth.

The ferrite based phase shifters have been deployed in many systems before because of those advantages [40,41]. Nevertheless, the ferrite phase shifter is an essential component of other applications such as circulators, isolators, antenna beam scanning, switches, and duplexers [42,43]. Several technologies have been used for these phase shifters such as waveguide and substrate integrated waveguide [8,44].

Rectangular waveguides are well-known structures that can handle high power with low losses compared to microstrip lines. Many phase shifters based on rectangular waveguides were introduced in the literature [8], [45], and [46]. The main advantages of such components are the high-power handling capability and low losses. Nonreciprocal phase shifters are widely used in commercial high power four-port differential phase applications. The phase shifters in each waveguide are oppositely magnetized to produce the required differential phase shift between the two channels. A typical rectangular waveguide phase shifter consists of a rectangular waveguide with two or four ferrite tiles on its top and broad bottom walls magnetized perpendicular to the direction of propagation. It relies for its operation on the existence of natural planes of counter-rotating circularly polarized alternating magnetic fields on either side of its symmetry plane.

Recently, SIW technology became very popular as an integrated form of a rectangular waveguide. It has the advantages of the rectangular waveguide such as low losses and high-quality factor. Also, it is compatible with planar microwave circuits, and its fabrication

cost is low [10]. Due to these advantages, the SIW technology is used in many microwave applications such as filters, couplers, and power dividers [11], [12]. This technology has also been deployed in antenna applications and its feeding structures [13]. Moreover, the phase shifters have been implemented based on SIW technology through various configurations. One of the typical configurations builds on the periodic loading of the guiding structure to achieve the required phase shift [47], [48], and [49].

#### 2.4.4 Orthomode Transducer

One of the most commonly used solutions is the dual orthogonal polarizations to duplicate the channel capacity [50]. Thus, an orthomode transducer (OMT) device has to be exploited. Typically, an OMT is one of the essential components in antennas feeding systems; in particular for space applications. It is responsible for transmitting and /or receiving two orthogonal polarizations utilizing a conventional physical structure. Basically, OMTs are, physically, three-port passive devices: the common port and two single-mode ports. The common port carries the two degenerate orthogonal modes while the other two ports are, each, coupled to one of the degenerate modes in the common port. OMTs had been reported for the first time in 1956 by Tompkins [51]. The single polarization ports can be implemented with any technology such as microstrip lines [52], rectangular waveguides [53], and coaxial lines [54]. OMTs reduce the volume and mass of the feeding systems, which is very critical in satellite applications and radio astronomy systems [55, 56].

OMTs with waveguide junctions had been divided into three main groups, with one-fold symmetry, two-fold symmetry and asymmetric configuration [57–60]. The one-fold symmetry OMT structures were mainly based on the T-junctions, in which the horizontal polarization was guided through the lateral port, while the vertical polarization was directed to the other port [53, 61, 62] exploiting a differential feeding mechanism. This configuration was reversed in other designs [63, 64]. However, it occupied a large volume. This topology was further modified based on backward coupling structures with multi-hole coupling section to improve the bandwidth [65], but the overall size further increased.

The second configuration is the two-fold symmetry OMTs, which separated the two orthogonal modes and overcome the in-band higher order mode excitation as well [60]. OMTs with symmetrical structures are naturally having high isolation between orthogonal channels and wide operating bandwidth such as the Bøifot junction [60], and the turnstile junction [66–72]. These improvements are achieved at the expense of the high mechanical complexity and large size. Symmetric OMTs were implemented with fin-lines [73], ridge waveguides [54] and quad-ridged waveguides [74]. Nevertheless, the third topology was the asymmetric OMTs. This topology could provide orthogonal modes splitting in a very

compact size. However, they could only cover the narrow operating bandwidth to avoid the undesired coupling to the in-band higher order modes [75]. Moreover, the asymmetric configuration, in general, has a poor isolation level compared with the symmetric structures.

Based on the Authors' knowledge, the ridge gap waveguide differential phase shifters and the groove gap waveguide OMTs are not visited at all. As they are essential elements in many systems as explained before, so it is essential to design and test samples of these devices.

# Chapter 3

## Investigation and Analysis of Ferrite Material

Non-reciprocal microwave devices play an essential role in communication systems. There are various examples of such devices, such as isolators, circulators, and differential phase shifters. The non-reciprocal devices can be based on either an active component such as a diode or transistor, or ferrite material. The ferrite material has many leading advantages over the diodes and transistors such as the relatively high power capability and high-frequency operation. Ferrite material can work in the millimeter wave band with more stability than the diodes and transistors.

The direction of the propagating signal does indeed matter to the non-reciprocal devices such as the ferrite-based ones. For example, the ferrite-based isolator allows the signal to propagate in only one direction and pans the propagation in the opposite direction. On the other hand, devices that are based on isotropic dielectric material always have the same response regardless of the signal propagation direction.

The ferrite material needs an external magnetic field ( $H_a$ ) to be biased. Such a field can be created using either electromagnets or permanent magnets. The magnitude of  $H_a$  must be higher than the summation of the saturation magnetization ( $M_S$ ) value of the ferrite material and the DC bias field ( $H_0$ ) to ensure that the ferrite is not in the saturation mode. If the value of the applied external field is less than that, the ferrite will remain in the saturation mode, and it will not be functional. The internal and external fields of a ferrite slab are shown in Fig. 3.1. Nevertheless, the direction of the externally applied field is also an important parameter. It determines which direction of the propagating signal will interact with the ferrite material. For example, recalling the ferrite-based isolator again, the direction of the applied field determines which way the isolator will allow the signal to pass and which way it will pan it.

This chapter presents the investigation and analysis of ferrite material. It can be divided into four parts. The first part is showing the traditional design methodology of the

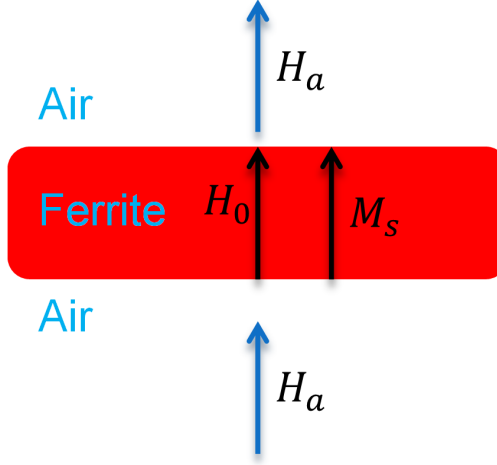


Figure 3.1: Ferrite slab internal and external fields.

ferrite phase shifters that utilize the standard waveguides as an implementation technology. Moreover, its limitations are discussed. Thus, the experience is gained after such investigation and studies. Later, a new model for new ferrite phase shifter structure is proposed and proved with mathematical formulations and equations. Thus, new design procedures are proposed in which the phase shift value flatness is improved. At the end of this part, an example is selected for fabrication to validate the proposed model. Measurements are compared with the simulations and the proposed model results.

The second part is utilizing the same procedures but using another implementation technology that is suitable more for the 5G applications. Such technology is the Ridge Gap Waveguide technology (RGW), this also validates the proposed methodology but in RGW environment. The results are validated by two different numerical solvers, one is the time domain, and the other is the FEM.

Moreover, a phase shifter using the Substrate Integrated Waveguide (SIW) technology is proposed in part three as another example using 5G implementation technologies. This design is for the low profile applications since SIW is a printed technology.

The last part is an example of the differential phase shifters applications. Therefore, an array of two slot antennas deploying RGW technology is designed and introduced. The antenna array is a circularly polarized, and it deploys the RGW shifter proposed in the second part. The circular polarization is achieved through two steps; the first one is the differential phase between the two channels that is  $90^\circ$ , while the second step is the physical rotation between the two slots with  $90^\circ$ .

### **3.1 Rectangular Waveguide Differential Phase Shifter Based on Horizontal Ferrite Tiles: Accurate Model for Full-band Operation**

The phase shifter as known it is a device that adds a specific phase shift to the propagating signal regardless of the direction of propagation, and it also needs a reference phase that is the second channel. While, the differential phase shifter is a device that adds a specific phase on a certain direction of propagation only, and it does not add any phase on the opposite direction of propagation. Each channel has a specific phase added to the propagating signal at a certain direction (same direction for both channels). The phase shift is the difference between the phase of the two channels. Thus, it is called differential phase shifter. This section (Sec. 3.1) is discussed in details and accepted for publication at [76].

This work presents an analysis and study of the waveguide differential phase shifter composed of two horizontal ferrite slabs in each channel. An accurate model for calculating the phase constant is proposed. The transcendental equations that represent the propagation constant of the waveguide that is loaded with two horizontal ferrite slabs are derived starting from Maxwell's equations and validated later by simulations and measurements. The proposed model has shown a maximum percentage error below 10%. An example of the differential phase shifter in Ku-band has been fabricated, where the measured results are in excellent agreement with the proposed model.

#### **3.1.1 Ferrite Differential Phase Shifter Configuration Description**

The ferrite based differential phase shifter has different configurations based on the position and the cross-section shape of the ferrite material such as rectangle, circle, square, or any other geometry. The commonly used ferrites have a rectangular cross-section due to the fabrication feasibility. The ferrite tiles with rectangular cross-section can be placed either in a vertical or in a horizontal orientation. This results in two common configurations: the vertical tile and the horizontal tile phase shifter. The configuration of the differential phase shifter consists of two channels parallel and adjacent to each other. One (or two) ferrite tile(s) with suitable magnetization is placed in each channel. The ferrite tiles in each waveguide are oppositely magnetized to produce the required differential phase shift between the two channels. To achieve the desired differential phase with the least filling factor (i.e., minimize the ratio of the ferrite cross-section to the channel cross-section), the ferrite tiles must be placed at the point of circular polarization inside the rectangular waveguide. In this way,

there is no need to use a larger filling factor because it will be useless. The following equations determine the optimum position of the ferrite slab [8]:

$$\tan(k_c x) = \pm k_c / \beta_0 \quad (3.1)$$

where  $k_c = \pi/a$ ,  $x$  is the location of the circular polarization point in the air filled guide, and  $\beta_0$  is the propagation constant of the air filled guide, which is given by:

$$\beta_0 = \sqrt{k_0^2 - k_c^2} \quad (3.2)$$

In this work, ferrite tiles of a rectangular cross-section are considered. This results in two distinct configurations for the differential phase shifters. The first case is the traditional one, in which a full height vertical ferrite tile is utilized. This case has a relatively high phase shift with high phase variations. The second case has less phase variations and it is recommended for wideband applications, in which two horizontal thin ferrite tiles are mounted on the top and bottom walls of the waveguide [8]. This case has a more flat response, and a wide operating band, however, it has a slightly lower phase shift compared with the vertical case. Fig. 3.2 shows the structure of a single channel according to the first and the second configurations. The max phase shift occurs when the ferrite is placed at a certain point at which two orthogonal magnetic field components are exactly equal to each other. This maximum phase shift point is frequency dependent. As a result, the narrow vertical tile can satisfy this condition for a narrower frequency band. On the other hand, the horizontal tile is able to cover wider range of frequencies with similar performance. This can explain the flat phase shift response of the horizontal tile compared with the vertical one. Moreover, the vertical tile configuration shown in Fig. 3.2(a) has two drawbacks [8]:

- Ferrite alignment difficulty: As the circular polarization point is a function of frequency, the wide frequency variation because the optimum point to be outside the slab width. Therefore, the ferrite will not be fully enabled.
- The vertical orientation of the ferrite slab leads to a small contact area between the ferrite and the metal, which reduces the heat transfer and increases the temperature significantly under high power conditions.

A comparison between the vertical and the horizontal ferrite slabs Differential Phase Shifter (DPS) is presented in Table 3.1.

It is worth to mention that selecting the right ferrite material and applying the suitable magnetic bias is a critical step in building phase shifters. The ferrite selection criteria are illustrated in detail in Appendix A. It is essential to understand this process deeply before

Table 3.1: Comparison Between Differential Phase Shifters Techniques.

Comparison Point	Vertical ferrite DPS [77]	Horizontal ferrite DPS (This work)
Implementation Technology	Rectangular waveguide	Rectangular waveguide
Operating B.W	34 GHz - 40 GHz	Full-band for any standard waveguide
Bandwidth Percentage	16.2%	40%
Maximum Phase Variation Over B.W	20°	15°

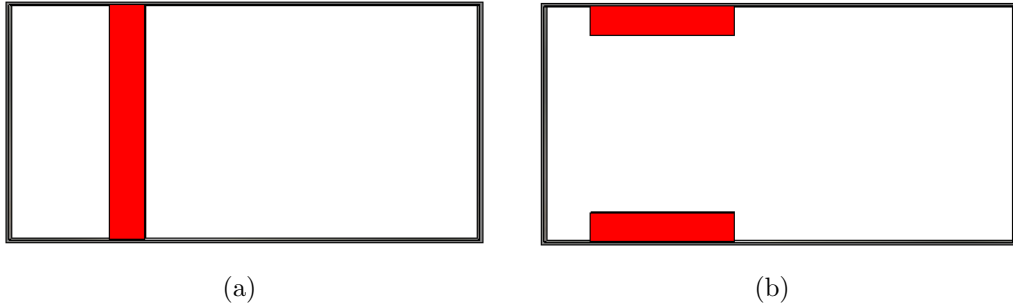


Figure 3.2: Each channel of the ferrite differential phase shifter is deploying. (a) One vertical tile. (b) Two horizontal tiles.

going through either the traditional design methodologies or the proposed work as the same guidelines must be considered in all cases.

### 3.1.2 Traditional Design Methodology Limitations

In this section, the traditional solution of the differential phase shifter problem is discussed, where the current limitations are highlighted. The basic configuration for the differential phase shifter is considered, in which the ferrite slab has a vertical orientation as shown in Fig. 3.2(a). The vertical ferrite slab is centered at the point of circular polarization inside the rectangular waveguide. To find the differential phase occurs due to the existence of the ferrite

slab the phase propagation constant  $\beta$  has to be evaluated. The solution, in this case, is simple and straightforward. However, the vertical tile phase shifter has many limitations compared with the horizontal orientation in terms of both the electrical and thermal characteristics as mentioned before.

The transcendental equation is obtained in the literature in the case of the vertical tile [8, 78]. Afterward, these provided formulas have been simplified to introduce an approximate expression for the phase shift [8].

$$\Delta\beta = 2k_c \frac{\kappa}{\mu} \frac{\Delta S}{S} \sin(2k_c m) \quad (3.3)$$

where  $\kappa$  and  $\mu$  are the elements of the permeability tensor of the ferrite material. Moreover,  $\frac{\Delta S}{S}$  represents the filling factor that is equivalent to the cross-section area of the ferrite divided by the cross-section area of the waveguide. Although this expression has been extracted for the vertical tile case, it is utilized in other ferrite shapes if the filling factor is below 1% (i.e.  $\frac{\Delta S}{S} < 0.01$ ).

In conclusion, although the case of two horizontal slabs is significant due to its advantages compared with the vertical case as explained before, it has not been well investigated in the literature. The approximate expression has an acceptable percentage error for small filling factor ( $\frac{\Delta S}{S}$ ), but these small filling factors are not practical since the differential phase shifter, in this case, needs long length to accomplish the desired phase shift value. To reduce the length of the ferrite slab, the high filling factor is needed. Accordingly, we are proposing an accurate model to solve the differential phase of the horizontal slabs case that is valid for large values of the filling factor, with a maximum error below 10% in the following section.

### 3.1.3 Proposed Model

As a first step, we propose to model the horizontal tile differential phase shifter with an equivalent waveguide, where the horizontal tiles and the intermediate air filling will be replaced by a single effective homogeneous medium. The equivalent slab has the same cross-section area, but it has an effective permeability and an effective dielectric constant. These two parameters depend on the filling factor of the ferrite material. This equivalent model is expected to achieve accurate results only if the ferrite filling is distributed along the region. This case will be entitled as the homogeneous case, which is not practical as the possible configuration is to attach the ferrite material to the top and the bottom walls. A second step is performed to reach an accurate model that can be applied to the realistic case, where the ferrite slabs exist at the top and the bottom wall. In this step, the physical width of the ferrite slab is replaced by an effective one to take into consideration the

discontinuity effect. In the following part, these two steps are discussed in detail starting from the first principles to obtain the required model.

### 3.1.3.1 Homogeneous Case Transcendental Equation

The original structure of the phase shifter is shown in Fig. 3.3(a), while the proposed equivalent model is shown in Fig. 3.3(b). The structure of the equivalent model consists of three regions, where region 1 and region 3 are air-filled, while region 2 represents the effective material of the ferrite tiles. The idea used for region 2 which is shown in equations 3.4, 3.5, and 3.6 is to define the effective parameters by calculating the filling ratio between the ferrite and the air. Thus, it can be considered as averaging the values of  $\mu$ ,  $\kappa$ , and  $\epsilon$ . Later, the correction factor is added to these equations to decrease the error. The elements of permeability tensor and the permittivity of region 1 and 3 are  $\mu_{(1),(3)} = \mu_0$ ,  $\kappa_{(1),(3)} = 0$ ,  $\epsilon_{(1),(3)} = \epsilon_0$ , respectively. On the other hand, both the permeability and the permittivity in region 2 are assumed to be:

$$\mu_{eff(2)} = \frac{h_f}{b} (\mu_0 \left[ 1 + \frac{f_0 f_m}{f_0^2 - f^2} \right]) + (1 - \frac{h_f}{b}) \mu_0 \quad (3.4)$$

$$\kappa_{eff(2)} = \frac{h_f}{b} \mu_0 \left[ \frac{f f_m}{f_0^2 - f^2} \right] \quad (3.5)$$

$$\epsilon_{eff(2)} = \frac{h_f}{b} \epsilon_r \epsilon_0 + (1 - \frac{h_f}{b}) \epsilon_0 \quad (3.6)$$

Where  $f_m$  and  $f_0$  are the saturated magnetic and the Larmor frequencies, respectively. Hence, the permeability tensor  $[\mu_{eff(2)}]$  for the  $\hat{y}$  bias will be:

$$[\mu_{eff(2)}] = \begin{bmatrix} \mu_{eff(2)} & 0 & -j\kappa_{eff(2)} \\ 0 & \mu_0 & 0 \\ j\kappa_{eff(2)} & 0 & \mu_{eff(2)} \end{bmatrix} \quad (3.7)$$

The phase propagation constant  $\beta$  of the equivalent model will be obtained from Maxwell equations that can be written in the case of source free as:

$$\nabla \times \vec{E} = -j\omega \vec{B} \quad (3.8)$$

$$\nabla \times \vec{H} = j\omega \vec{D} \quad (3.9)$$

For linear isotropic mediums:

$$\nabla \times \vec{E} = -j\omega \mu \vec{H} \quad (3.10)$$

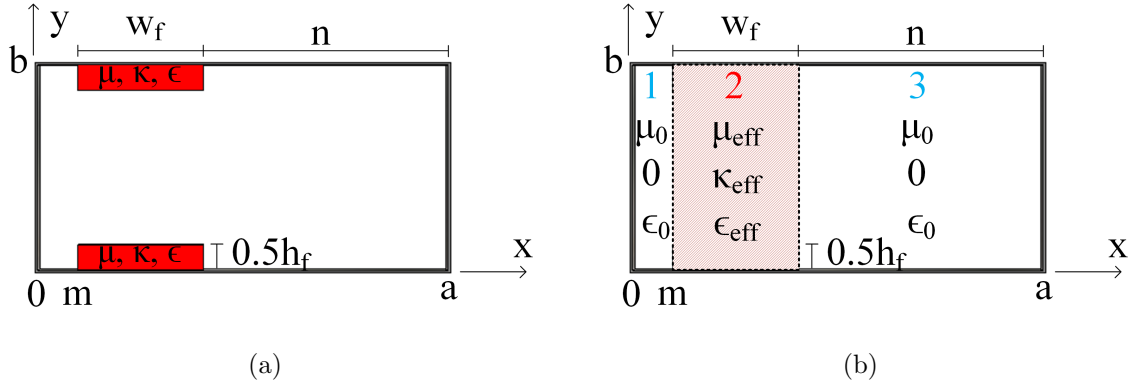


Figure 3.3: Each channel of the ferrite differential phase shifter. (a) Actual structure. (b) Effective model.

$$\nabla \times \vec{H} = j\omega\epsilon\vec{E} \quad (3.11)$$

As the ferrite materials are anisotropic materials, the magnetic flux density and the magnetic field can be related to each other by the following relation in region 2:

$$\vec{B} = [\mu_{eff}] \vec{H} \quad (3.12)$$

Assuming  $\vec{E}$  and  $\vec{H}$  are:

$$\vec{E}(x, y, z) = [\vec{e}(x, y) + \hat{z}e_z(x, y)]e^{-j\beta z} \quad (3.13)$$

$$\vec{H}(x, y, z) = [\vec{h}(x, y) + \hat{z}h_z(x, y)]e^{-j\beta z} \quad (3.14)$$

Enforcing the boundary conditions in the three regions a resultant transcendental equation for the propagation constant  $\beta$  can be derived.

By solving Maxwell's equations based on  $\vec{E}$  and  $\vec{H}$  in (3.13) and (3.14), and if the propagating mode is TE<sub>10</sub>, the equations are reduced to:

$$j\beta e_y = -j\omega(\mu_{eff(2)}h_x - j\kappa_{eff(2)}h_z) \quad (3.15)$$

$$\frac{\partial e_y}{\partial x} = -j\omega(j\kappa_{eff(2)}h_x + \mu_{eff(2)}h_z) \quad (3.16)$$

$$j\omega\epsilon_{eff(2)}e_y = -j\beta h_x - \frac{\partial h_z}{\partial x} \quad (3.17)$$

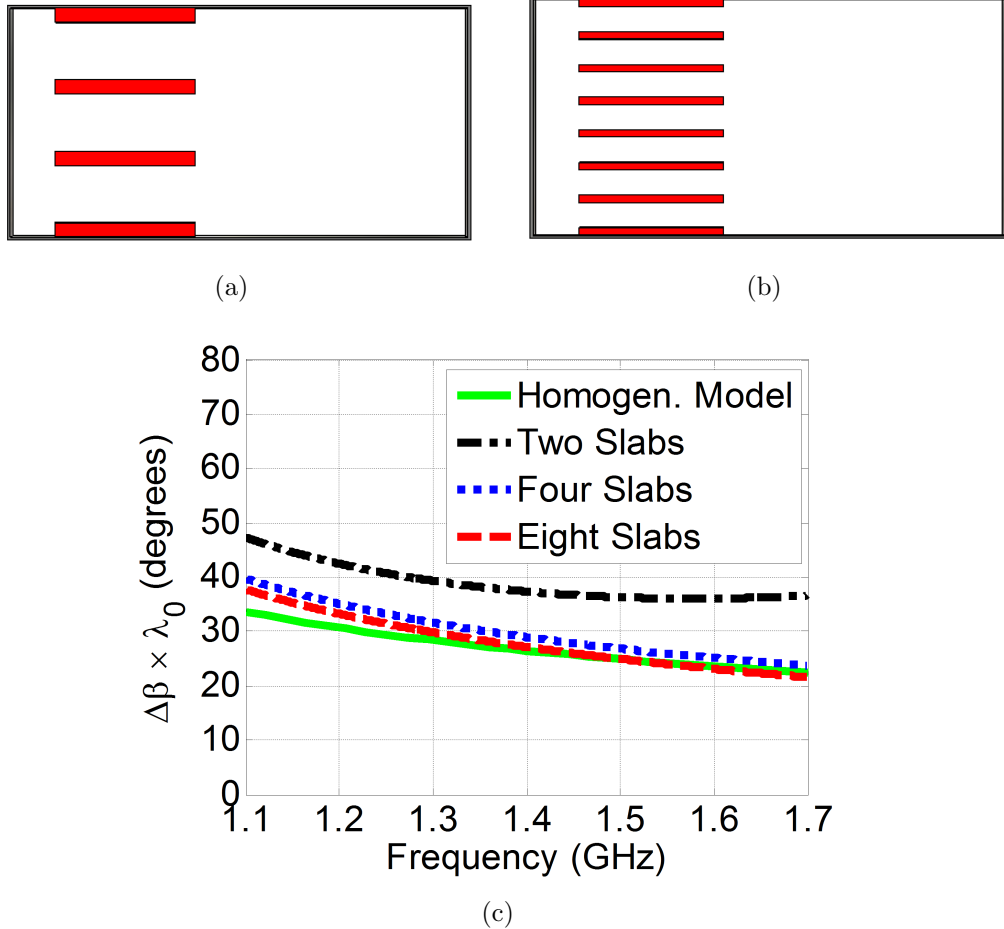


Figure 3.4: Ferrite material distribution. (a) Four tiles. (b) Eight tiles.(c) Simulation results comparison (WR-650,  $4\pi M_s = 300$  G,  $H_0 = 120$  Oe,  $\frac{\Delta S}{S} = 0.075$ ).

Solving (3.15) and (3.16) to find  $h_x$  and  $h_z$

$$h_x = -\frac{\beta e_y}{\omega \mu_f} - \frac{\kappa_{eff(2)}}{\omega \mu_f \mu_{eff(2)}} \frac{\partial e_y}{\partial x} \quad (3.18)$$

$$h_z = \frac{j \kappa_{eff(2)} \beta e_y}{\omega \mu_f \mu_{eff(2)}} + \frac{j}{\omega \mu_f} \frac{\partial e_y}{\partial x} \quad (3.19)$$

Where here the factor  $\mu_f$  is defined by

$$\mu_f = \frac{\mu_{eff(2)}^2 - \kappa_{eff(2)}^2}{\mu_{eff(2)}} \quad (3.20)$$

Substitute by (3.18), (3.19), and (3.20) in (3.17) to find the wave equation  $e_y$ :

$$\begin{aligned} j\omega\epsilon_{eff(2)}e_y &= \left(\frac{j\beta}{\omega\mu_{eff(2)}\mu_f}\right)(\mu_{eff(2)}\beta e_y + \kappa_{eff(2)}\frac{\partial e_y}{\partial x}) \\ &\quad - \left(\frac{j}{\omega\mu_{eff(2)}\mu_f}\right)(\kappa_{eff(2)}\beta\frac{\partial e_y}{\partial x} + \mu_{eff(2)}\frac{\partial^2 e_y}{\partial x^2}) \end{aligned} \quad (3.21)$$

Obtaining the corresponding results for region 1 and 3:

$$\left(\frac{\partial^2}{\partial x^2} + k_f^2\right)e_y = 0 \quad (3.22)$$

Where  $k_f$  is the cutoff wave number for the ferrite and it is related to  $\beta$  by:

$$k_f^2 = \omega^2\mu_f^2\epsilon_{eff(2)} - \beta^2 \quad (3.23)$$

$k_a$  is the cutoff wave number of the air regions and it is related to  $\beta$  by:

$$k_a^2 = k_0^2 - \beta^2 \quad (3.24)$$

$h_x$  and  $h_z$  in the air region are given by:

$$h_x = -\frac{\beta}{\omega\mu_0}e_y \quad (3.25)$$

$$h_z = \frac{j}{\omega\mu_0}\frac{\partial e_y}{\partial x} \quad (3.26)$$

The solution of  $e_y$  inside the waveguide that can satisfy the boundary conditions for the three regions:

$$e_y = \begin{cases} C_1 \sin k_a x, & \text{for } 0 < x < m \\ C_2 \sin k_f(x - m) \\ + C_3 \sin k_f(m + w_f - x), & \text{for } m < n < m + w_f \\ C_4 \sin k_a(a - x), & \text{for } m + w_f < n < a \end{cases} \quad (3.27)$$

Using (3.26) and (3.27) to get  $h_z$  and then matching  $e_y$  with  $h_z$  at  $x = m$ ,  $x = m + w_f = a - n$  results in four equations for the constants  $C_1$ ,  $C_2$ ,  $C_3$ , and  $C_4$ :

$$C_1 \sin(k_a m) = C_3 \sin(k_f w_f) \quad (3.28)$$

$$C_2 \sin(k_f w_f) = C_4 \sin(k_a n) \quad (3.29)$$

$$\begin{aligned} \frac{C_1 k_a}{\mu_0} \cos k_a m &= \frac{C_2 k_f}{\mu_f} \\ &+ \frac{C_3}{\mu_{eff(2)} \mu_f} (\kappa_{eff(2)} \beta \sin k_f w_f - \mu_{eff(2)} k_f \cos k_f w_f) \end{aligned} \quad (3.30)$$

$$\begin{aligned} \frac{C_4 k_a}{\mu_0} \cos k_a n &= \frac{C_3 k_f}{\mu_f} \\ &- \frac{C_2}{\mu_{eff(2)} \mu_f} (\kappa_{eff(2)} \beta \sin k_f w_f + \mu_{eff(2)} k_f \cos k_f w_f) \end{aligned} \quad (3.31)$$

By solving (3.28) and (3.29) and substituting in (3.30) and (3.31), then eliminating all the constants results in a transcendental equation for the propagation constant  $\beta$  as:

$$\begin{aligned} &\left(\frac{k_f}{\mu_f}\right)^2 + \left(\frac{\kappa_{eff(2)} \beta}{\mu_{eff(2)} \mu_f}\right)^2 \\ &- \frac{k_a}{\tan k_a m} \left( \frac{k_f}{\mu_0 \mu_f \tan k_f w_f} + \frac{\kappa_{eff(2)} \beta}{\mu_0 \mu_{eff(2)} \mu_f} \right) \\ &- \left(\frac{k_a}{\mu_0}\right)^2 \frac{1}{\tan k_a m \tan k_a n} \\ &- \frac{k_a}{\tan k_a n} \left( \frac{k_f}{\mu_0 \mu_f \tan k_f w_f} - \frac{\kappa_{eff(2)} \beta}{\mu_0 \mu_{eff(2)} \mu_f} \right) = 0 \end{aligned} \quad (3.32)$$

In this case, the total area of the ferrite material ( $\Delta S = w_f \times b$ ) is uniformly distributed over the waveguide cross-section area ( $S = a \times b$ ) in such way the medium in this area is a homogeneous medium. As the number of the ferrite slabs number increases and their thickness decrease but with the same filling factor, the medium becomes more homogenized. The ideal case is represented by the proposed model so far to have an infinite number of horizontal slabs with almost zero thickness. To prove this claim, different configurations are investigated and shown in Figs 3.4(a), 3.4(b). In these configurations, the ferrite material is distributed over four and eight strips, respectively. The phase shift is extracted numerically and compared with the realistic case (Two slabs) and the homogeneous model in Fig. 3.4(c). This figure shows that if the ferrite is distributed more, the phase shift response is getting closer to the proposed homogeneous model.

### 3.1.3.2 In-homogeneous Case Adjustment

In this case, the two distinct ferrite horizontal slabs are considered, the ferrite slab total area is not uniformly distributed over the cross-section area  $w_f \times b$ , that means the ferrite medium here is inhomogeneous medium. Due to the sudden discontinuities between the ferrite and the air. Some adjustment must be performed for the proposed model. Fringed fields above the ferrite slab lead to an effective height slightly larger than the physical height. This can

be represented mathematically with a correction factor  $CF$ . Hence,  $h_f$  in Equations (3.4), (3.5), and (3.6) will be replaced with  $h'_f$  as

$$h'_f = CF \times h_f \quad (3.33)$$

where  $CF$  is a correction factor that represents the in-homogeneity of the ferrite distribution. The empirical expression that represents this correction factor is extracted through comparison with the extracted results numerically over several standard rectangular waveguides. Many parametric sweeps are performed such as the ferrite slab dimensions and parameters. Then, the final  $CF$  is obtained numerically. Furthermore, if the ferrite filling factor is less than 7.5% ( $\frac{\Delta S}{S} \leq 0.075$ ) with an aspect ratio between 5 and 9, the  $CF$  is valid for any waveguide dimension and operating frequency. The correction factor is represented by the following equation:

$$CF = F_1 \times F_2 \quad (3.34)$$

Where  $F_1$  and  $F_2$  can be defined by the following equations that have the constants shown in Table 3.2.

$$F_1 = a_1 \times \arctan(a_2 \times 100 \times \frac{\Delta S}{S} - a_3) + a_4 \quad (3.35)$$

$$F_2 = b_1 \times \sin(b_2 \times Fr_{asr}) + b_3 \quad (3.36)$$

Where  $Fr_{asr}$  is the aspect ratio of each ferrite tile cross-section area that is given by the following equation using the parameters shown in Fig. 3.3.

$$Fr_{asr} = W_f/h_f \quad (3.37)$$

Based on equation (3.33), the correction factor represents the essential modification in the ferrite slab height for the model to obtain accurate values for the phase shift. As the model is based on a physical insight and the correction factor compensates only for the inhomogeneous distribution of the ferrite material, it is expected to have a constant value for the correction factor with respect to frequency (it is not a frequency dependent value). As the equations (3.34) through (3.37) show, this factor depends only on the physical dimensions of the ferrite slab and the dimensions of the rectangular waveguide cross-section. Hence, the proposed model along with this correction factor can obtain the phase shift in all rectangular waveguide standards loaded with horizontal ferrite slabs with slight deviation as will be discussed in subsection 3.1.4.

Some examples are selected to show the effect of the  $CF$  on Equations (3.4), (3.5), and

Table 3.2: Correction Factor Equation Constants.

Parameter	Value	Parameter	Value
$a_1$	0.16	$b_1$	1.18
$a_2$	0.90	$b_2$	0.21
$a_3$	7.10	$b_3$	0.11
$a_4$	1.08		

(3.6). The CF is a function of  $\frac{\Delta S}{S}$  and  $Fr_{asr}$  as shown before. Thus, the three standard waveguides WR-650, WR-90, and WR-28 are selected, each of them has a  $\frac{\Delta S}{S} = 0.075$ , and  $Fr_{asr} = 7$ . Nevertheless, other filling factors and aspect ratios are valid; only those examples are selected to facilitate the article readability. The effective model parameters with and without the correction factor for the selected examples are shown in Fig 3.5, Fig. 3.6, and Fig. 3.7.

Figure 3.8 shows the variation of the phase constant versus frequency for the right hand circularly polarized, the left hand circularly polarized components and the difference.

### 3.1.4 Validation and Experimental Results

Many cases using different standard waveguides have been studied and investigated to validate the proposed inhomogeneous model equations. Some cases have been selected and presented in this section. The selected waveguides are WR-650, WR-90, and WR-28 that covers the L-band, X-band, and Ka-band, respectively. Each case is evaluated using the proposed inhomogeneous model equations and then compared with both approximate relation and the numerical simulation results. Suitable parameters are selected for each case. The differential phase ( $\Delta\beta$ ) for each case is calculated for a guided wavelength at the center frequency ( $\lambda_0$ ) of each corresponding band.

The comparison of the three methods for the standard waveguide WR-650 is shown in Fig. 3.9, the behavior of the three curves is almost the same with slight deviations for the small filling factor ( $\frac{\Delta S}{S} = 0.01$ ), meanwhile, for larger filling factor ( $\frac{\Delta S}{S} = 0.075$ ) the proposed model is very close to the numerical simulation results with the deviation that does not exceed 10%. The same behavior for the other standard waveguides WR-90 and WR-28, their comparisons are shown in Figs 3.10, and 3.11, respectively. It is clear from the shown comparison curves that the approximate relation has an acceptable percentage error for small ferrite filling factors but not for the high filling factors. On the other side, the proposed model finds a value of the differential phase that is much closer to the true one.

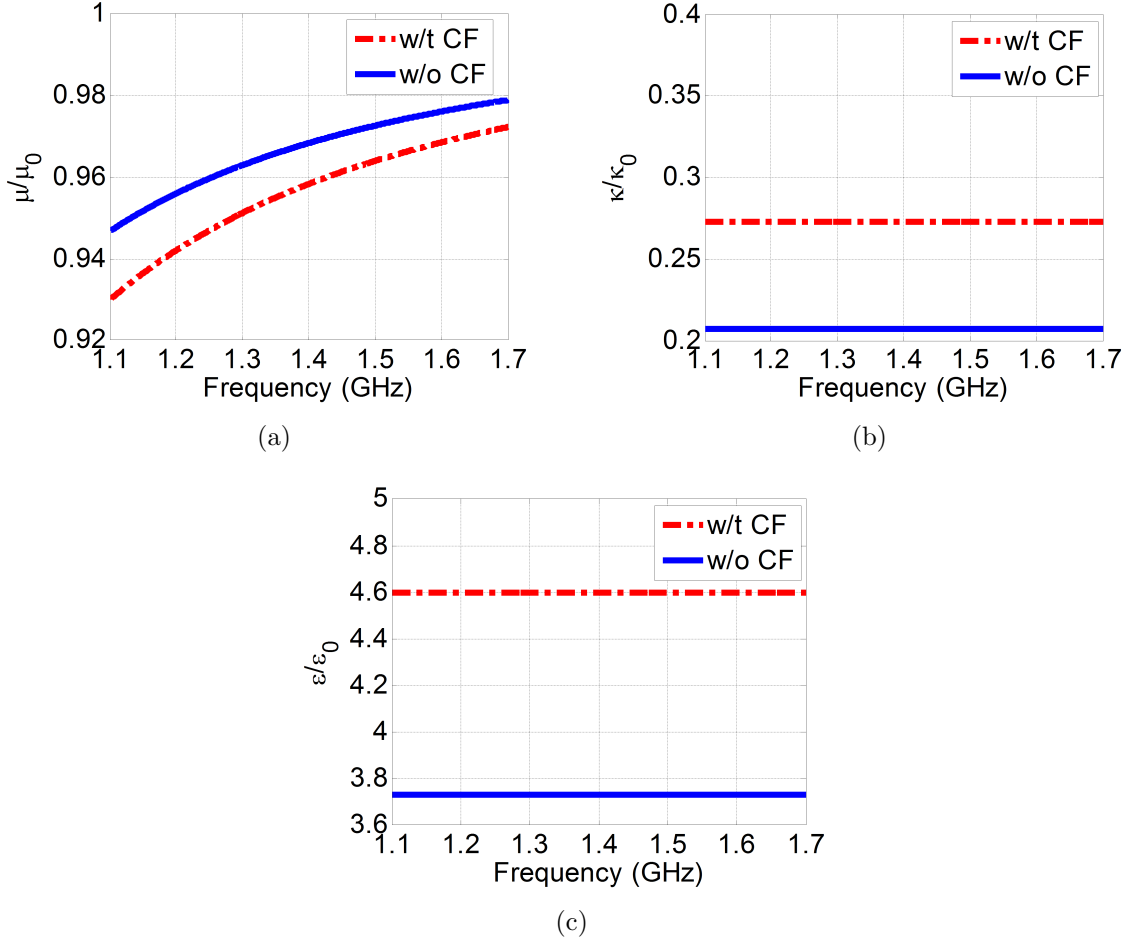


Figure 3.5: The effective model parameters in the case of WR-650 ( $4\pi M_s = 300$  G,  $H_0 = 120$  Oe,  $\frac{\Delta S}{S} = 0.075$ ,  $Fr_{asr} = 7$ ). (a)  $\frac{\mu}{\mu_0}$ . (b)  $\frac{\kappa}{\kappa_0}$ . (c)  $\frac{\epsilon}{\epsilon_0}$ .

The error percentage of the proposed model as a function of  $\frac{\Delta S}{S}$  and  $Fr_{asr}$  is plotted in Fig. 3.12.

The approximate relation is based on oversimplifying the phase shift expressions of the vertical slab while using this expression in all cases [8]. As a result, this relation fails to obtain the phase shift with reasonable accuracy in many cases, especially in the case of the horizontal slab. On the other hand, the proposed model defines an effective region with a correction factor for the slab height to model the ferrite loaded rectangular waveguide (as described before). This model can obtain the phase shift with reasonable accuracy as shown in Figs. 3.9, 3.10, and 3.11, where the proposed correction factor is a part of the presented model.

The approximate model is very close as long as the filling factor is extremely small (below 1%). Thus, we proposed our model to cover both small and large values for filling factors, which is needed for practical applications. Our model is valid up to 0.075 filling factor (7.5%),

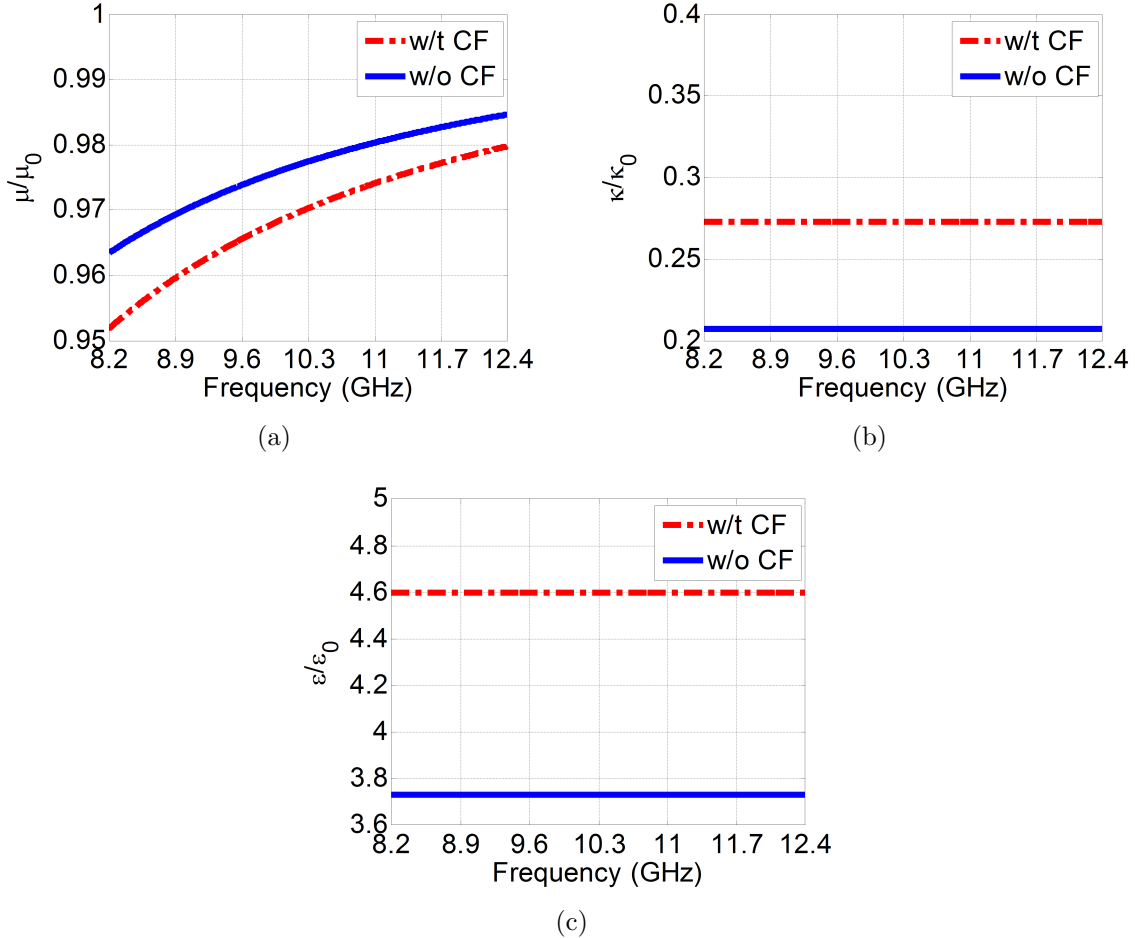


Figure 3.6: The effective model parameters in the case of WR-90 ( $4\pi M_s = 1880$  G,  $H_0 = 752$  Oe,  $\frac{\Delta S}{S} = 0.075$ ,  $Fr_{asr} = 7$ ). (a)  $\frac{\mu}{\mu_0}$ . (b)  $\frac{\kappa}{\kappa_0}$ . (c)  $\frac{\epsilon}{\epsilon_0}$ .

which can cover all the practical applications of these components. Nevertheless, our model is valid for all frequency bands.

The deviation between the proposed model and the numerical solution is limited as the error calculated in all standard waveguide is below 10%, which can be depicted from Fig. 3.12. However, this can be enhanced by calculating an effective ferrite slab width to the ferrite slab to take into consideration the fringing fields as a future extension to this work.

An example is constructed and measured in favor of comparing it with the proposed model as well as the simulations. This example utilizes the standard waveguide WR-28 with two ferrite slabs per channel as described before. The ferrite material is nickel ferrite with zinc substitution with  $4\pi M_s = 5300$  G,  $\epsilon_r = 13.5$ , and  $\tan \delta = 0.0006$ . Each ferrite slab has dimensions of  $25.4 \times 1.9 \times 0.56$  mm<sup>3</sup>. Thus the ferrite filling factor  $\frac{\Delta S}{S}$  is 0.084, and each slab aspect ratio  $Fr_{asr}$  is 3.4. The frequency range of the comparison between measurements and other methods (proposed model, approximate relation, and numerical simulation) is limited

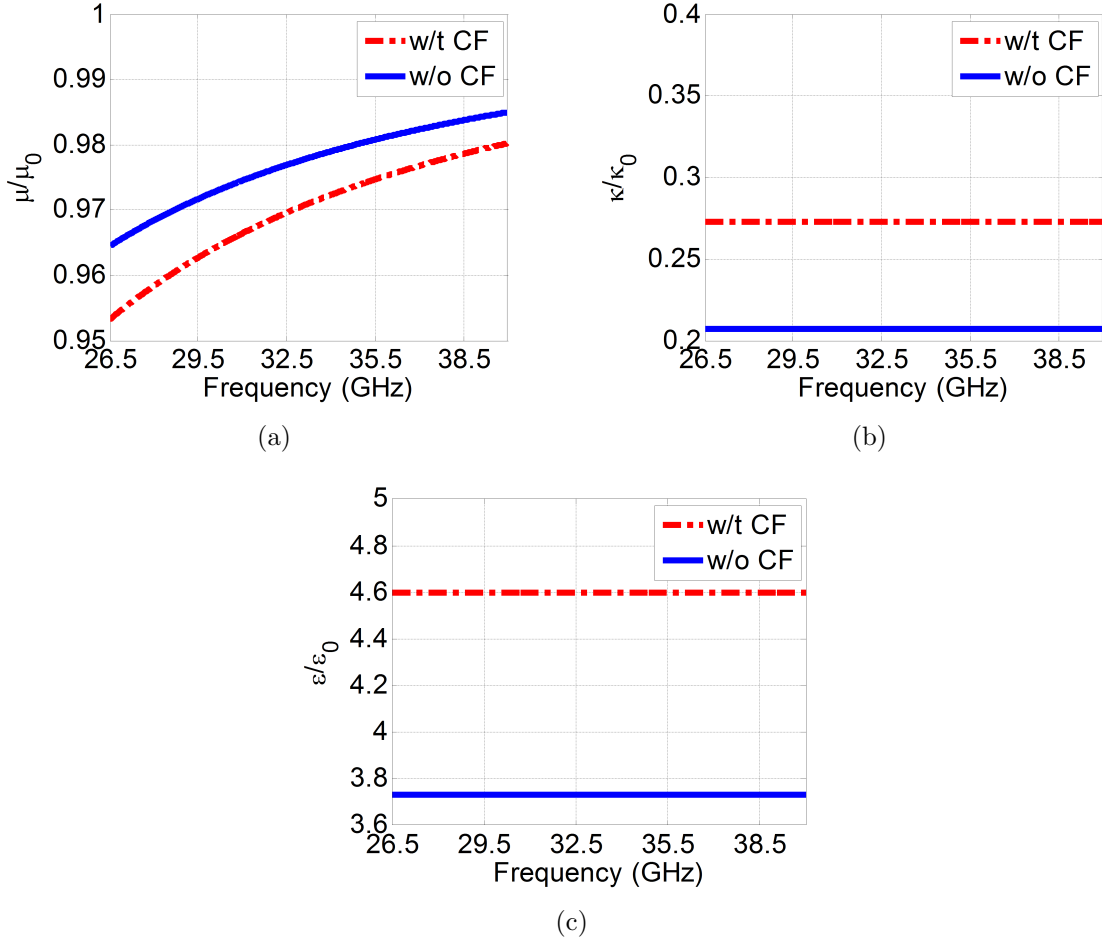


Figure 3.7: The effective model parameters in the case of WR-28 ( $4\pi M_s = 6000$  G,  $H_0 = 2400$  Oe,  $\frac{\Delta S}{S} = 0.075$ ,  $Fr_{asr} = 7$ ). (a)  $\frac{\mu}{\mu_0}$ . (b)  $\frac{\kappa}{\kappa_0}$ . (c)  $\frac{\epsilon}{\epsilon_0}$ .

to 26.5-34 GHz due to limitations of the fabrication with respect to the exact values of dimensions and  $4\pi M_s$ .

The setup of the fabricated example consists of one channel in order to facilitate the setup. This is equivalent to the differential phase shift between two channels that have the same ferrite slabs with the same direction and magnitude of magnetization. The only difference between the two channels is the ferrite slabs location; each channel is a mirrored version of the other. The measurement setup is shown in Fig. 3.13(a). The comparisons of the measured differential phase shift, and the S-parameters magnitudes simulation and measurement comparison are shown in Fig. 3.13.

It is clear from Fig. 3.13(b) that the approximate relation fails at higher frequencies, meanwhile, the proposed model is very close to the simulations. In this figure, we tried three tolerance values ( $\pm 5\%$ ,  $\pm 7.5\%$ , and  $\pm 10\%$ ). The closest curve to the measurements is the one with  $\pm 10\%$  tolerance as shown in Fig. 3.13(b). The other two curves indicate a large

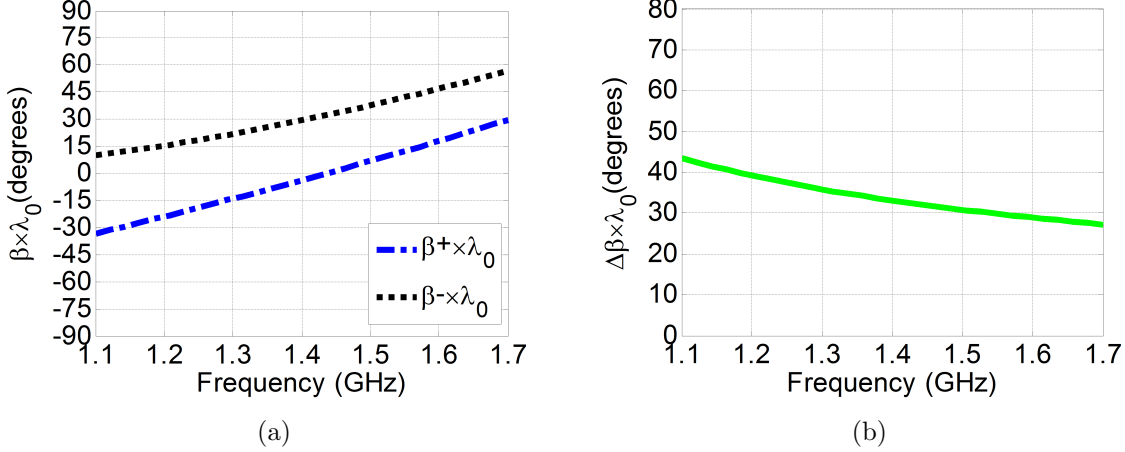


Figure 3.8:  $\beta \times \lambda_0$  components for WR-650 ( $4\pi M_s = 300$  G,  $H_0 = 120$  Oe,  $\frac{\Delta S}{S} = 0.075$ ,  $Fr_{asr} = 7$ ). (a)  $\beta^+ \times \lambda_0$  and  $\beta^- \times \lambda_0$ . (b)  $\Delta \beta \times \lambda_0$ .

deviation. The reason for such a deviation between the measured and simulated phase can be attributed to the tolerance of the ferrite slabs alignment, which was difficult to verify due to the long and narrow closed waveguide. In addition, the value of  $H_0$  of the magnet is tough to achieve practically with a precise value. Nevertheless, the magnitude of the  $4\pi M_s$  of the ferrite material has  $\pm 5\%$  tolerance, and its physical parameters are measured at 9 GHz by the manufacturer. Those physical parameters can change a bit at the 30 GHz band. Thus, some deviations in the measurements are expected. In Fig. 3.13(c) the matching level is acceptable. However, these ripples are attributed to the effect of the ferrite slabs and the magnets. Moreover, the insertion loss levels of the measurements and the simulations are close to each other.

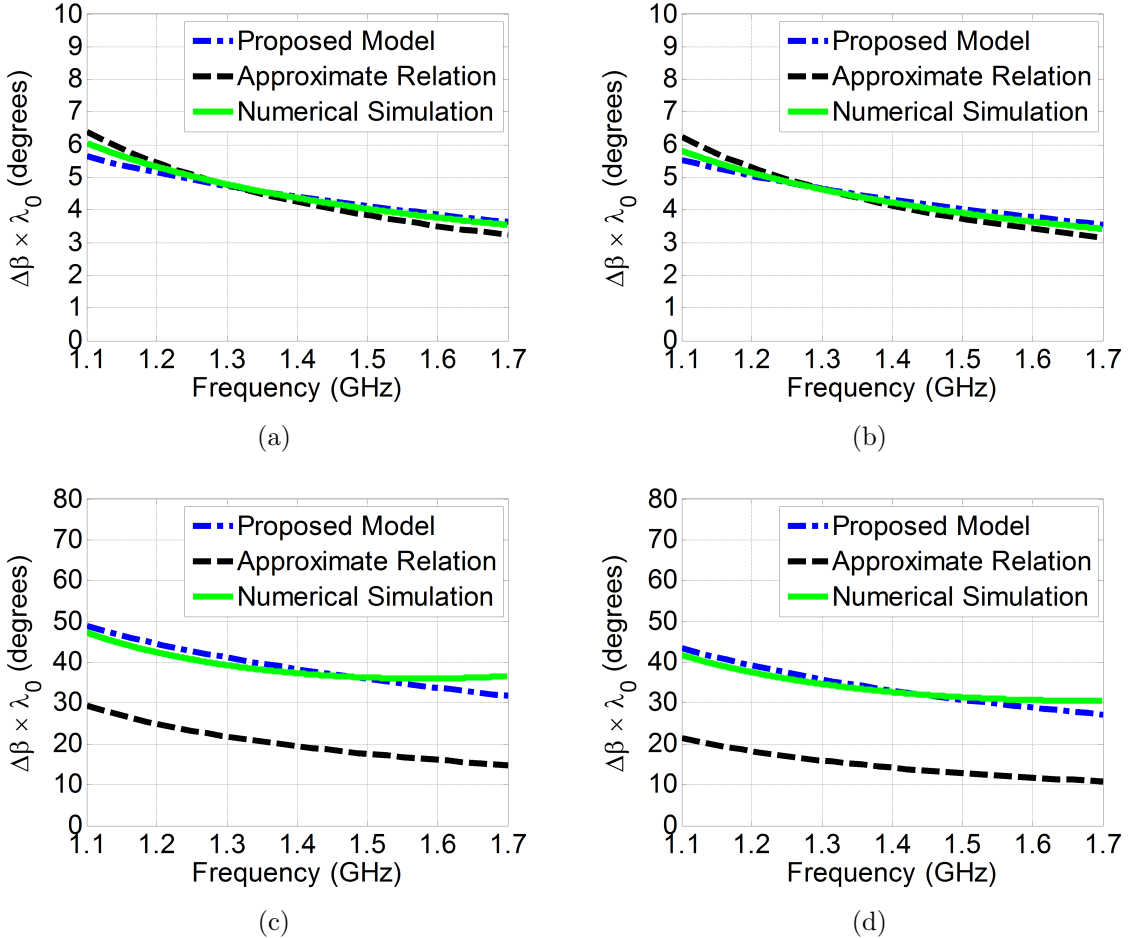
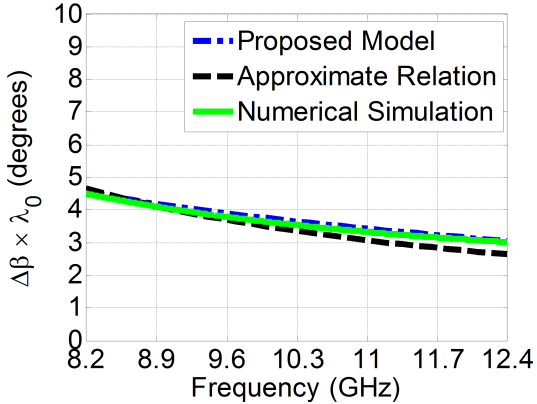
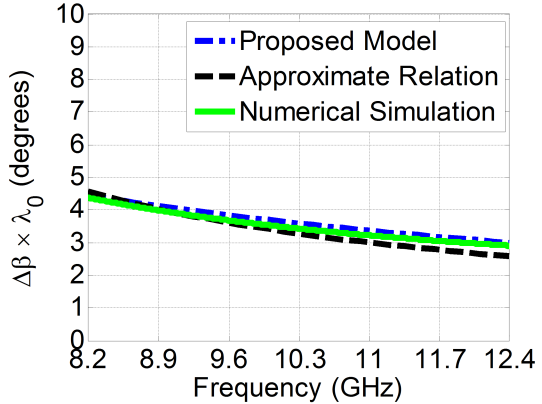


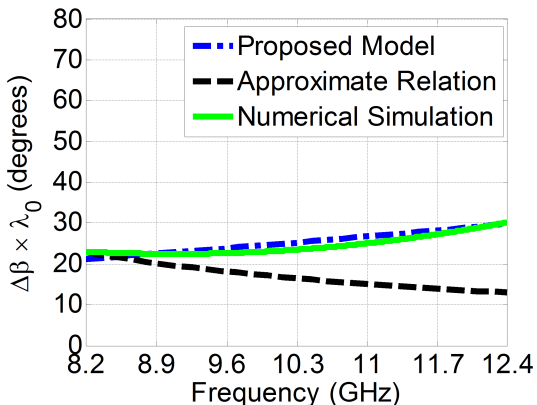
Figure 3.9: Comparing proposed inhomogeneous. model with CST and Approx. model (WR-650,  $4\pi M_s = 300$  G,  $H_0 = 120$  Oe). (a)  $\frac{\Delta S}{S} = 0.01, Fr_{asr} = 5$ . (b)  $\frac{\Delta S}{S} = 0.01, Fr_{asr} = 7$ . (c)  $\frac{\Delta S}{S} = 0.075, Fr_{asr} = 5$ . (d)  $\frac{\Delta S}{S} = 0.075, Fr_{asr} = 7$ .



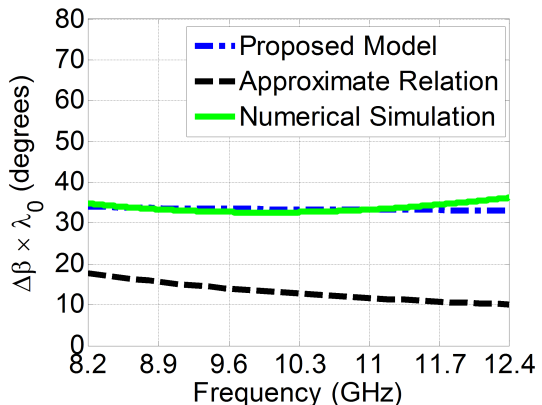
(a)



(b)



(c)



(d)

Figure 3.10: Comparing proposed inhomogeneous. model with CST and Approx. model (WR-90,  $4\pi M_s = 1880$  G,  $H_0 = 752$  Oe). (a)  $\frac{\Delta S}{S} = 0.01$ ,  $Fr_{asr} = 5$ . (b)  $\frac{\Delta S}{S} = 0.01$ ,  $Fr_{asr} = 7$ . (c)  $\frac{\Delta S}{S} = 0.075$ ,  $Fr_{asr} = 5$ . (d)  $\frac{\Delta S}{S} = 0.075$ ,  $Fr_{asr} = 7$ .

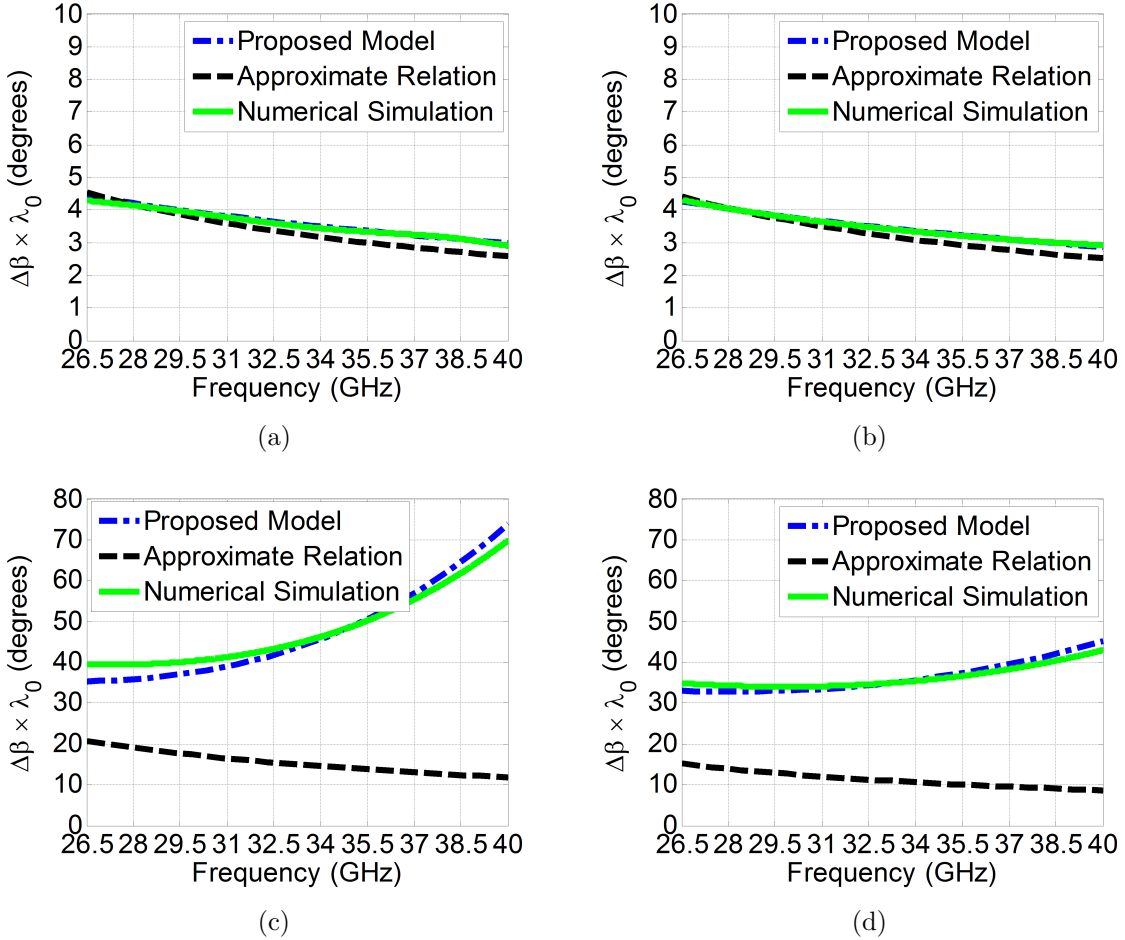


Figure 3.11: Comparing proposed inhomogeneous. model with CST and Approx. model (WR-28,  $4\pi M_s = 6000$  G,  $H_0 = 2400$  Oe). (a)  $\frac{\Delta S}{S} = 0.01$ ,  $Fr_{asr} = 5$ . (b)  $\frac{\Delta S}{S} = 0.01$ ,  $Fr_{asr} = 7$ . (c)  $\frac{\Delta S}{S} = 0.075$ ,  $Fr_{asr} = 5$ . (d)  $\frac{\Delta S}{S} = 0.075$ ,  $Fr_{asr} = 7$ .

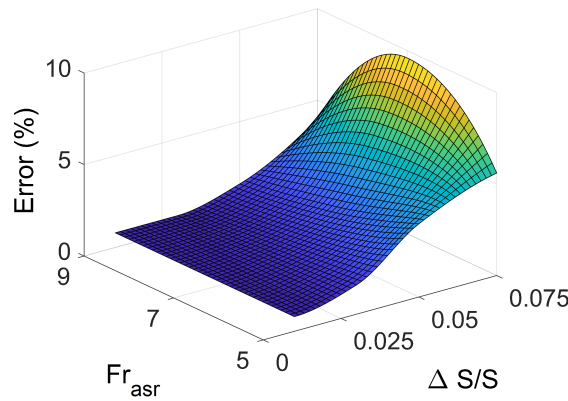
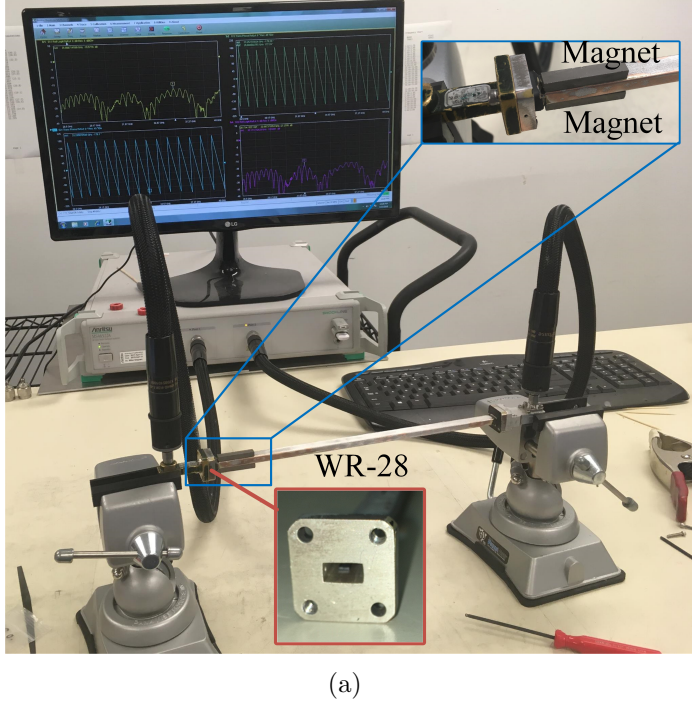
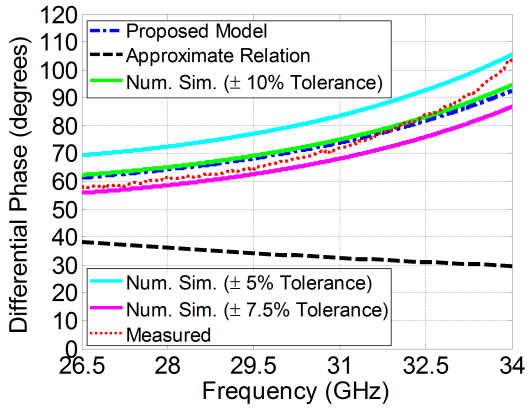


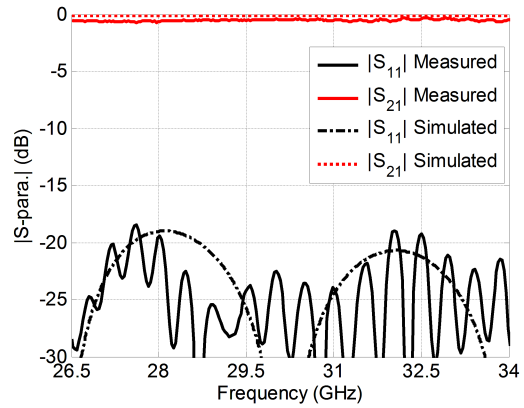
Figure 3.12: Proposed inhomogeneous model percentage error as a function of  $\frac{\Delta S}{S}$  and  $Fr_{asr}$ .



(a)



(b)



(c)

Figure 3.13: Fabricated example. (a) Measurement setup. (b) Measured differential phase shift (dotted red) comparison with simulations (solid line:  $\pm 10\%$  Tolerance: green,  $\pm 7.5\%$  Tolerance: magenta, and  $\pm 5\%$  Tolerance: cyan), approximate model (dashed black) and proposed model (dash-dotted blue). (c) S-parameters magnitudes simulation and measurement comparison.

## 3.2 Compact Ultra-Flat RGW Differential Phase Shifter for Millimeter-Wave Applications

This work introduces a compact Differential Phase Shifter (DPS) based on RGW technology. The proposed structure is new, and it covers a bandwidth of 5 GHz around the center frequency of value 30 GHz. The phase shift of the presented work is  $90^\circ$  with an ultra-flat response over the covered band with phase variation of less than  $10^\circ$ . This section (Sec. 3.2) is explained more and published at [79].

### 3.2.1 Ferrite Slab Operation

In this section, the ferrite slab material selection is discussed briefly as well as its optimum location. In order to activate the ferrite material, certain factors must be considered, which will be described later in this section. Moreover, the location of the ferrite slab is a very critical parameter in which the differential phase of the shifter can be controlled.

Material selection depends mainly on two parameters the saturation magnetization factor ( $4\pi M_s$ ), and magnetic DC bias ( $H_0$ ). The equations representing those parameters are given by [8]:

$$4\pi M_s(G) = f_m(MHz)/2.8 \quad (3.38)$$

$$H_0(Oe) = f_0(MHz)/2.8 \quad (3.39)$$

where  $f_m$  and  $f_0$  are the saturated magnetic and the Larmor frequencies, respectively. The minimum frequency ( $f_{min}$ ) must be at least equivalent to the sum of  $f_0$  and  $f_m$ .

The ferrite slab operation depends mainly on the quasi-TEM mode. Since it is not pure TEM, the ferrite slab makes use of the fringing fields between the ridge and edge of the first column of the unit cells. In other words, if the propagating mode is only TEM the ferrite slab will not operate. The optimum location of the slab is to be centered around the ridge edge. Thus, all the fringing fields will be considered. If the slab is shifted forward more to the unit cells column it will be useless since the fringing fields are minimum there, also shifting it more backward will just attenuate the propagating signal without any benefit to the differential phase.

### 3.2.2 RGW Differential Phase Shifter Design

In this section, the RGW DPS configuration is described starting with the unit cell design, then the whole phase shifter, and finally, simulations are performed using two different numerical solvers in the time domain and in the frequency domain and compared with each other.

#### 3.2.2.1 Unit Cell Design

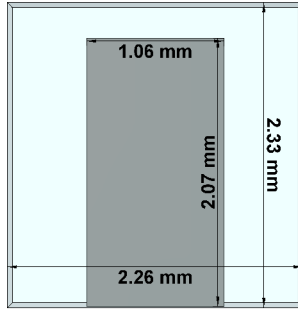


Figure 3.14: Geometry of the nail unit cell.

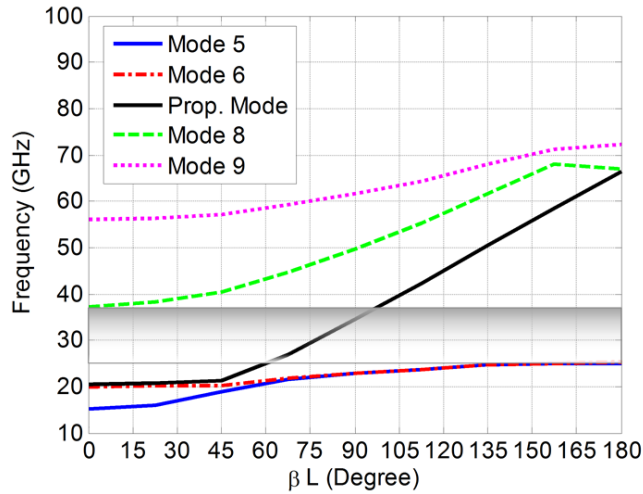


Figure 3.15: RGW propagating modes and its band gap.

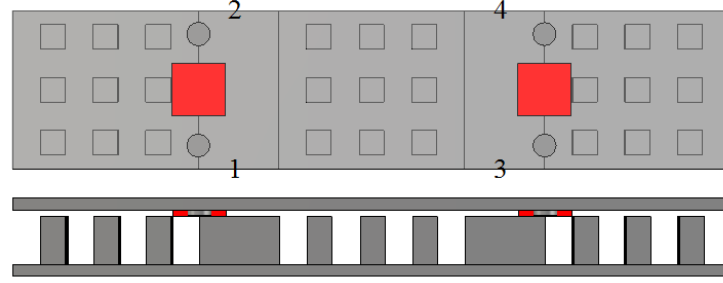


Figure 3.16: RGW differential phase shifter geometry.

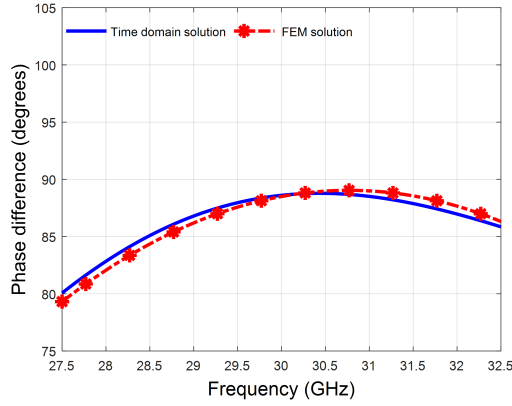


Figure 3.17: Differential phase between the outputs of the proposed RGW DPS channels outputs.

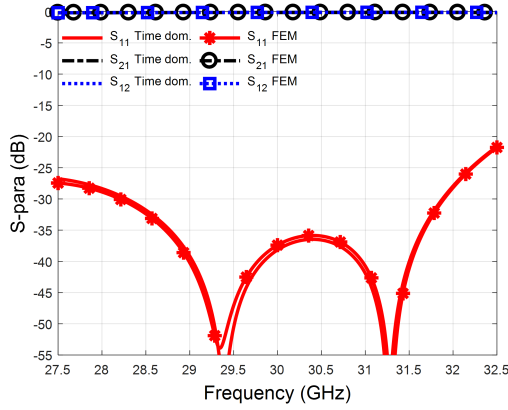


Figure 3.18: Matching and transmission coefficients of the proposed RGW DPS.

The first step to design the RGW phase shifter is to design the RGW. The RGW consists of the ridge surrounded by a bed of nails. The bed of nails is designed as a periodic structure that acts as an EBG surface that suppresses the waves that leak off the ridge that acts as

the propagating medium. The unit cell that covers the targeted frequency band should be designed. The dimensions and geometry of the proposed cell are shown in Fig. 3.14. In order to assure the band gap of the RGW transmission line, it is necessary to simulate one row including the ridge and three unit cells on each side. The geometry and the simulation results of such structure are shown in Fig. 3.15. However, the propagating mode of the ridge is from 20 GHz to 65 GHz, the band gap of this configuration is from 20 to 38 GHz.

### 3.2.2.2 RGW DPS Configuration

This section presents the proposed non-reciprocal ferrite differential phase shifter for 30 GHz band applications. The proposed structure shown in Fig. 3.16 is based on RGW technology. The DPS consists of two channels; each has a ferrite slab with suitable magnetization. Such slab is inserted between the top plate of the RGW and the top of the ridge. Hence, the slab fits in the gap. The slab has the same length as the unit cell which is 2.26 mm. Moreover, the slab width is also the same as its length. The material used has an epsilon of 14.2. Two pins are used to improve the matching level each has a radius of 0.508 mm and height of 0.254 mm. Such pins are inserted from the upper plate of the ridge; each has a center that is placed at 2.286 mm from the slab center.

The differential phase shift and S-parameters are extracted using two different numerical solvers. The differential phase is shown in Fig. 3.17, meanwhile, both of matching and transmission coefficients are shown in Fig. 3.18. There is an excellent agreement between the simulated results of the two solvers, which validates the DPS performance.

### 3.3 $90^\circ$ Phase Shifter Based on Substrate Integrated Waveguide Technology for Ku-band Applications

This work introduces a compact phase shifter based on SIW technology. The phase shift of the presented work is  $90^\circ$  with an ultra-flat response. The phase shift has a variation of less than  $\pm 15^\circ$  over the Ku-band. This work is organized as follows. Subsection 3.3.1 introduces the proposed methodology to design non-reciprocal ferrite phase shifters. In subsection 3.3.2, an example in the Ku-band is presented using the described methodology, and then the configuration of the proposed example is modeled and simulated through two commercial packages to validate the proposed design algorithm. Nevertheless, this section (Sec. 3.3) is explained and published at [80].

#### 3.3.1 SIW Phase Shifter Configuration

The configuration of the proposed SIW phase shifter consists of two parallel waveguides (channels) with a common wall. Each channel has two ports, one for the input signal and another for the output. One ferrite tile with suitable magnetization in each channel, it is mounted on the top wall of the SIW channel. The phase shifters in each waveguide are oppositely magnetized to produce a differential phase of  $90^\circ$  between the two channels. The differential phase between the two channels depends mainly on the width, length, height, and position of the ferrite tiles inside the waveguide.

#### 3.3.2 Ku-Band Phase Shifter Example

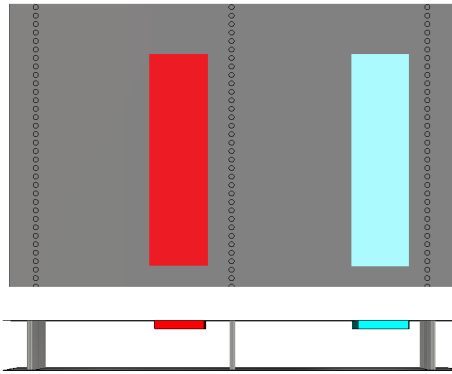


Figure 3.19: SIW phase shifter geometry.

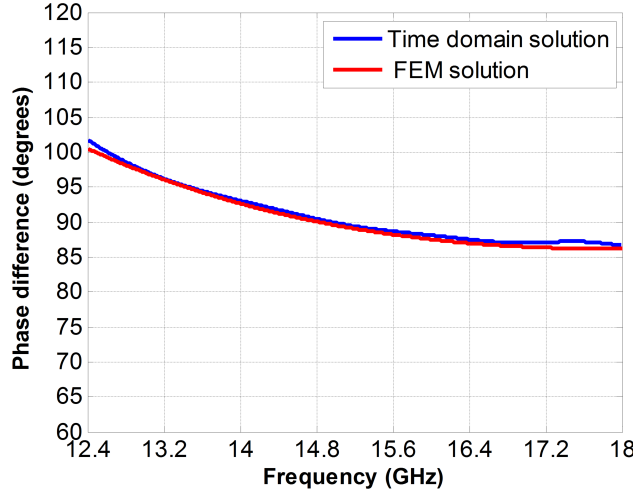


Figure 3.20: Differential phase between the two channels outputs.

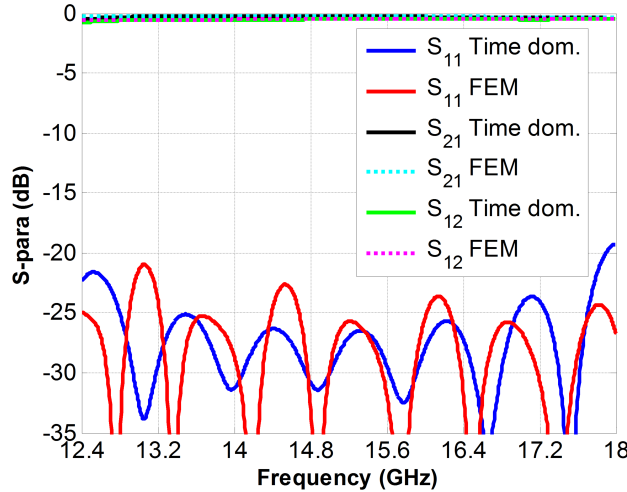


Figure 3.21: Matching and transmission coefficients of the proposed phase shifter.

This section presents a case of non-reciprocal ferrite phase shifter for Ku-band applications. The proposed structure is designed based on SIW technology to be used as a phase shifter in the previous section. The proposed configuration is simulated using two commercial tools to validate the proposed structure results. In Figure 3.19, the proposed phase shifter geometry is shown. The phase shifter is printed on Rogers RT 6002 with an epsilon of 2.94 and a thickness of 3.048 mm. The radius of the vias used in the SIW walls is 0.2 mm, the width of the SIW line is selected to be 9.3 mm. The ferrite tile has a width, height, and length of 2.4 mm, 0.75 mm and 83.5 mm, respectively. The ferrite tile in each channel is placed at the middle distance between the SIW side wall and its center. Also, the ferrite plate is

attached to the top wall of each channel from inside. In Figure 3.20, the differential phase between the output signals of the two channels is shown, and in Figure 3.21 the matching and transmission coefficients are shown. The phase shift, matching, and transmission are extracted through two different numerical solvers in the time domain and in the frequency domain. Both results agree with each other, which validates the phase shift between the two channels.

### **3.4 Circularly Polarized RGW Slot Antenna Fed by Ferrite Based Phase Shifter**

Ridge Gap Waveguide (RGW) technology is a promising technology, especially for the millimeter wave bands. Hence, the need for antennas utilizing the same technology is growing fast to provide complete solutions to the applications in the millimeter wave band. Both linear polarization and circular polarization are deployed in the communication systems depending on the required system needs. Antennas with circular polarization have a remarkable advantage over the linear antennas since they overcome the polarization mismatching and misalignment problems. Here, a circularly polarized antenna that deploys a compact ferrite based differential phase shifter is introduced. The proposed antenna has an impedance matching bandwidth of 16.67% at 30 GHz with a 3 dB axial ratio. Simulations are obtained by two numerical packages, where both results have an excellent agreement with each other.

The main purpose of this work is to show the importance and the applications of the differential phase shifters (DPS) at the millimeter-wave band. Thus, the presented DPS in the previous section is deployed here to improve and enhance the axial ratio of the presented slot antenna.

The traditional guiding structures have many limitations to operate in such bands. Ridge Gap Waveguide (RGW) structures are very promising for these bands. They have many advantages over other structures, such as the absence of dielectric losses, low radiation losses, and wideband operation.

Circularly polarized antennas have the immunity to the multipath interference and the polarization mismatch. Generally, to achieve circular polarization operation there are many methods such as deploying arrays of linearly or circularly polarized antenna elements and feeding them with the proper network [81,82]. Also, a hybrid method can be used to broaden the axial ratio bandwidth [32–34]. The feeding network of such arrays can be realized by deploying differential phase shifters. Moreover, they have also other applications such as the beam scanning antenna systems [31,32,83–85].

This work introduces a circularly polarized antenna using a ferrite differential phase shifter based on RGW technology. As a result, the proposed antenna has a wideband operation in the millimeter band. The following subsections are organized as follows. Subsection 3.4.1 introduces the RGW differential phase shifter. In subsection 3.4.2, the proposed antenna is simulated by utilizing two commercial packages to assure the proposed design performance. It is worth to mention that this section (Sec. 3.4) is published at [86] with more details.

### 3.4.1 Ferrite Based RGW Differential Phase Shifter

The proposed antenna consists of three subsections as shown in Fig. 3.22. A unit cell is designed to cover the targeted frequency band. The unit cell has a square cross-section of length 2.286 mm and height of the same value, while the bed nail has a height of 2.03 mm and a square base cross-section of side length equals 1.02 mm. The proposed unit cell has a band gap from 20 GHz to 38 GHz. The power divider designed has a 50 Ohm input impedance, and it divides the power equally among the two output ports with the same phase. The following stage is the ferrite-based differential phase shifter that has a  $90^\circ$  phase difference. It consists of two channels; each contains a ferrite slab with a suitable magnetization. Each slab has a square shape of 2.286 mm side length and thickness equivalent to the gap between the ridge and the top ground; the material epsilon is 14.2. Moreover, four pins are used for matching purposes. The simulations are performed using two different computation methods. The simulation results of the matching and insertion loss parameters of the power divider connected to the phase shifter are shown in Fig. 3.23(a), while the differential phase shift is shown in Fig. 3.23(b). From these curves, it is clear to say that the matching level is around 20 dB and the maximum phase variation is less than  $10^\circ$  over the entire band. There is an excellent agreement between the simulation results of the two methods, which assures the performance of the structure.

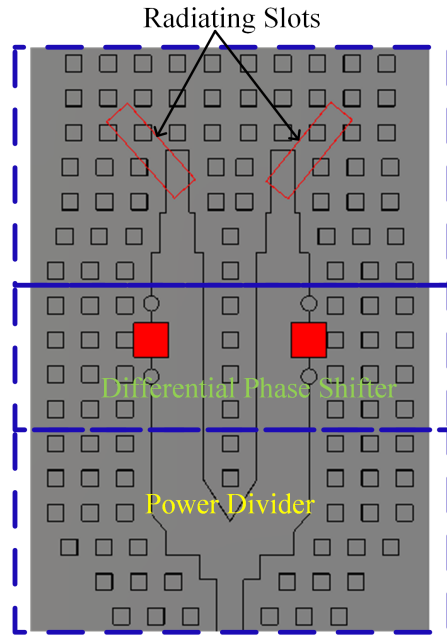
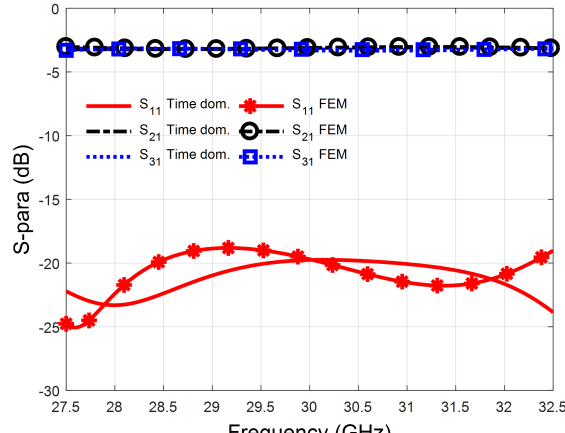
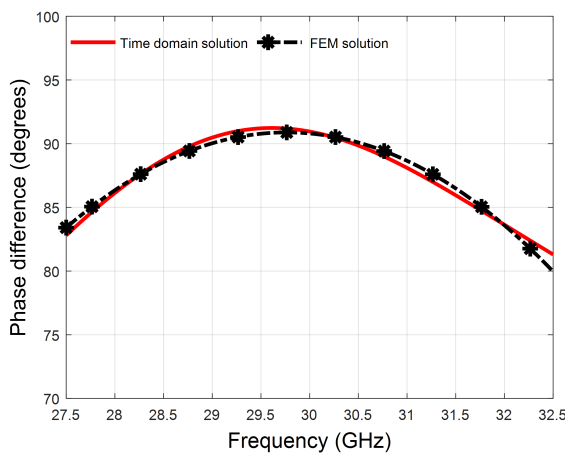


Figure 3.22: The geometry of the proposed antenna (Top ground is hidden).



(a)



(b)

Figure 3.23: Simulations of the RGW power divider connected to the differential phase shifter.  
 (a) Matching and insertion loss. (b) Differential phase shift between the two channels outputs.

### 3.4.2 Circularly Polarized Antenna Design

The proposed antenna shown in Fig. 3.22 is investigated and then simulated with two different methods. The main idea of this antenna is deploying the  $90^\circ$  relative phase difference between the two channels and the  $90^\circ$  by the physical alignment of the slots. Each slot is placed on the top ground of the RGW structure. The right-hand slot has an angle of  $45^\circ$  with respect to the horizontal axis while the left slot has  $-45^\circ$ . The simulation results of the antenna matching and the axial ratio are shown in Fig. 3.24, while the radiation pattern of the proposed antenna at the center frequency (30 GHz) is shown in Fig. 3.25. It is clear to say that the simulation results done by two methods have an excellent agreement with each other, which validates the performance of the proposed antenna.

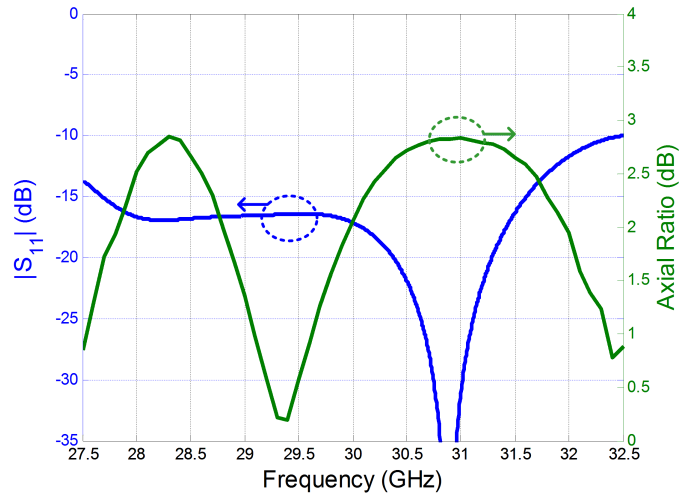


Figure 3.24: Simulations of the proposed antenna (Reflection coefficient magnitude and axial ratio).

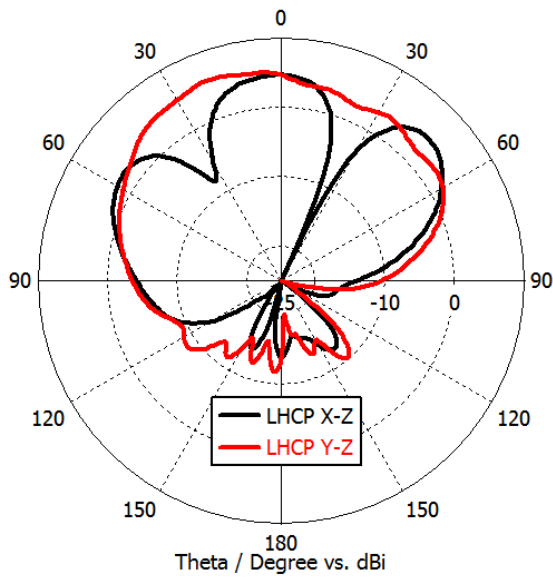


Fig. 3.25: Simulations of the proposed antenna (Radiation pattern at 30 GHz).

# Chapter 4

## Design and Analysis of Orthomode Transducers

In this chapter, reciprocal devices that are responsible for combining and separation of two orthogonal polarized signals are discussed. Such devices are the Orthomode Transducers (OMTs). There are three categories of these devices, the two-fold symmetry, the one-fold symmetry, and the asymmetric. The history of such devices is presented in the literature review chapter in this thesis. OMT is a very critical device that is attached to the antenna system. Such a device is mainly used for the antenna feeding structures that support two propagating modes aiming to maximize the bandwidth efficiency of communication channels.

Three new OMT structures are proposed and validated in this chapter, each of them falls in a different category. Two of the proposed OMTs are implemented by the waveguide technology, while the other deployed the groove gap waveguide technology. The overall performance of the presented OMTs is improved compared to other published ones. This includes the matching level, the isolation level, and the insertion loss. Moreover, they have more compact size than other OMTs.

The proposed concepts for the presented OMTs can be applied to any frequency band. Considering the limitations of the CNC machines and their relatively lower accuracy for the very small dimensions of the millimeter wave devices. The first two proposed OMTs concepts are validated by prototyping such structures after scaling them to a lower frequency band. Moreover, the needed modifications to such designs are done so that they have a standard waveguide for each polarization port. Thus, the machining has more acceptable tolerance and reasonable fabrication price. This also reflects in the accuracy of the measurements. Nevertheless, their examples at the millimeter wave band are simulated and presented at the end of each part that corresponds to each presented OMT.

The third proposed OMT is presented in the last section of this chapter. It is not scaled and its prototyping is made to be measured at the 30 GHz frequency band. It is the first of its kind since it is based on the groove gap waveguide technology. This provides the OMT

with enormous advantages such as avoiding the necessity of electrical contact without any leakage problems. Each OMT design is explained and investigated in a separate section.

## 4.1 Compact Full Band OMT Based on Dual Mode Double Ridge Waveguide

A nonstandard dual mode double-ridge waveguide is utilized to design a compact Orthomode Transducer (OMT). The OMT is terminated with a standard circular waveguide common port and two standard isolated rectangular waveguide ports. The proposed structure exploits a one-fold symmetry to eliminate the coupling to the in-band higher order odd modes within the common port. Furthermore, the performance of the proposed OMT design is verified through a back-to-back measurement showing an excellent agreement between the full-wave simulations and measurements. Nevertheless, the proposed design achieves a measured matching level of 19 dB for the two modes and isolation level between them beyond 30 dB over the entire band.

With the increasing demand for a wideband and compact size for OMT for space application, this work presents a novel design concept for a compact and simple one-fold OMT based on a dual-mode double-ridge waveguide to meet such a challenge. The orthogonality of the modes in the double ridge waveguide is deployed to design a full K1-band OMT having a standard circular common port as well as two standard rectangular waveguides (WR-51) isolated ports. In addition, a study on the nature of the propagating modes in the core part of the design is presented followed by the design procedure. Moreover, prototypes for the proposed design are presented to verify the performance through a back-to-back configuration. Moreover, the proposed OMT is discussed in details and published at [87]. Nevertheless, the main contributions in this section can be summarized as follows:

- Introducing the proposed double ridge compact OMT design in Sec. 4.2.2.2
- Presenting the modal analysis of the core part of the dual mode double ridge waveguide in Sec. 4.1.1.2
- Displaying the prototypes and measurement results and validation in Sec. 4.2.3

### 4.1.1 OMT Design Concept

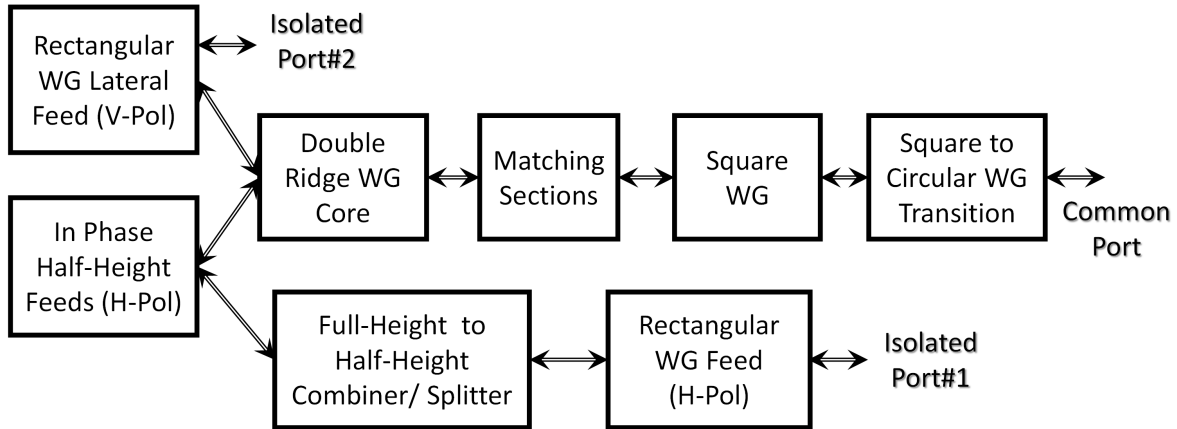


Figure 4.1: Block diagram for the proposed OMT.

A block diagram of the proposed OMT is shown in Fig. 4.1 illustrating the common circular port and the two isolated rectangular ports associated with the orthogonal polarizations. The main design concept is to use a one-fold symmetric excitation type to avoid the undesired coupling to the in-band higher order modes that typically exist within the circle or square cross-section waveguides. Furthermore, the proposed design topology features an inline arrangement to achieve the compactness of the structure without tolerating the bandwidth and port isolation.

#### 4.1.1.1 Design Interfaces

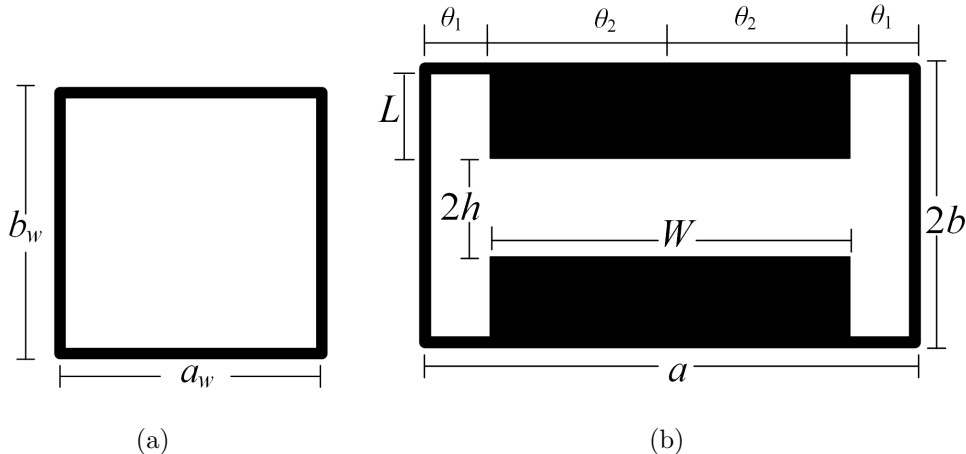


Figure 4.2: The proposed OMT interface section configuration. (a) Square waveguide cross section. (b) Dual-mode double ridge waveguide cross section.

Table 4.1: Double Ridge Waveguide Dimensions.

Parameter	Dimension (mm)	Parameter	Dimension (mm)
$a$	19.558	$2b$	12.954
$w$	12.954	$L$	3.2385
$2h$	6.477	$\theta_1$	3.302
$\theta_2$	6.477		

The realization of the presented concept within this work requires following the industrial standard for the K1-band. Typically, the K1-band circular waveguide has a diameter of 11.938 mm, and its operating band is from 17.5 GHz to 20.5 GHz. To simplify the matching requirements between the different parts of the proposed OMT, the circular waveguide opening is interfaced to a square waveguide to be of the same coordinates of the double ridge waveguide as shown in Fig. 4.2. As the square waveguide will be connected directly to the K1-circular waveguide, its cutoff frequency has to be close to the circular waveguide to simplify the matching within a compact structure. Therefore, the selected dimensions of the square waveguide are  $a_W = b_W = 10.16$  mm as shown in Fig. 4.2(a). Furthermore,  $a$ ,  $2b$ ,  $2h$ ,  $w$ ,  $L$ ,  $\theta_1$ , and  $\theta_2$  are the double ridge parameters based on Fig. 4.2(b), these dimensions are tabulated in Table 4.1. The isolated ports follow the standard WR-51 rectangular waveguide to comply with the desired frequency band. The dimensions of the double ridge sections are selected to merge one full-height central WR-51 port with two half-height WR-51 ports on both sides. The mathematical formulation for the design impedance matching for both polarizations is given in Appendix B.

#### 4.1.1.2 Double Ridge Waveguide Modal Analysis

In this subsection, the possible propagating modes within the band of interest inside the double ridge waveguide are studied. This study uses the Eigenmode solver of CST to predict the propagating modes to define the operating range of the presented OMT core as well as the nature of the operation, which includes the bandwidth limit, guard bands, and the dual mode matching. Fig. 4.3(a) shows the dispersion relation of the objective double ridge structure with the selected dimensions. The electric field distribution of all modes within the operating frequency band of double ridge waveguide is shown in Fig. 4.3(b). As this section is excited by a square waveguide carrying two orthogonal modes, any mode with odd field distribution will be suppressed. The first mode starts at 6.11 GHz, which is the double ridge waveguide dominant mode. This mode can be coupled to the vertical mode of the OMT input. The second mode has a cutoff frequency of 12.78 GHz, and this mode is not supported because all the electric field has an odd symmetry. Mode 3 has a cutoff frequency of 13.1 GHz, and it

has the desired electric field distribution that can couple to the horizontal mode of the OMT common port. Modes 4 and 5 are not supported due to their odd symmetry.

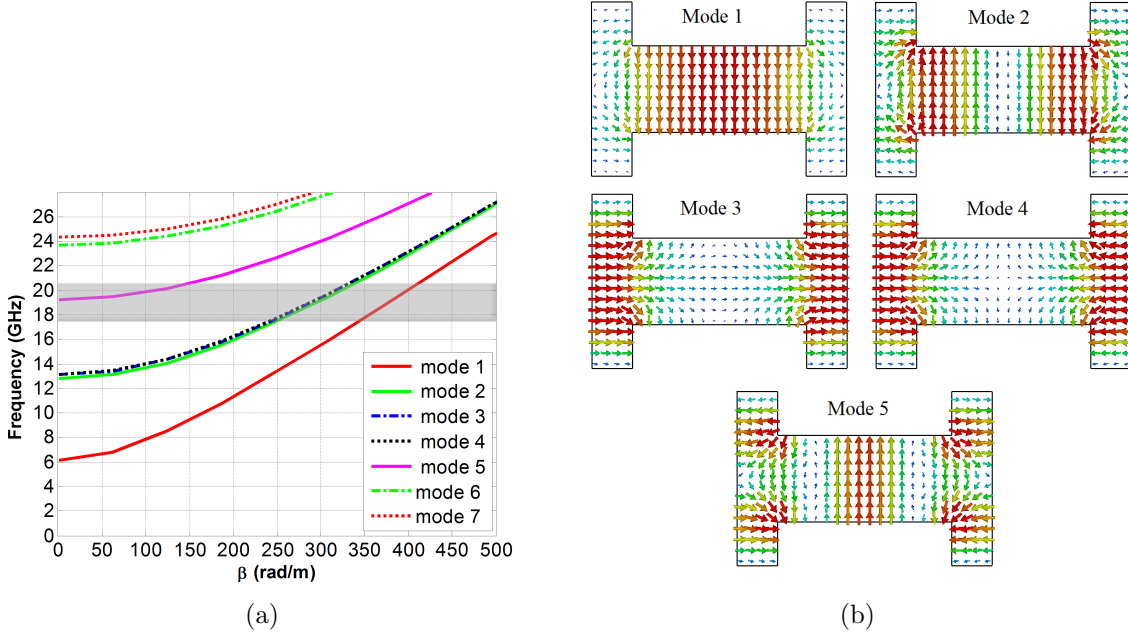


Figure 4.3: Proposed OMT interface section configuration. (a) Dispersion diagram of the dual-band double ridge waveguide. (b) Field mode patterns of the modes propagating within the operating bandwidth.

The nature of the dispersion diagram shown in Fig. 4.3 indicates that the propagation constants for the two modes of interest are different. This has an implication on the achievable matching level for both modes as shown in section III-A. In addition, the proposed structure cannot have the same operating band for the WR-51 (15-22 GHz) to respect a guard band from the cutoff frequency of mode 3. Therefore, one of the limitations of the proposed design is the limited achievable bandwidth in comparison to the two-fold designs available in the literature.

#### 4.1.2 OMT Design Description

The proposed OMT configuration is composed of three cascaded sections. The first section is the main OMT junction that is responsible for the dual polarization behavior and isolation, which is the double ridge waveguide core in Fig. 4.1. The following section is the space eliminator that aims to make the ports of the horizontally polarized signal adjacent and very close to each other. The third part is a power combiner that collects the horizontally polarized signals, which is a full-height to a half-height combiner/splitter in Fig. 4.1. Each part is designed and optimized separately in order to minimize the small reflections and

improve the overall transmission. Then, all these parts are connected together, simulated, fabricated, and measured.

#### 4.1.2.1 OMT Core

The first section is the OMT main junction in which the two polarizations are separated. This section is a four-port network from an electrical perspective. Port 1 is a square waveguide in which vertical and horizontal signals are excited corresponding to the dominant  $TE_{10}$  and  $TE_{01}$  modes. The vertically polarized signal is transferred to port 2, each of the other ports (port 3 and 4) accepts half the horizontally polarized signal. The 3D two orthogonal sectional views of the OMT main junction and its simulation results are shown in Fig. 4.4, and Fig. 4.5, respectively. The dimensions of the matching transformer used for the proposed OMT matching are shown in Table 4.2. The mathematical formulation of the impedance matching transformers is explained in Appendix B.

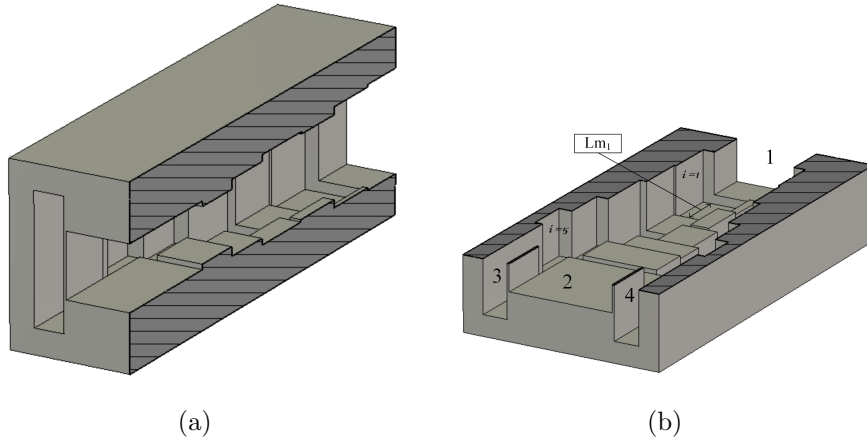
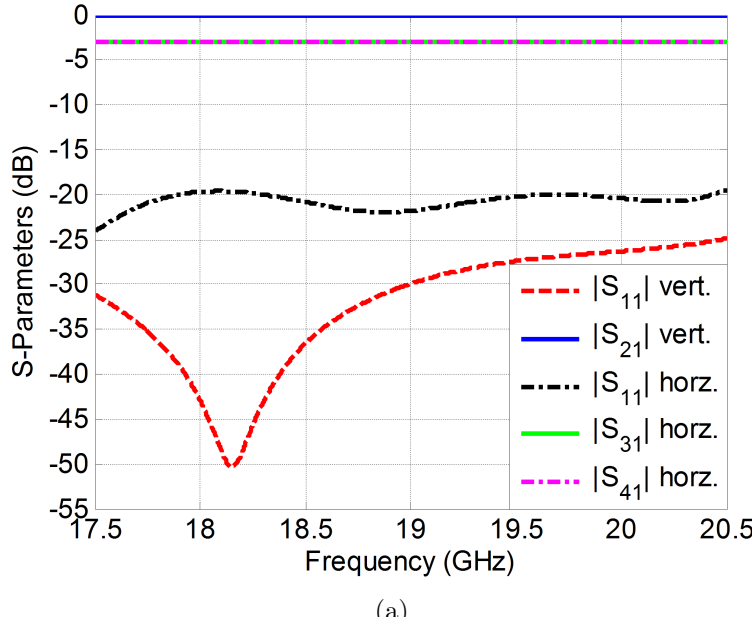


Figure 4.4: The proposed OMT 3D. (a) Vertical sectional view. (b) Horizontal sectional view with port numbers indicated.

Table 4.2: Matching Transformers Dimensions.

Sec. $i$	$a_i$ (mm)	$2b_i$ (mm)	$W_i$ (mm)	$L_i$ (mm)	$Lm_i$ (mm)
1	12.954	12.446	1.016	1.27	6.096
2	13.462	11.684	2.286	1.778	5.842
3	15.24	13.208	4.572	2.286	7.112
4	18.034	11.43	7.62	2.032	5.334
5	21.336	11.176	9.398	2.794	5.08



(a)

Figure 4.5: The proposed OMT matching and transmission simulation results.

#### 4.1.2.2 Assembly Elements

The first element is the space eliminator and power combiner at the same time, which is responsible for eliminating the physical space between the ports of the horizontally polarized signals to make them adjacent to each other. Also, it is the power combiner and its responsibility for collecting the horizontally polarized signals from the adjacent waveguides and combine them. The 3D geometry sectional view of the section and its simulation results are shown in Fig. 4.6(a). The next section is the  $90^\circ$  bend; it is designed to be attached to the port of the vertically polarized signal in order to create physical space separation between the two output ports of both modes. The 3D sectional view of this waveguide E-Plane bend and its simulation results are shown in Fig. 4.6(b). The last element is circular to square waveguide transition. It is connected between the antenna to the OMT. It is a transition between circular waveguide of type K1 with a diameter of 11.938 mm to a square waveguide of side length 10.16 mm. The 3D view of this transition and its simulated results are shown in Fig. 4.6(c).

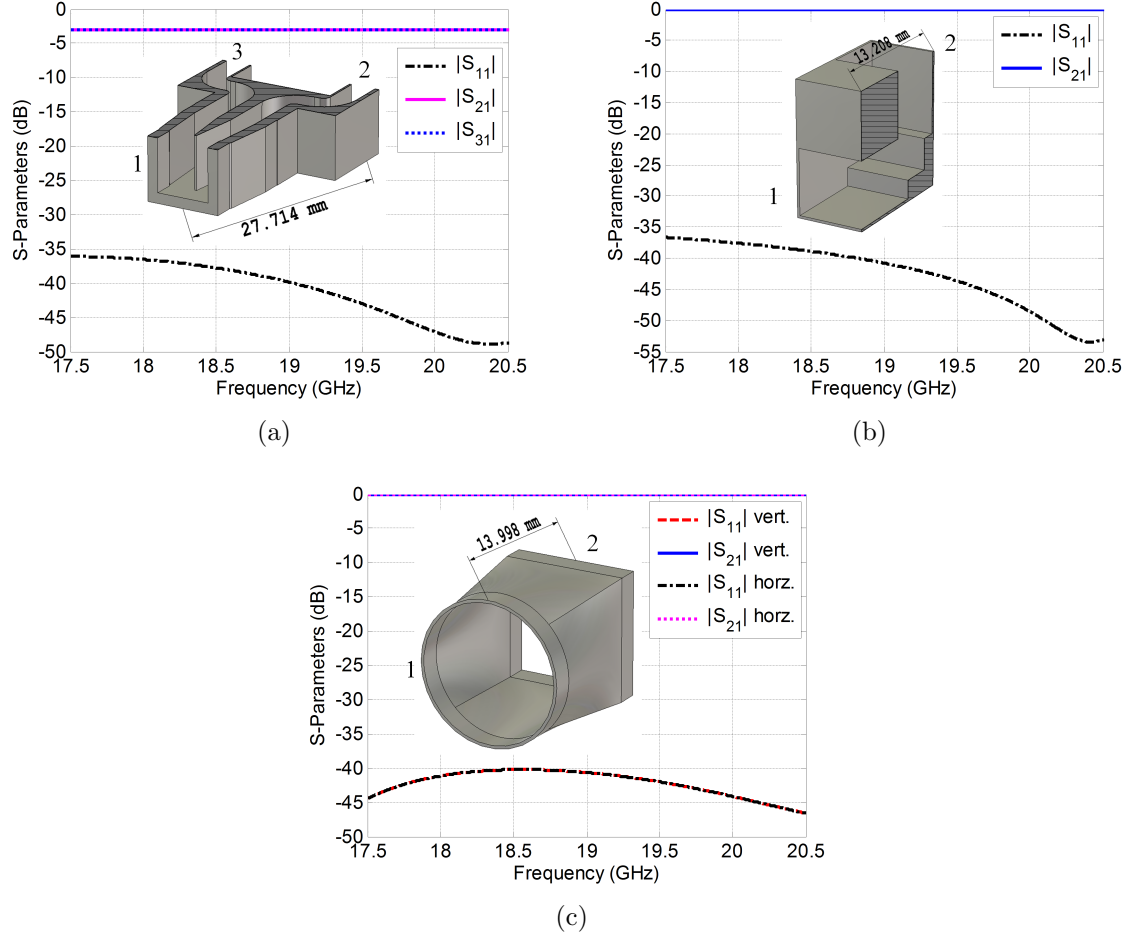


Figure 4.6: Assembly elements response. (a) Space eliminator and a power combiner. (b) 90° bend section. (c) Circular to the square waveguide.

#### 4.1.2.3 Entire OMT

The proposed OMT with all its sub-blocks is simulated using two commercial tools to validate the results before fabrication. The whole configuration of OMT with sectional views, 3D with dimensions, and the simulation results are shown in Fig. 4.8(a), Fig. 4.8(b), Fig. 4.8(c), and Fig. 4.8(d), respectively.

However, the reflection coefficient magnitudes shown in Fig. 4.8(d) have a difference in magnitude; this difference does not affect the OMT operation because it is very small (if converted from dB to ratio). Since the matching level is already acceptable, then the transmission of each polarization is more critical. In other words, the difference in matching parameters can be accepted, if and only if, the aimed matching and the transmission levels of each polarization is achieved.

It is worth discussing the power handling of the entire OMT briefly. Theoretically, both the standard waveguides WR-51 (each polarization port) and K1 (the common port) can handle power up to 801 kW, and this reflects into the maximum electric field of less than  $3 \times 10^6$  V/m (or 75 kV/in). Meanwhile, the whole OMT can handle up to 722.5 kW theoretically, which corresponds to the same value of the electric field. In other words, the power handling of the OMT is decreased by 9.8% of the maximum power that the standard waveguides can handle. The stated above values are calculated by the formulas given by [8]. Moreover, to verify such values simulations have been done and shown in Fig. 4.7.

Practically, these values are too high to operate. Thus, the maximum allowed value in industry is usually only 10% of the theoretical maximum power to operate safely without any sparks or failure of the structure. In other words, the practical maximum power of the proposed OMT is 72.25 kW. Nevertheless, this value should be avoided, and the power of the propagating signal should be lower than that.

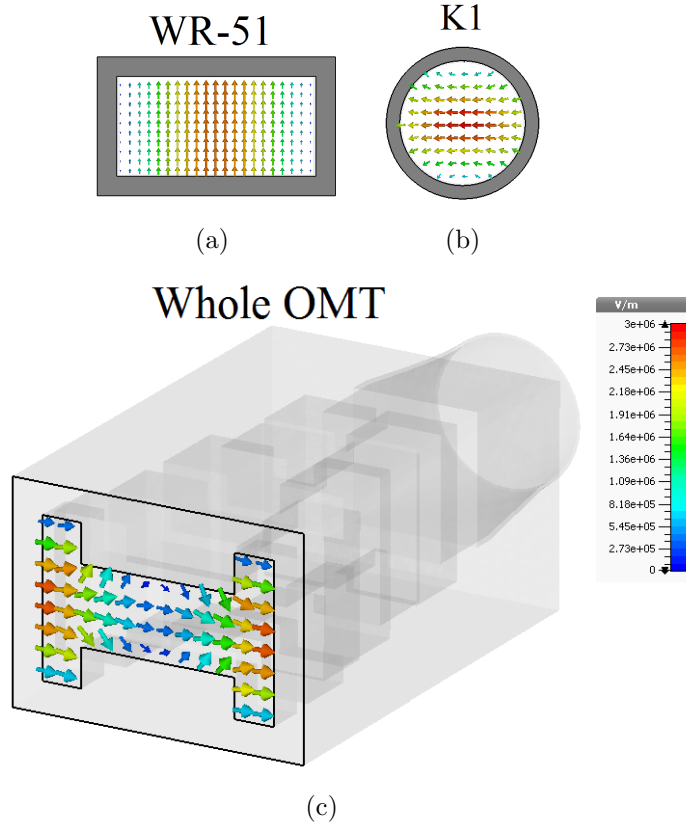


Figure 4.7: OMT theoretical maximum power simulation results. (a) Standard rectangular waveguide WR-51. (b) Standard circular waveguide K1. (c) Whole OMT.

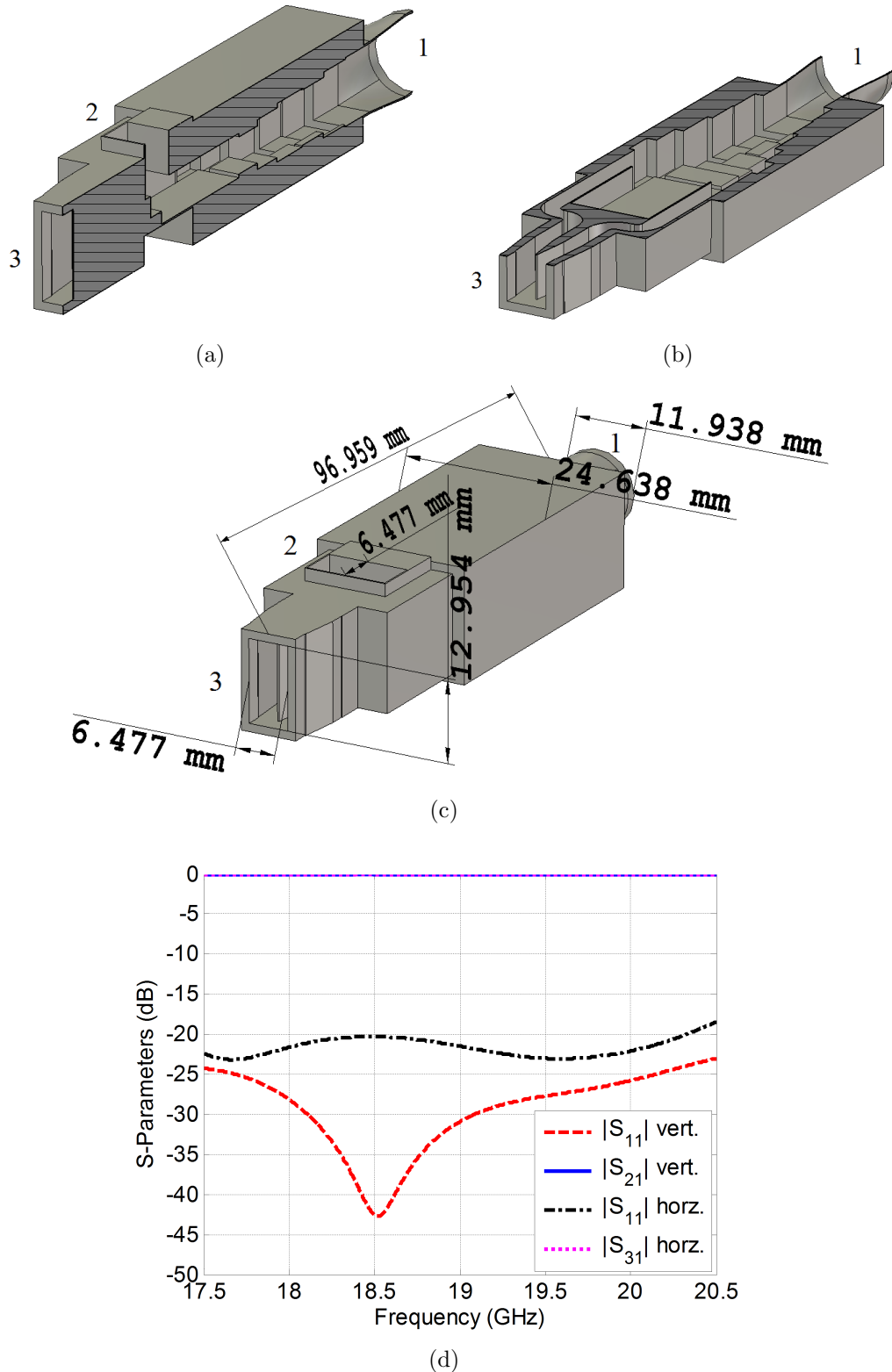


Figure 4.8: Whole OMT. (a) Vertical sectional view with port numbers indicated. (b) Horizontal Sectional view with port numbers indicated. (c) 3D structure with dimensions. (d) Simulation results.

### 4.1.3 Validation and Experimental Results

The proposed methodology presented in Sec. 4.2.2.2 that has been used in the proposed example of OMT that is shown in Sec. 4.1.2 needs to be validated experimentally. This validation can be done in several ways. The first way is by connecting the proposed OMT to a matched load that can absorb all the propagating modes. The second method is to use a conical horn antenna that is working in the same frequency band instead of the matched load. The third way is to connect two OMTs to each other, and this setup can be just two OMTs connected together without any rotation or rotating one of them by  $90^\circ$  to make sure that the insertion loss pass is identical to the two propagating modes. This way is selected for fabrication and measurements to validate the proposed OMT. This setup is more comfortable and more reliable in our case for measurements since the measuring ports are only four ports, each having one propagating mode. The proposed OMT in the back-to-back setup is also simulated before fabrication. Finally, it is fabricated and measured. The proposed OMT is manufactured using CNC machines with a tolerance of  $\pm 0.127$  mm. The OMT prototype is shown in Fig. 4.10, the material utilized in the fabrication is the brass alloy (not gold-plated). Such an alloy is selected because of its rigidity and hardness which assures that all the features of the structure are as precise as possible. The measurement setups with the port numbers are shown in Fig. 4.9. The simulated results are compared with measurements and shown in Fig. 4.11. As shown in this figure, there is excellent agreement between simulations and measurements. The measured insertion losses for both cases (with and without rotation) are acceptable and have an average value of 1 dB. Fig. 4.11(c) shows the measured isolation between the two orthogonal polarizations in the back-to-back setup, where it exceeds 25 dB all over the operating bandwidth. It is worth mentioning that there is a slight discontinuity in the isolation curve. This curve discontinuity is a result of fabrication tolerance especially at the center of the structure. The fabrication is performed by Matsuura-VX1000, where the expected tolerance is in the range of  $\pm 0.127$  mm. The walls that separate the sections of the horizontal and the vertical polarizations are very thin and fabricated out of two unequal halves, where the alignment is difficult and may cause such problems. Moreover, in the measurement setup, we need two identical OMTs, which is very difficult to achieve considering the machine tolerance. Nevertheless, each OMT is made from two halves that are fabricated separately which is difficult to assure their symmetry. Third, to assure the electrical contact between the two halves, an excessive number of screws are used on the edges instead of the middle of the OMT. Also, an extra screw is used in the middle of each OMT as shown in Fig. 4.10.

It should be stated that the results can be improved by redesigning the unit and increasing

the thin wall thickness to be around 0.508 mm instead of 0.254 mm. This will facilitate the alignment process and hence, reduce the possibility of measurement imperfections.

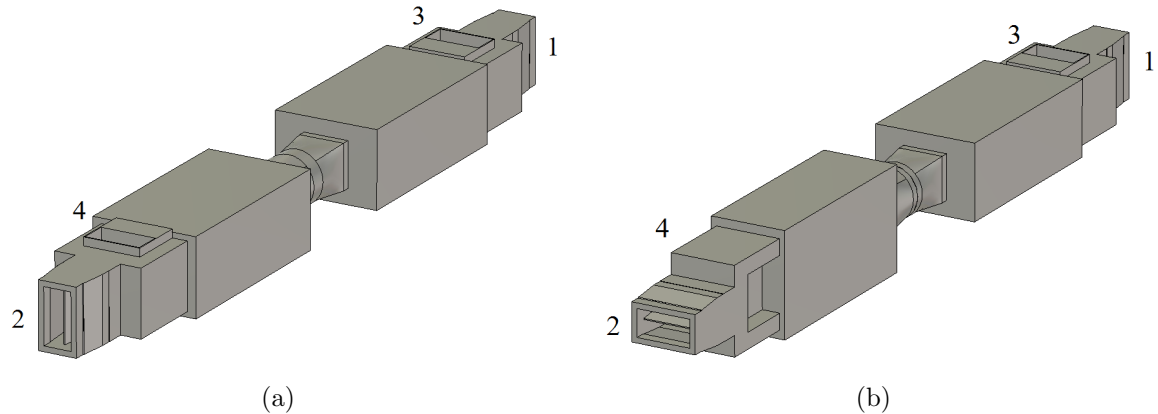


Figure 4.9: OMT back-to-back setup with port numbers. (a) Without rotation angle. (b) With 90° rotation angle.

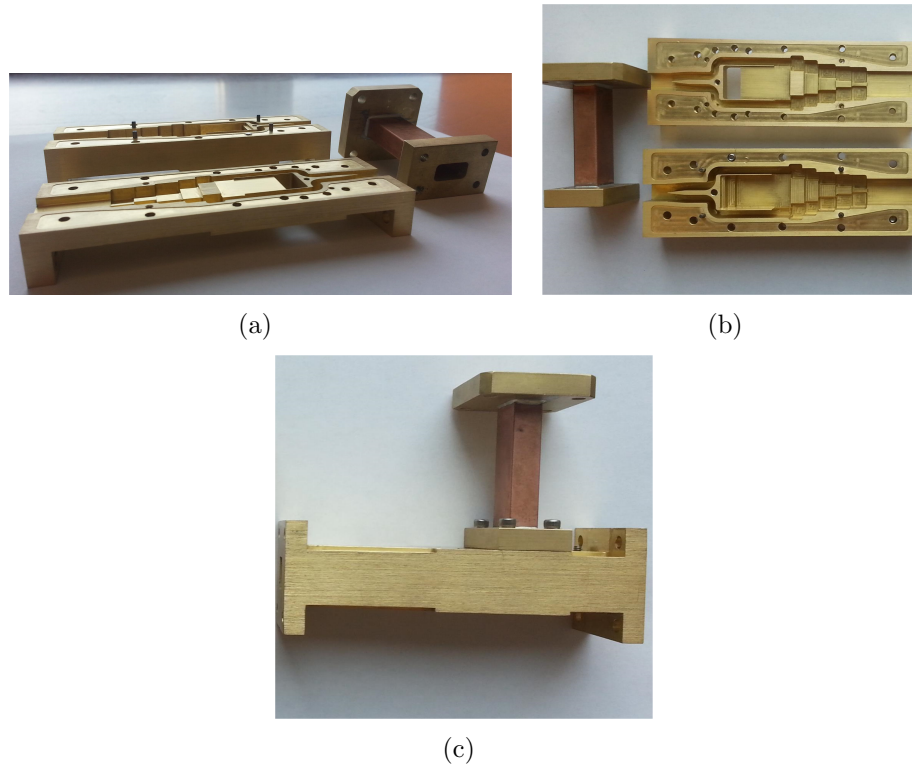


Figure 4.10: Proposed OMT Parts. (a) 3D view. (b) Top view. (c) After assembly.

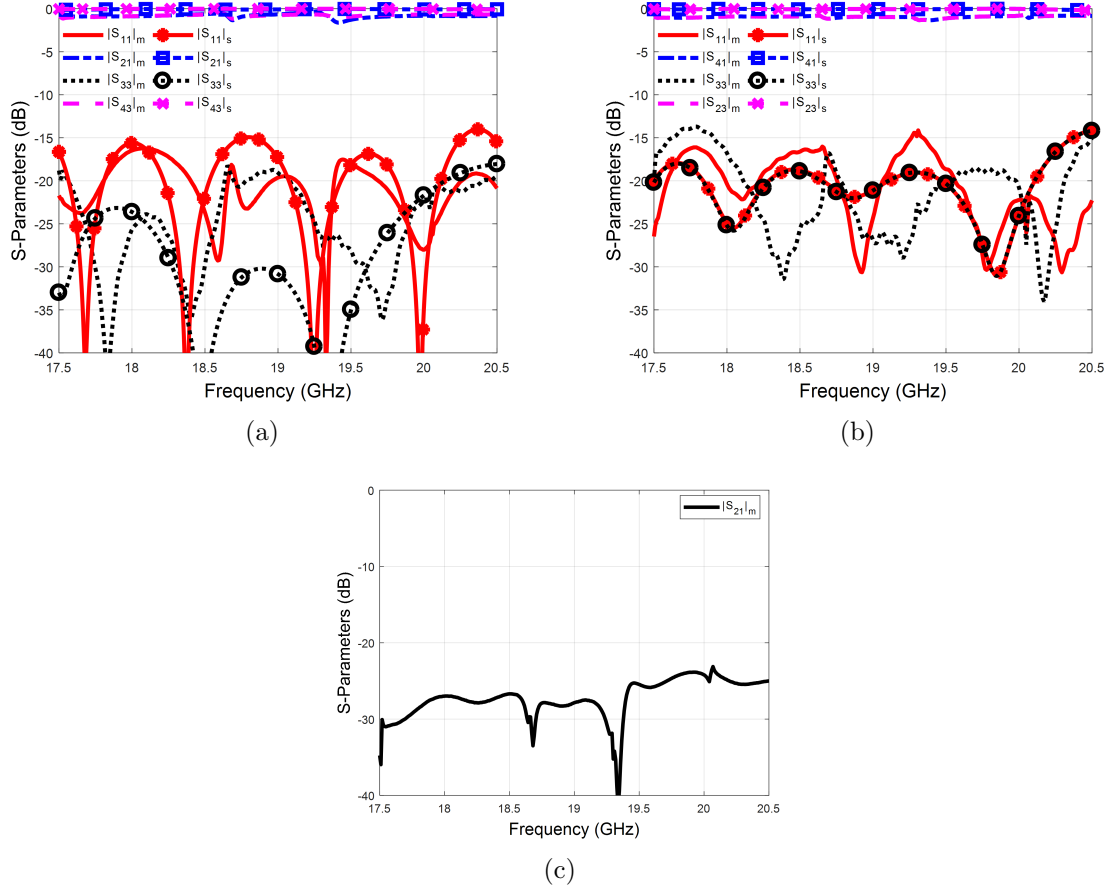
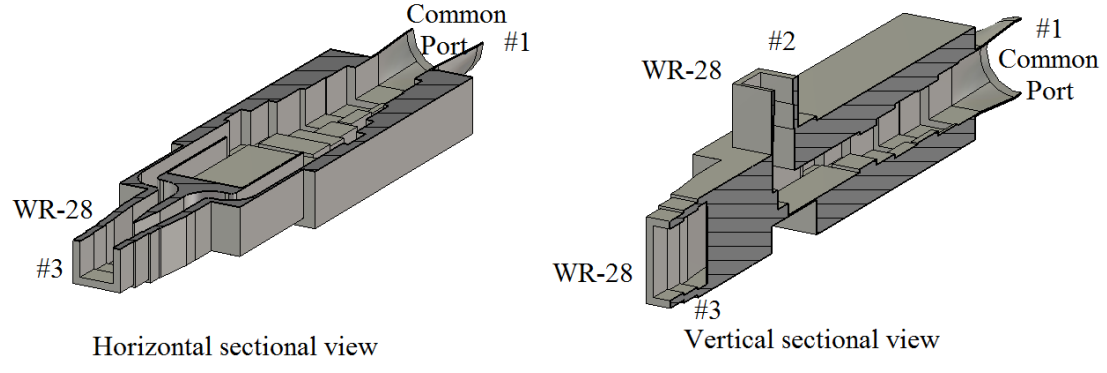


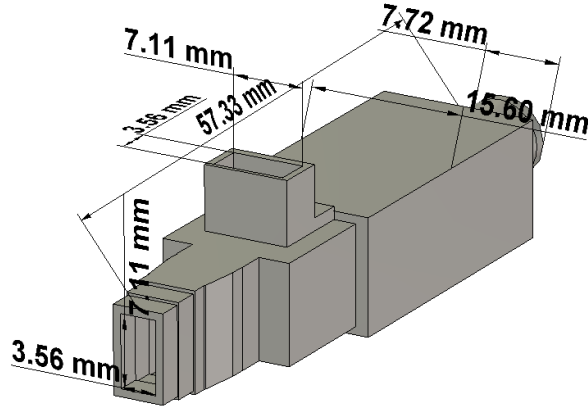
Figure 4.11: OMT results using back-to-back setup. (a) Simulations and measurements without rotation angle (matching and insertion loss). (b) Simulations and measurements with  $90^\circ$  rotation angle (matching and insertion loss). (c) Simulations with  $90^\circ$  rotation angle (measured far coupling).

#### 4.1.4 Higher Frequency bands Validation

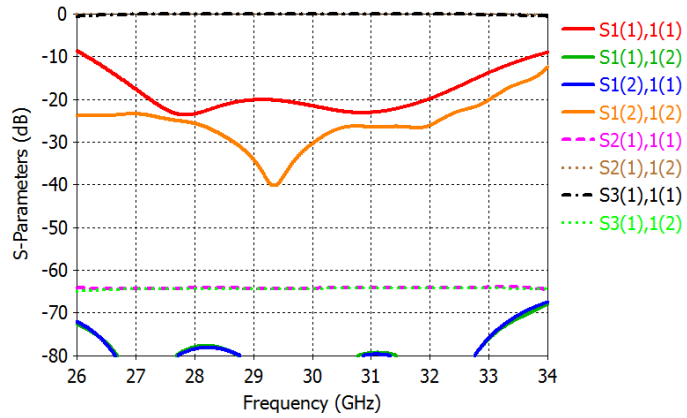
In this section, the structure and the simulated results of the proposed OMT at the millimeter wave band are presented. Some modifications have been made to the design to make it fractional for the 5G applications such as the two polarization ports are now WR-28 instead of WR-51. The internal dimensions of the fabricated OMT are simply scaled to the 30 GHz band as shown in Fig. 4.12(b), but one step impedance transformer is added to each polarization port to improve the matching level. This validates that the proposed concept can be applied to any frequency band. The fabrication was done at a lower frequency band because of the machining limitations as explained before. The simulation results shown in Fig. 4.12(c) have the same behavior of the scaled fabricated one. The structure of such OMT of the 30 GHz band is shown in Fig. 4.12(a).



(a)



(b)



(c)

Figure 4.12: Proposed OMT at 30 GHz band. (a) Structure 3D sectional views with port numbering. (b) Dimensions of the 3D structure. (c) Simulation results.

## 4.2 Asymmetric Compact OMT

A compact asymmetric OMT with high isolation between the vertical and horizontal ports is developed. The basic idea of the design is to deploy combined E- and H-plane bends within the common arm. Moreover, an offset between each polarization axis is introduced to enhance the isolation and decrease the size to be around one-third of most of the existing asymmetric OMTs. The OMT achieves better than 22.5 dB matching level and 65 dB isolation between the two modes. Good agreement is obtained between measurements and full-wave simulations.

In this work, we are targeting to reduce the overall weight of the system. Thus, a compact OMT is designed, fabricated, and presented. The launching cost for the satellite applications can exceed 18,000\$ per kg. In other words, such cost will be reduced if the system components are more compact and weigh less. The presented OMT that falls in the asymmetry class. The proposed design utilizes the combined E and H-plane bends within the common arm. Moreover, an offset between the polarization ports has been introduced to enhance the isolation. Compared to most of the published asymmetric OMTs, the proposed OMT size is around one-third. It is worth to mention that the proposed asymmetric OMT is explained more and published at [88].

### 4.2.1 Physical Alignment of OMT Ports

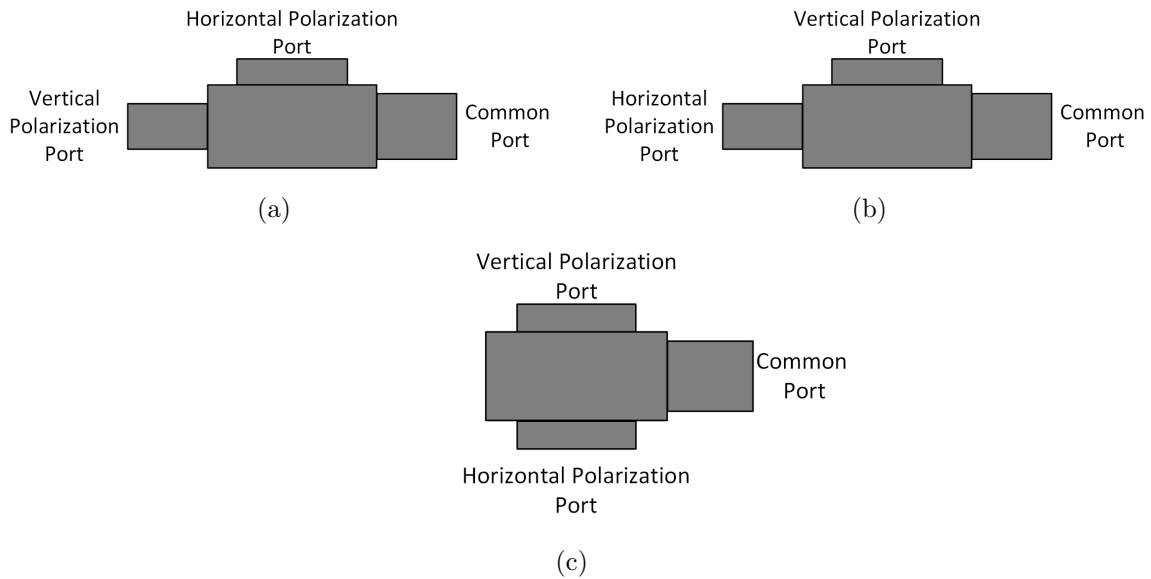


Figure 4.13: Traditional OMT structure. (a) Side view of V-Pol. inline. (b) Side view of H-Pol. inline. (c) Plane view of Non-inline.

The physical alignment of the OMT ports may have different forms as shown in Fig. 4.13 depending on the required mechanical consideration of the system where this OMT is going to be utilized. Figs. 4.13(a) and 4.13(b) show the most commonly used configurations of OMTs where one of the polarization ports is in-line with the common port and the other is orthogonally transverse to the other two ports. Physically, the port that is in-line with the common port can hold either the horizontal or vertical polarization. However, usually vertical polarization is preferred to this port [53, 64]. These structures are more comfortable to match due to the physical alignment of the ports. In some systems, vertical and horizontal polarization ports need to be placed in opposite directions as shown in Fig. 4.13(c). In this case, there are two solutions. The first one is using the traditional configurations shown in Figs. 4.13(a) and 4.13(b) and adding E or H-plane bend, which results in a relatively larger structure. Meanwhile, the second solution is to deploy both of E and H-plane bends in the common arm in a combined form, which provides a compact structure.

#### 4.2.2 Combined OMT Design Methodology

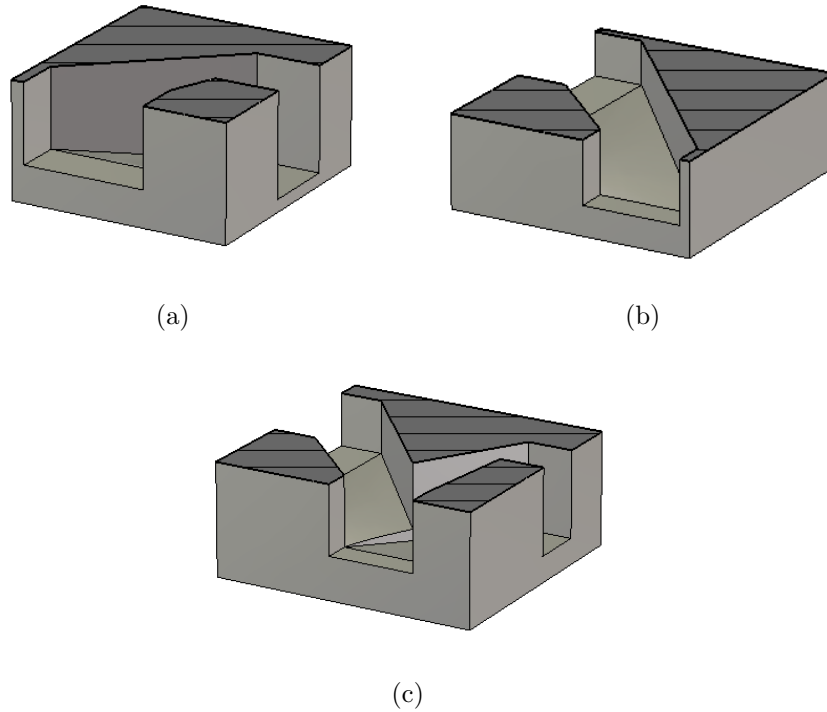


Figure 4.14: Bends sectional view. (a) E-plane. (b) H-plane. (c) E- and H-plane.

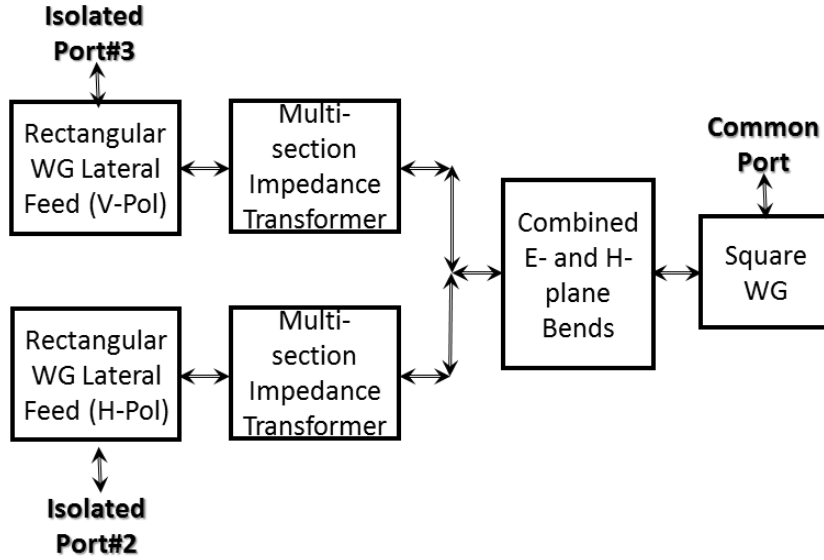


Figure 4.15: Block diagram of the proposed OMT methodology.

The problem discussed in the previous section has two solutions. The first solution is to add E- and/or H-plane bends, such bends are shown in Figs. 4.14(a) and 4.14(b), respectively. They can be added to the traditional OMT structure, which makes the design size larger. The second, combine both E- and H- bends in the OMT core itself as shown in Fig. 4.14(c). The second solution makes the structure more compact but complicates achieving the required matching and isolation levels. On the other hand, such a structure provides more freedom in aligning each polarization port independently. It should be stated that the proposed physical alignment of the OMT ports is the most difficult and challenging task. The design methodology of the combined OMT is summarized in the block diagram shown in Fig. 4.15.

#### 4.2.2.1 OMT Description

The proposed OMT is composed of three ports, common port, horizontal, and vertical port. The common port has a square cross-section of side length  $0.8''$ . Each of the other ports is a WR-112 standard rectangular waveguide of dimensions  $1.112'' \times 0.497''$  (28.50 mm  $\times$  12.62 mm).

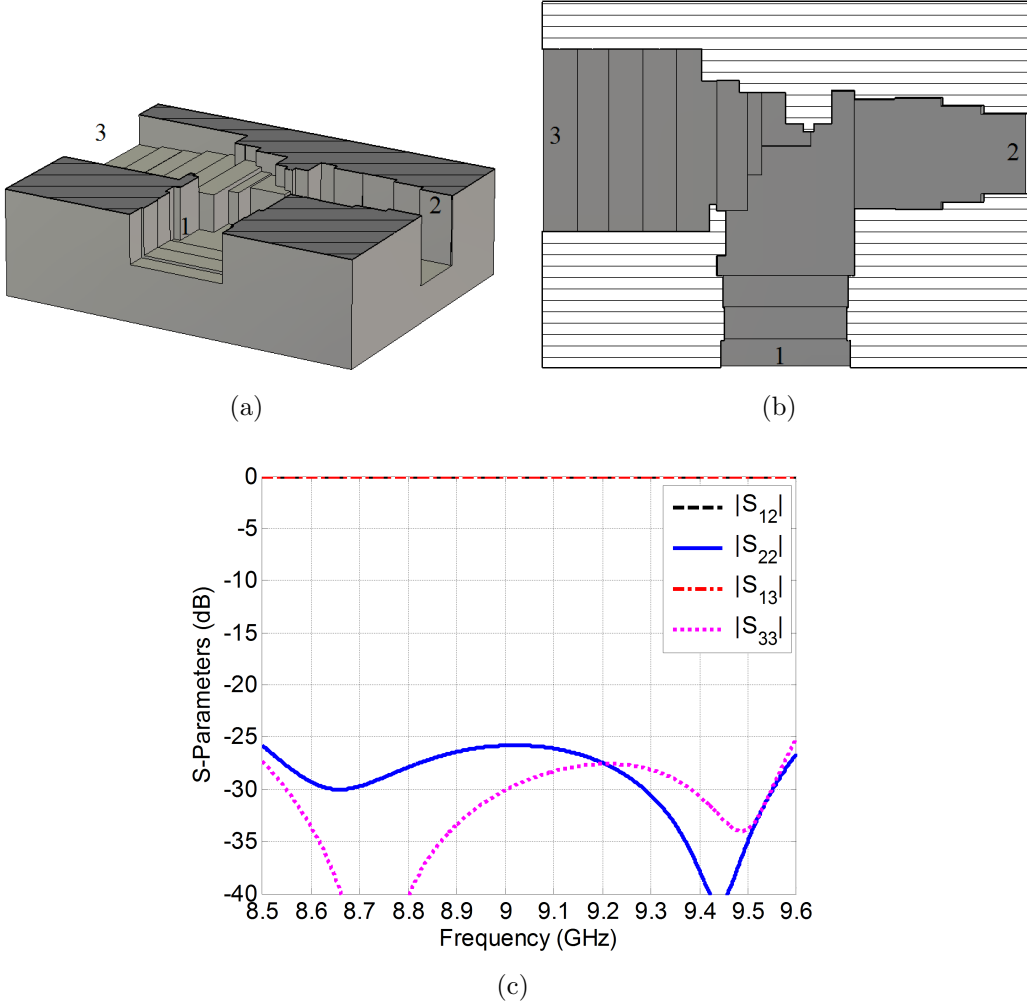


Figure 4.16: The proposed OMT without offset. (a) 3D horizontal sectional view. (b) Plane horizontal sectional view. (c) Simulation results.

The basic idea is using both of E- and H-plane bends in the structure's core as explained in the previous section. Moreover, multiple-section impedance transformers are added to each port in order to improve the matching level. The 3D sectional view and the planar horizontal sectional view of the designed OMT are shown in Fig. 4.16. This structure achieves better than 25 dB matching level for both modes and isolation better than 60 dB as shown in Fig. 4.16(c). The proposed design is investigated and simulated using CST simulator; the simulation results are shown in Fig. 4.16(c).

#### 4.2.2.2 Offset OMT Design

The proposed structure has excellent isolation. However, this isolation can be improved by introducing a small offset between the center axis of each polarization. Introducing this little

offset in the proposed design improves the isolation level by more than 5 dB with a slight reduction of the OMT size.

This offset is placed intentionally between the centers of Port 2 and 3 to reduce the coupling level between them. This offset avoids having the maximum electric field of each waveguide from being on the same axis. If the maxima are on the same axes, strong undesired modes due to the discontinuities in the transformers are excited, which eventually increase the coupling that reduces the isolation. In addition, the common port is shifted more towards the direction of Port 3, which is introduced intentionally to satisfy the geometry requirements. Other specs requirements may lead to different configurations.

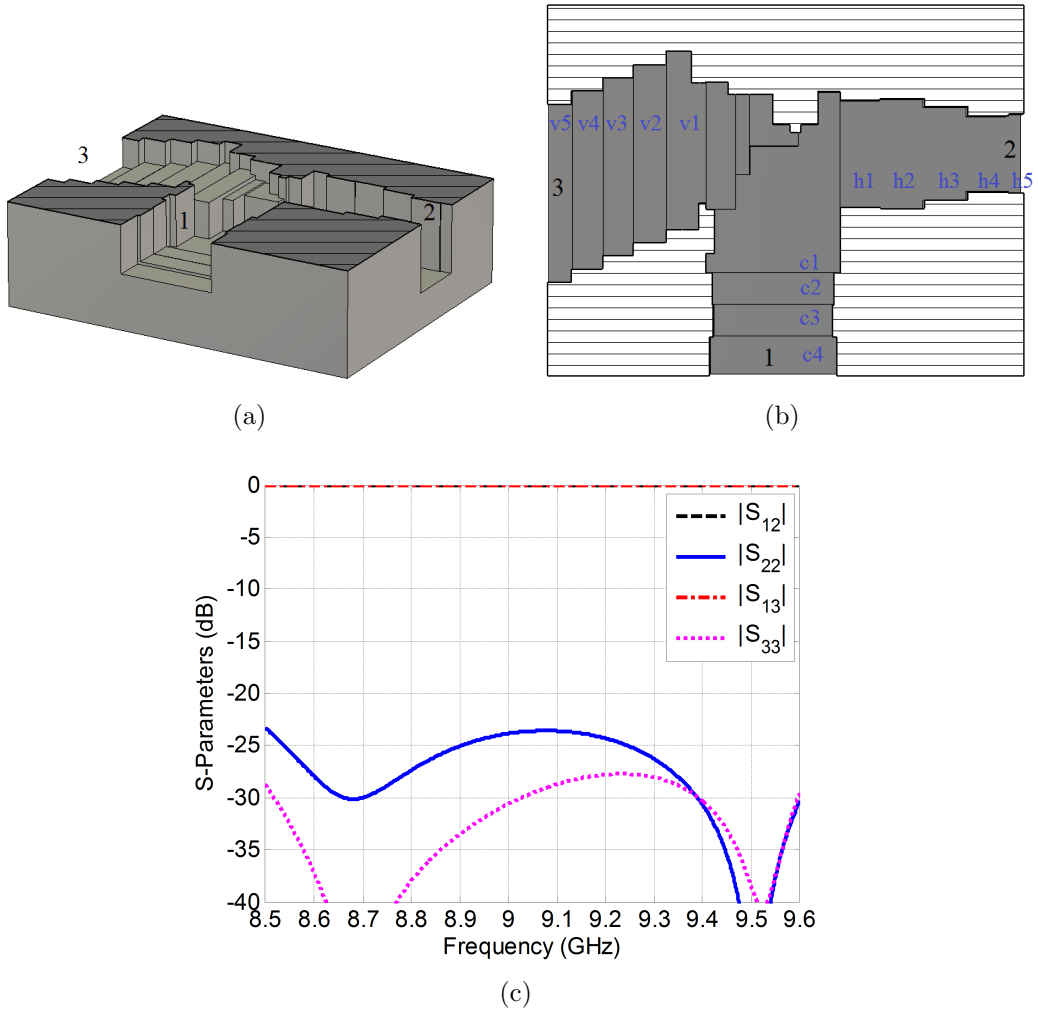


Figure 4.17: The proposed OMT with offset. (a) 3D horizontal sectional view. (b) Plane horizontal sectional view. (c) Simulation results.

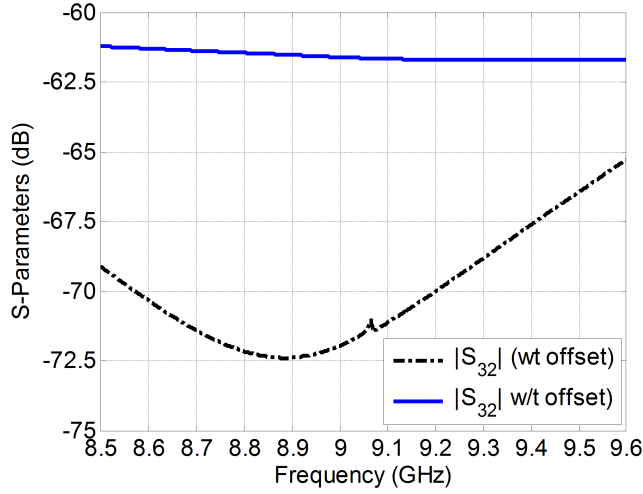


Figure 4.18: Comparison between the simulated isolation level of OMT with and without offset.

The selected offset value is  $0.2\lambda_0$  at the center frequency of the targeted band. The modified design after introducing the offset is shown in Fig. 4.17. The simulation results of both matching and transmission are shown in Fig. 4.17(c). The comparison between the isolation levels with and without the offset is shown in Fig. 4.18.

Table 4.3: Proposed OMT Dimensions.

Parameter	Dimension (mm)	Parameter	Dimension (mm)
$L_{h1}$	6.35	$b_{h1}$	17.02
$L_{h2}$	7.11	$b_{h2}$	17.53
$L_{h3}$	6.86	$b_{h3}$	15.24
$L_{h4}$	6.35	$b_{h4}$	12.19
$L_{h5}$	2.54	$b_{h5}$	12.62
$L_{v1}$	6.35	$b_{v1}$	9.14
$L_{v2}$	5.08	$b_{v2}$	9.14
$L_{v3}$	4.83	$b_{v3}$	10.16
$L_{v4}$	5.08	$b_{v4}$	10.41
$L_{v5}$	3.81	$b_{v5}$	12.62
$L_{c1}$	3.05	$a_{c1}$	21.59
$L_{c2}$	5.08	$a_{c2}$	19.3
$L_{c3}$	5.08	$a_{c3}$	19.05
$L_{c4}$	6.35	$a_{c4}$	20.32
$b_{c1}$	21.59	$b_{c3}$	19.05
$b_{c2}$	19.56	$b_{c4}$	20.32

The final dimensions of the impedance transformers after introducing the offset are shown in Table 4.3.

### 4.2.3 Validation and Experimental Results

The proposed OMT structure with an offset is validated experimentally by three different setups. The back-to-back setup by connecting two OMTs to each other without any rotation, the same setup with  $90^\circ$  rotation between the two OMTs, and finally measuring only one OMT that is connected to a non-standard matched load through the common port. The following subsections explain each setup and present the measurements compared to the simulated results. The proposed OMT is fabricated using a CNC machine that has a tolerance value of  $\pm 0.001''$ . The fabricated OMT and the back-to-back measurement setup are shown in Fig. 4.19

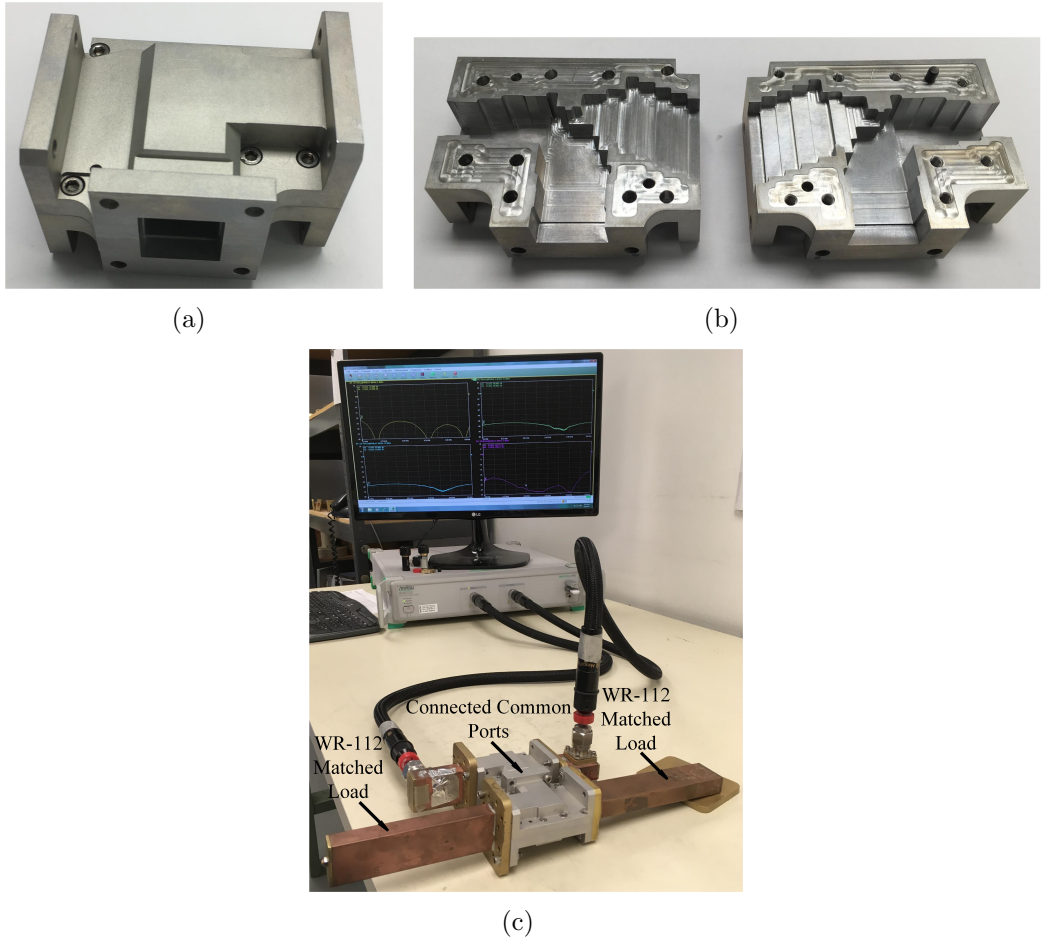


Figure 4.19: Fabricated OMT. (a) 3D view. (b) Sectional view. (c) Measurement setup of the back-to-back setup.

#### 4.2.3.1 Back-to-Back

This setup is simple and reliable since the measuring ports are four ports. The ports numbering in this setup are: Port 2 and 4 are for horizontal polarization while Port 3 and 5 are for vertical polarization. Moreover, the common ports (port 1 and port 6) are not existing since they are connected to each other. This setup is simulated and measured. Notice that the transmission and isolation between the ports of the opposite sides exchange as will be seen from the results later. The advantage of this method is providing information regarding the transmission coefficients of each polarization and the cross-polarization level that might be due to the OMT itself. It should also be stated that because the square cross-sectional waveguide is not a standard one and it is difficult to measure the transmission from Port 2 and 3 to Port 1 without having a transition from square to the rectangular waveguide to be connected to the common port. It can be seen that this method of using two similar OMTs back-to-back is providing the needed transitions from the common port to the two polarizations. The measurements are compared to the simulated results and shown in Fig. 4.20. There is a good agreement between the measurements and the simulations.

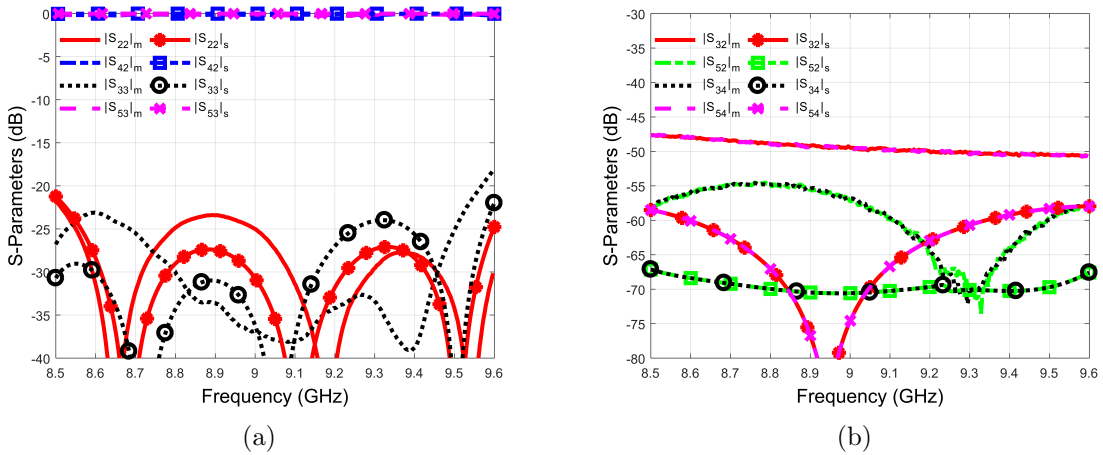


Figure 4.20: Simulated and measured S-parameters of the proposed OMT with an offset in back-to-back setup. (a) Reflection and transmission coefficients. (b) Isolation coefficients.

#### 4.2.3.2 Back-to-Back with 90°

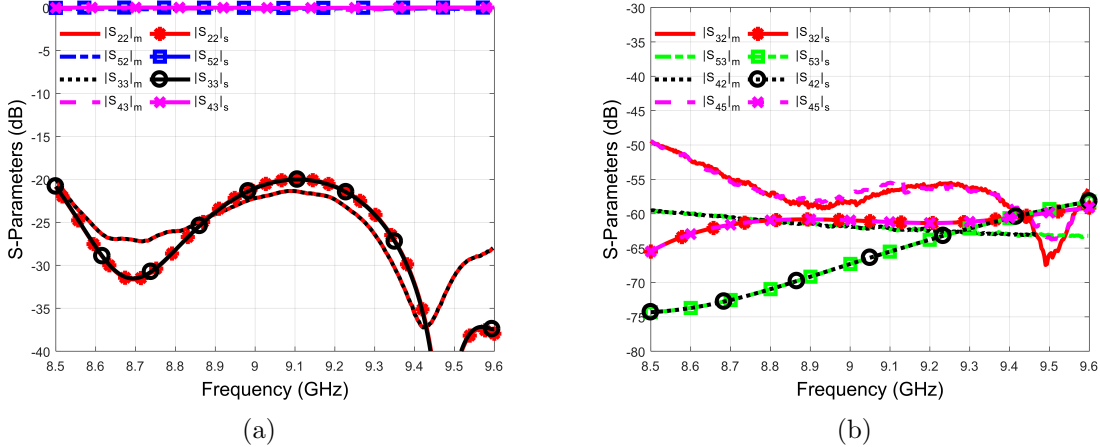


Figure 4.21: Simulated and measured S-parameters of the proposed OMT with an offset in a back-to-back setup with 90° rotation. (a) Reflection and transmission coefficients. (b) Isolation coefficients.

This setup is also simple and reliable as the previous one. The only difference is that one of the two OMTs is rotated by 90°. In this setup, the ports numbering are changed to be: Port 2 and 5 are for horizontal polarization while Port 3 and 4 are for vertical polarization. The advantage of this setup over the previous one is to indicate if unwanted modes are propagating. Such modes can exist in the previous setup and being canceled by the length of the common port. Moreover, this setup also shows the tolerance of the fabricated components. Good agreement between simulated and measured results are shown in Fig. 4.21.

#### 4.2.3.3 Non-standard Matched Load

This measurement setup is based on connecting the common port (port 1) of the proposed OMT to a matched load that has low reflections. If only standard components are available, the conventional method is to use a matched load that is mounted inside one of the standard rectangular waveguides. The matched load should be connected to the common port so that the two polarization signals are absorbed. Since the common port is a square waveguide and the load is a rectangular waveguide, a transition must be used. In this situation, the matched load and the transition will have two setups. The first one for the vertical polarization and the second for the horizontal polarization. A more convenient way is to design a matched load that has a square cross-section with the same side length as the common port. This matched load is not a standard one, but it is preferred because no transitions are needed.

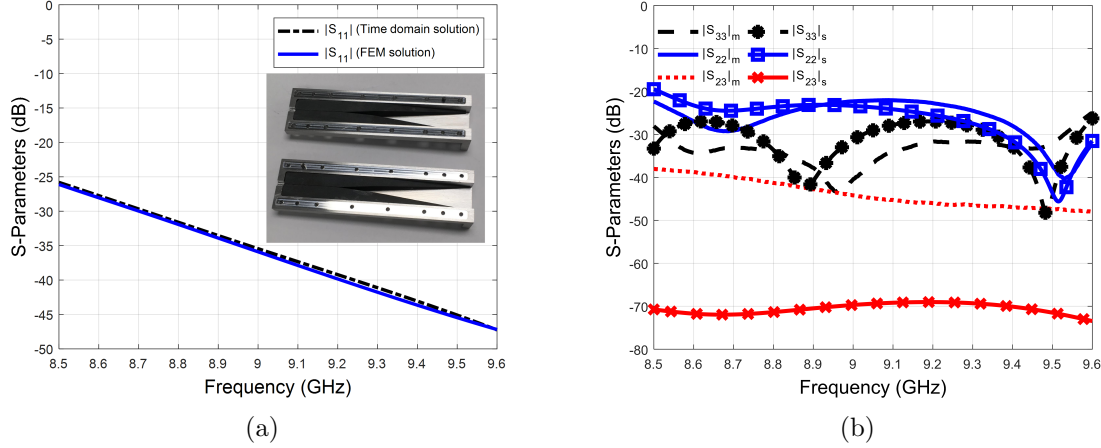


Figure 4.22: Designed matching load. (a) Sectional view of the fabricated prototype and its simulation results. (b) Connected to the OMT measured results (m) compared to simulation results (s).

However, no information regarding the actual transmission coefficients from Port 2 and 3 to Port 1 is possible since it is terminated with the matched load.

Since port 1 is terminated by a custom-made matched load, the S-parameters measured for both polarizations are the S-parameters of the single OMT. The matched load is designed to deploy four double tapered pyramids of Resin material (RS-4200CHP) that is a ceramic based with a dielectric constant of 12.6 and  $\tan \delta = 0.76$ . The prototype of the fabricated matched load and its simulated results are shown in Fig. 4.22(a). Comparison between the measured and simulated results based on this setup is shown in Fig. 4.22(b). The slight deviation between the simulated and measured results may occur due to the possible difference between the ideal simulated geometry and the fabricated geometry, which affect the actual machining level of the load since it consists of four pyramids that are supposed to be identical but challenging to achieve. In addition, the two fabricated OMTs may not be identical. Not to mention that each OMT prototype consists of two halves in which each of them is machined separately, and then connected to each other. All of these are factors that add up causing such deviations.

#### 4.2.4 Evaluation of Proposed OMT

A comparison between the proposed OMT and other published OMTs in terms of different specifications is presented. The published OMTs are classified into three classes depending on the structure symmetry, the first one is the two-folded symmetry, while the second is the one-folded symmetry and finally the asymmetric OMTs.

We start with the two-folded symmetry OMTs [66,89,90]. This design has many junctions including Y-junctions, E- or H-plane bends, and turnstile junction. These structures have improved the matching level compared to other classes. They have comparable isolation with the second class at the expense of size and complexity.

The second class of OMTs is the one-folded symmetry, many examples of such class have been published [91–93]. This class has almost half the complexity and the size of the first class. The main advantage of this structure is the freedom of adding shorting pins and matching sections that were a problem before for such class of OMTs. This design provides higher isolation at the expense of the size and complex structure that uses many junctions. Meanwhile, the proposed design has only one junction.

Table 4.4: Comparing the proposed OMT with different classes.

Type	Ref.	Advantages	Disadvantages
Two-folded	[66] [89] [90]	High isolation High matching level Large B.W	Considerable size Very complex structure Difficult ports align.
One-folded	[91] [94, 95] [92, 93]	High isolation Moderate matching level Large B.W	large size complex structure Difficult ports alignment
Asymmetric	[53, 64] [96–98] [74, 75]	Small size Simple structure Moderate matching level	Low isolation Small B.W Moderate ports alignment
Proposed OMT		Compact size Simple structure High isolation Easy ports alignment	Moderate matching level Small B.W

Table 4.5: Comparing the proposed OMT with asymmetric OMTs.

	Asymmetric OMTs	Proposed OMT
Overall Size ( $\lambda_0^3$ )	$> 2.5 \times 1.5 \times 2.5$	$1.7 \times 2.3 \times 0.86$
Isolation Level	Less than $-40\text{dB}$	$-65\text{dB}$
$-22.5\text{ dB BW}$	$4\% - 22\%$	$12.2\%$

The third class is the asymmetric OMT, which is featured with its compact size and simple structure among other OMT classes [53, 64, 96–98]. This class has a fair comparison with the proposed OMT as they both belong to the same class of asymmetry. The structure is simple but still needs some tuning stubs. This class achieves a comparable matching level with the present OMT. A comparison between the three classes is summarized in Table 4.4.

The asymmetric OMTs either have a T-junction in their core [53, 64, 96, 97] or a Y-junction instead of the T-junction [98, 99]. These OMTs deploy either circular or square waveguide common port. The presented alignment offset makes it different from the traditional asymmetric OMT. In addition, all ports share the same center plane cut, and both polarization ports are orthogonal with the common port. Although none of the polarization ports are in-line with the common port that usually used to achieve better matching, the presented OMT overcomes the matching and isolation problems without compromising the compact size. The proposed design is compact compared to most of the published OMTs. The proposed design has many advantages over the other published OMTs. These advantages are at the expense of a slight sacrifice of matching bandwidth. Nevertheless, the achieved matching level and bandwidth satisfies the SAR application requirements. The comparison between the asymmetric OMTs and the present OMT is shown in Table 4.5.

#### 4.2.5 Validation at 30 GHz Band

Due to the limited resources during the start of this work, the concept is practically validated at the x-band. Here, a scaled design at the Ka-band is provided. As the standard waveguides are not scalable, the scaled design has been tuned to work with the standard

Ka-band waveguide. In this section, the structure and the simulated results of the proposed OMT at the millimeter wave band are presented. Slight modifications have been made to the design to make it operational at the millimeter wave band, such as the two polarization ports are now WR-28 instead of WR-112. The internal dimensions of the fabricated structure are simply scaled to the 30 GHz band as shown in Fig. 4.23(b), but one step impedance transformer is added to each polarization port to improve the matching level. This validates that the proposed concept can be applied to any frequency band. The fabrication was done at a lower frequency band due to the machining limitations as mentioned before. The simulation results shown in Fig. 4.23(c) have the same behavior of the scaled fabricated one. The structure of such OMT is shown in Fig. 4.23(a).

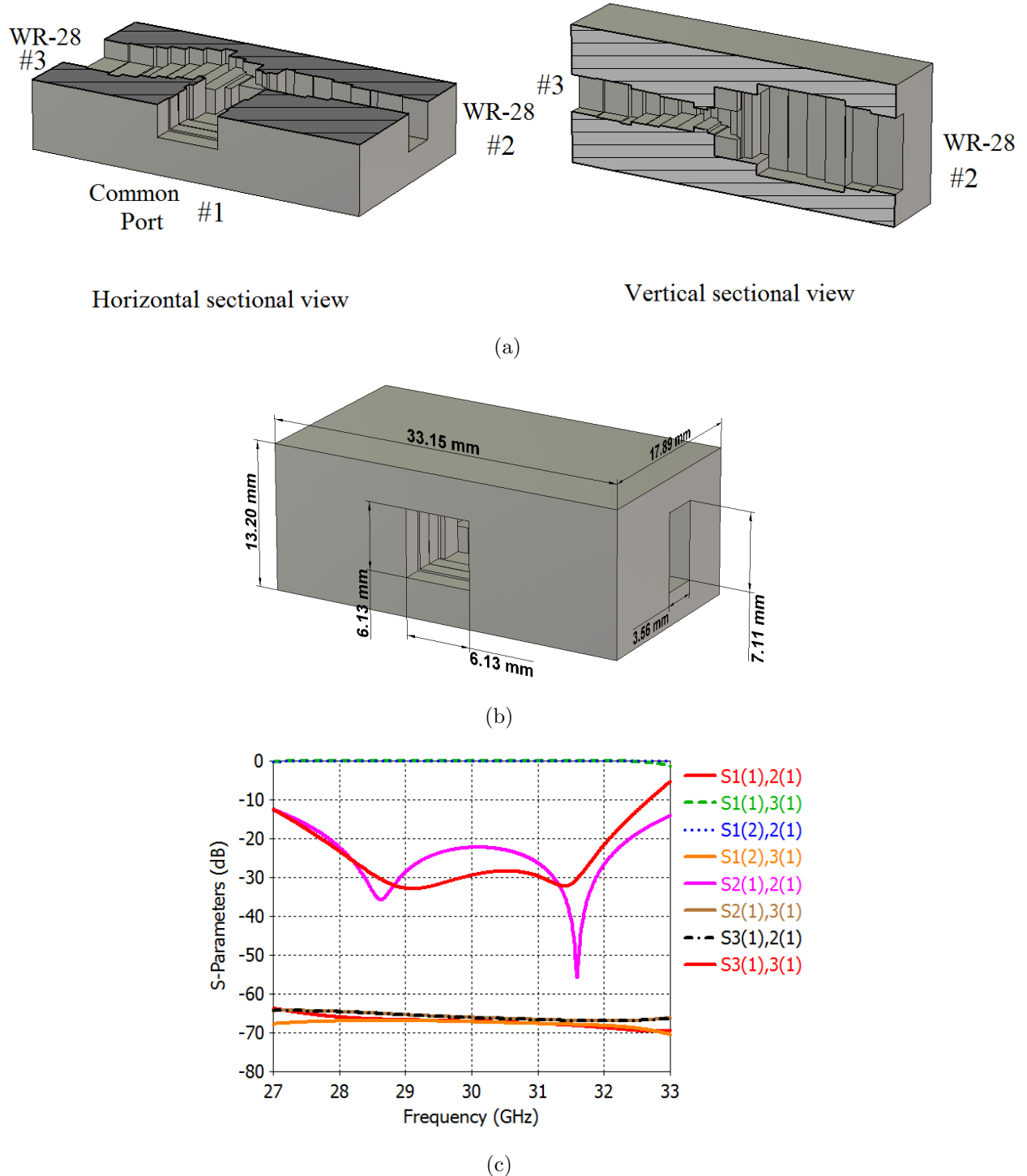


Figure 4.23: Presented OMT at 30 GHz band. (a) Structure 3D sectional views with port numbering. (b) Dimensions of the OMT structure. (c) Simulation results.

## 4.3 3D-Printed Wideband Groove Gap Waveguide Orthomode Transducer

This work presents a new design concept for the twofold symmetric OMT type by utilizing the groove gap waveguide technology. Such technology is selected due to its advantages over other technologies at Ka-band such as the broad bandwidth, absence of dielectric losses, and low radiation losses [22, 100, 101]. Moreover, it has an extra advantage over the ridge gap waveguide technology, which is the relatively high power capability [14, 100, 102–105]. In addition, such a design can allow having a feeding network for an array of such OMTs.

The fabrication technique used for this work is the 3D printing technology. There are few works discussing this technology for antennas and microwave devices [106–108]. The proposed structure consists of two main sections, the core, and the assembly elements. In Section 4.3.1, the OMT core is presented and investigated, and the guiding structure utilized in the isolated ports is discussed as well. Moreover, the proposed assembly elements and their simulation results are presented in Section 4.3.2. Later in Section 4.3.3, the simulated results of the overall OMT after connecting the assembly elements are studied and presented. Nevertheless, fabrication and measurements are presented in Section 4.3.5. Finally, this work is accepted for publication at [109] with more explanations and details.

### 4.3.1 Orthomode Transducer Core

This subsection presents the design of the central core of the proposed structure. The structure used in the isolated ports is the Groove Gap Waveguide (GGWG). It is selected due to its high-power capability compared to the ridge gap waveguide. The following subsection 4.3.1.1 discusses the proposed transmission line and its simulation results. Moreover, the OMT core design and its simulation results are presented in subsection 4.3.1.2.

#### 4.3.1.1 Proposed GGWG Transmission Line

The OMT designed in this work is symmetric. The selected guiding structure is GGWG in order to allow the structure to withstand a relatively higher power than the Ridge Gap Waveguide (RGW) structures. This guiding structure supports the  $TE_{10}$  mode of the rectangular waveguide even if the GGWG is not electrically connected. It is actually similar to the RGW with the ridge is removed to form the groove. In our case, the guide is excited by the output of the OMT core, which allows only one mode to propagate. This

means other modes are not banned from propagation because of the nature of the guiding structure, but because they are not excited at the input of the proposed guide.

The GGWG geometry, dimensions, and its simulated results are shown in Fig. 4.24. The simulated results in Figs. 4.24(c), and 4.24(d) show that the guide has an acceptable matching and transmission levels over the targeted band that is from 25 to 35 GHz.

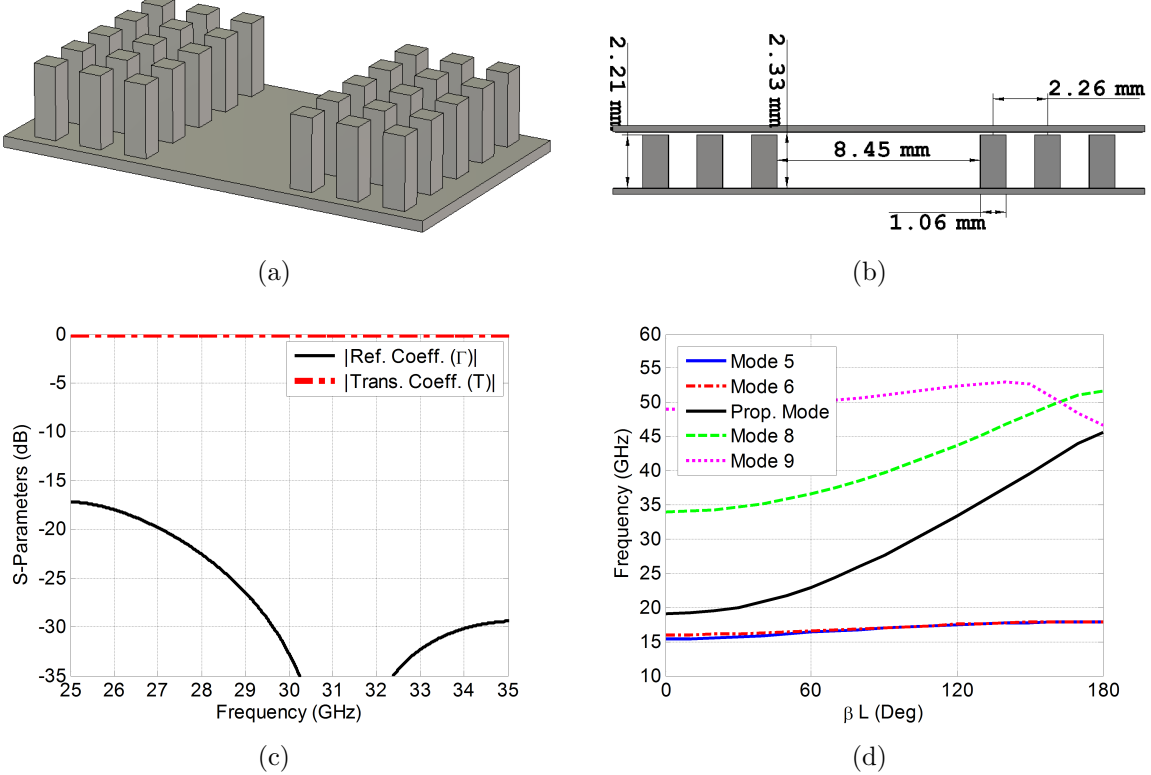


Figure 4.24: GGWG structure. (a) 3D view (Top conducting cover is hidden). (b) GGWG cross-section with the geometrical parameters. (c) Reflection and transmission coefficients. (d) Dispersion diagram.

#### 4.3.1.2 OMT Core Structure

The basic idea of the proposed OMT is summarized in the block diagram that is shown in Fig. 4.25. It is deploying the previously mentioned guiding structure at the polarization ports. Meanwhile, the common port (Port 1) is a nonstandard circular waveguide of diameter 0.32" (8.128 mm), it supports two propagating orthogonal polarizations of the  $TE_{11}$  mode. The selected diameter corresponds to  $TE_{11}$  at 21.6 GHz,  $TM_{01}$  at 28.3 GHz, which is an odd mode, and  $TE_{21}$  at 35.9 GHz. In other words, the available band is from 21.6 to 35.9 GHz. This allows the targeted frequency band (25 to 35 GHz) to propagate without any problem. A turnstile of the five sections is utilized to separate/combine the two orthogonal

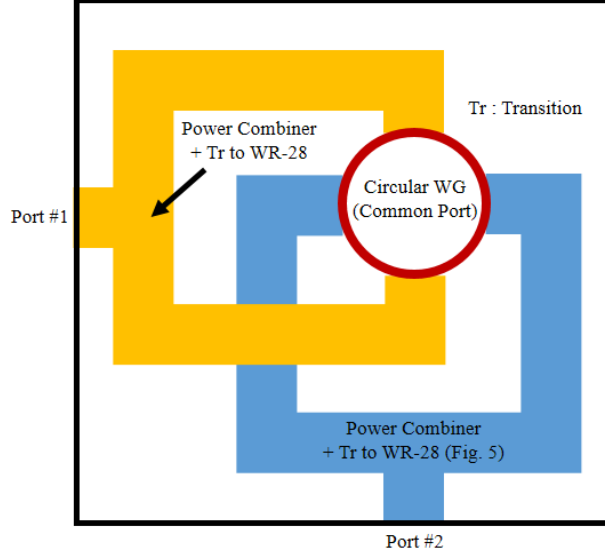


Figure 4.25: Block diagram of the proposed OMT.

polarizations. The turnstile divides each mode into two halves that are out of phase. For example, Port 3 and 5 support the same mode but with  $180^\circ$  phase difference. While Port 2 and 4 support the orthogonal modes with  $180^\circ$  phase difference. The core structure of the OMT is shown in Fig. 4.26, and its simulated results are shown in Fig. 4.27. The dimensions of the turnstile sections are shown in Table 4.6 where  $\phi_i$  and  $h_i$  are the diameter and the height, respectively. The sections are numbered starting from 1 to 5, which are corresponding to the base section and the top section, respectively.

### 4.3.2 Assembly Elements

This section discusses the assembly parts needed to combine each polarization signal after the separation process that is performed by the OMT core. The first part is the power combiner and the WR-28 transition while the second part is the transition between the two stacked GGWG layers. More explanations and details regarding these two elements are presented in the following two subsections.

#### 4.3.2.1 GGWG to WR-28 Power Combiner and Transition

The general idea of any power combiner is to combine two signals from two ports to one port. The two signals could be of any magnitude and phase. Here, the two signals are of the same magnitude, but out of phase. Thus, the power combiner must counteract the phase difference between the two signals. The idea of the proposed power combiner is based on a slot in the top ground of the GGWG, where two lines are feeding this slot from two opposite directions

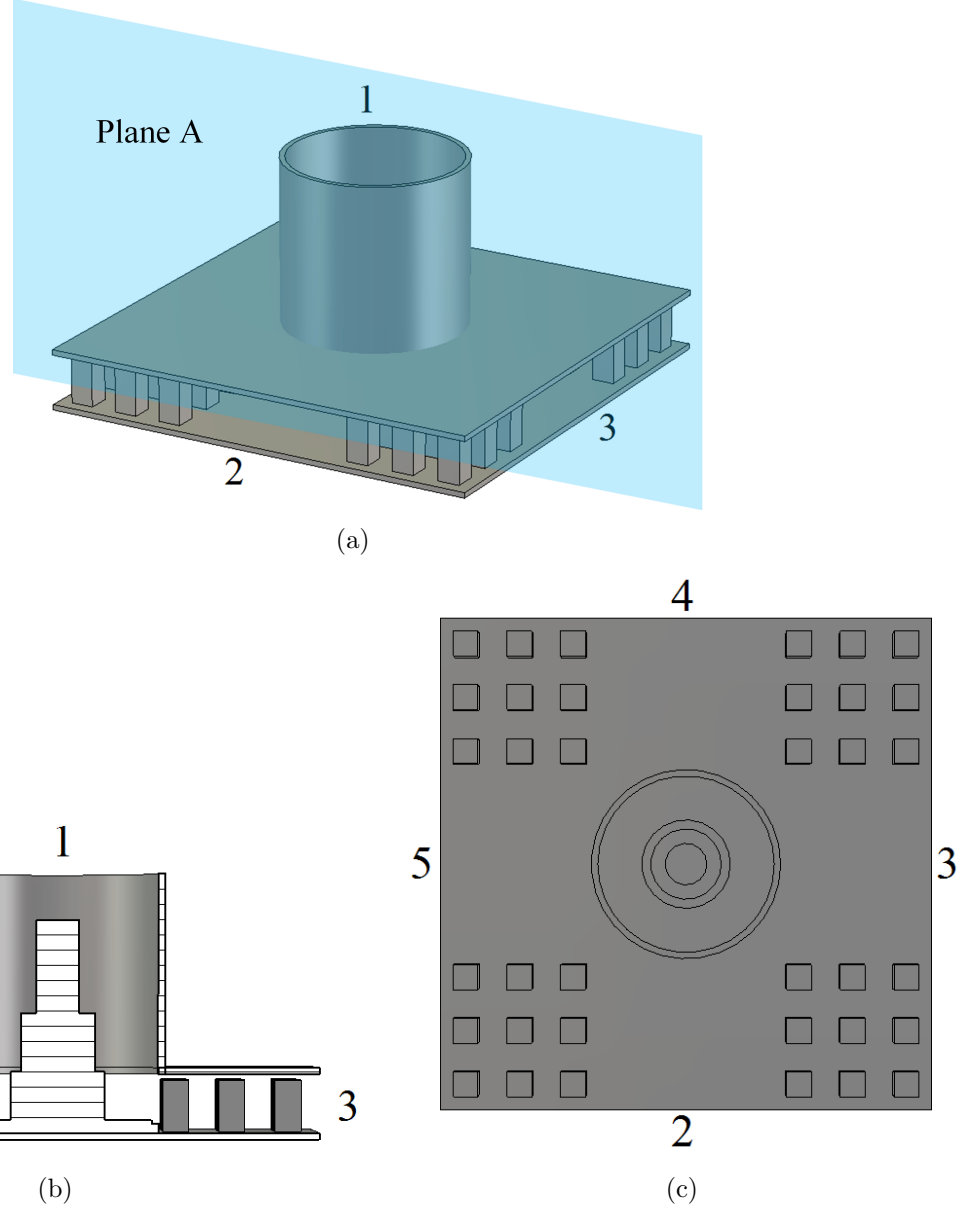


Fig. 4.26: Proposed OMT core, numbers are for ports. (a) 3D view. (b) Side cross-sectional view across Port 1, 3, and 5 on Plane A. (c) Planar view with top metallic cover and circular waveguide are removed.

as shown in Fig. 4.28. To improve the matching and reduce the reflections a turnstile of only one section (metallic cuboid) with rectangular cross-section is utilized. It is placed at the center of the slot. The dimensions of the slot are the same as the WR-28, which later facilitates the measurements of the fabricated prototype. The geometry and the structure of the proposed power combiner are shown in Figs 4.28(a), 4.28(b), and 4.28(c). Moreover, the simulation results are shown in Fig. 4.29. As shown in Fig. 4.29(a) the matching level is around 20 dB over the entire band, while in Fig. 4.29(b) the phase difference between the

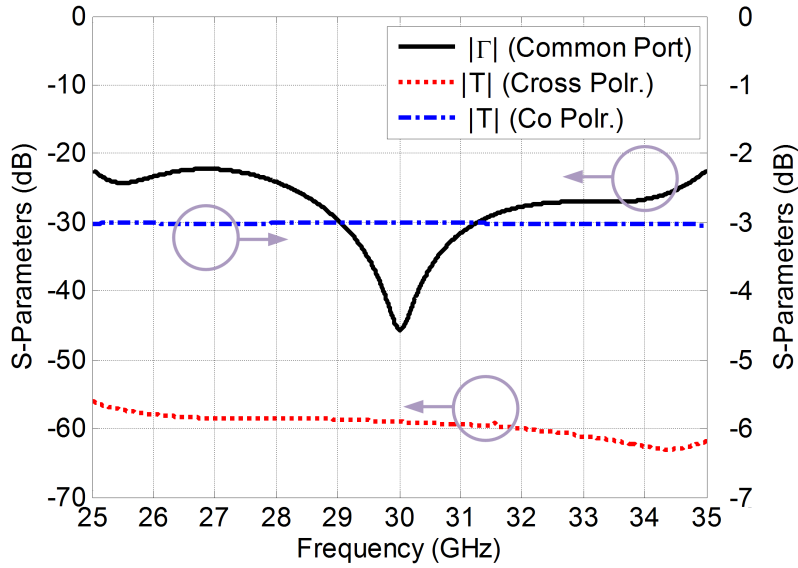


Figure 4.27: Simulated results of the proposed OMT core.

Table 4.6: Turnstile Dimensions.

Section $i$ Bottom to top	Section diameter $\phi_i$ (mm)	Section height $h_i$ (mm)
1	8.00	0.38
2	7.46	0.12
3	3.72	1.93
4	2.94	2.31
5	1.71	3.67

two feeding ports is  $180^\circ$ , which is required to compensate the other  $180^\circ$  occurred because of the turnstile. Moreover, to show that the two feeding ports are out of phase, the magnetic field distribution at 30 GHz is shown in Fig. 4.29(c). This power combiner is used twice within the OMT design. It is used in layer 1 for polarization 1 and then used in layer 2 for

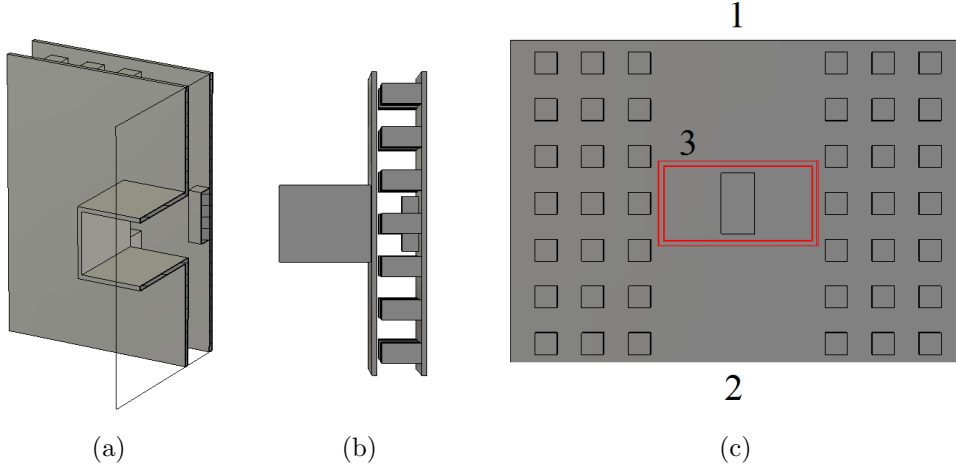


Figure 4.28: GGWG to WR-28 power combiner and transition with port numbers. (a) 3D view of half the structure. (b) Front view. (c) Planar view with the top removed and the red rectangle indicating the position of the rectangular waveguide.

the polarization 2.

#### 4.3.2.2 GGWG to GGWG Multilayer Transition

The proposed OMT consists of two GGWG layers to combine each polarization signal in a single layer. This provides high isolation between the two polarization signals and reduces the mismatch. Thus, a transition between the two layers must be introduced. The proposed transition is equivalent to  $360^\circ$  that is used with standard waveguides, but here we are utilizing the GGWG, which is more challenging to implement.

The transition consists of a slot with dimensions  $7.11 \times 3.56 \text{ mm}^2$ , which is placed in the common wall between the two layers of the GGWGs. The common wall is the top conducting cover of the lower GGWG and at the same time is the bottom conductor of the upper GGWG. In other words, the upper GGWG is organized in the same order as the lower one, and this is not a mirror version. A shorting wall is placed at such a slot; it is connecting the lower GGWG to the upper GGWG. Such wall has the same width of the slot and half its length. It is aligned to be entirely in the rear half of the slot. The geometry of this transition is shown in Fig. 4.30, and its simulation results are shown in Fig. 4.31. It is clear that the matching level of this transition is better than 20 dB.

#### 4.3.3 Overall OMT Structure

The final OMT structure is to be discussed in this subsection. The OMT core has four outputs, each two of them are for one polarization signal as mentioned before. The simulation

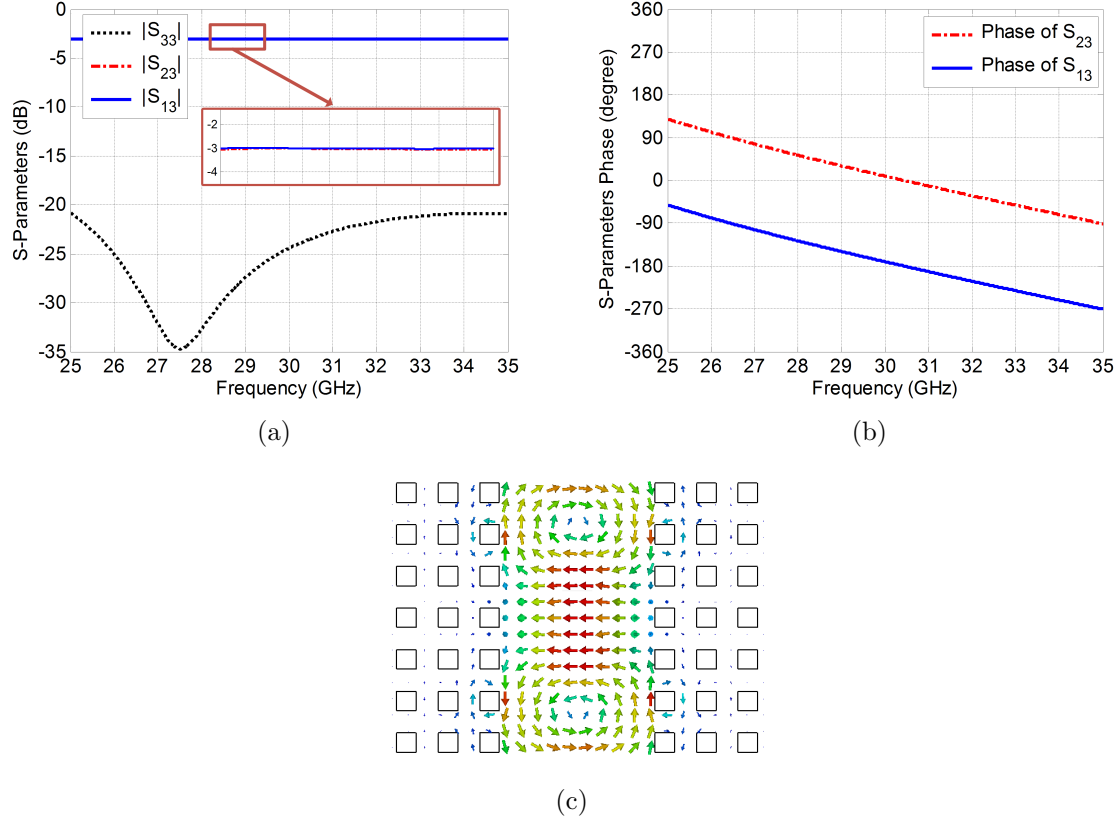
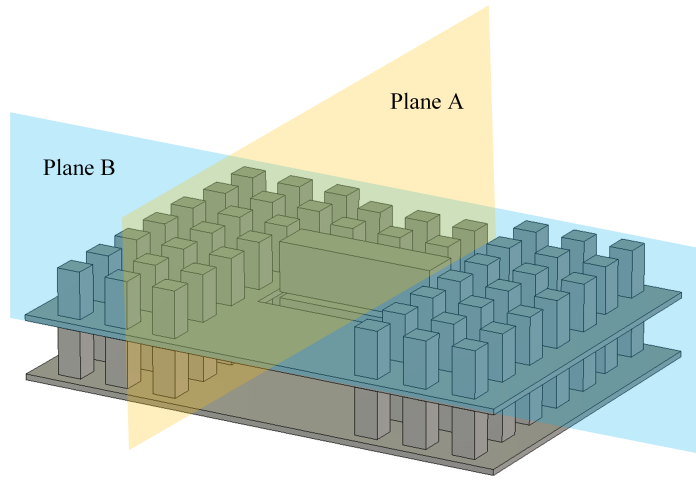


Figure 4.29: GGWG to WR-28 power combiner and transition simulation results. (a) Reflection and Transmission coefficients, indicating equal power division. (b) Phase indicating Port 1 and 2 are out of phase. (c) Magnetic field distribution at 30 GHz on the horizontal plane cut.

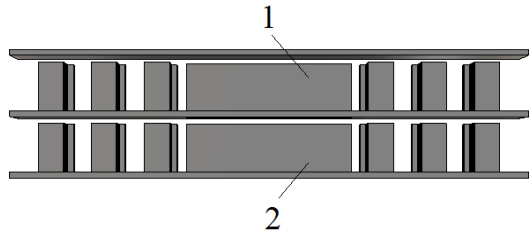
results of the whole OMT are shown in Fig. 4.32. It achieves a matching level better than 15 dB for the two polarization signals over 10 GHz from 25 to 35 GHz. The isolation between the two polarizations is better than 45 dB over the whole entire band. Nevertheless, the insertion loss has an acceptable level over such a band.

The fabricated OMT consists of three layers, the lower, the middle, and the top layer. The three layers are shown in Fig. 4.33. In the first layer, two of the outputs of the OMT core that are corresponding to one polarization signal is combined and transferred to WR-28 standard waveguide using the power combiner proposed in the previous section that is shown in Fig. 4.28. Meanwhile, the other two outputs are transferred to an upper layer by the transition that is described before and shown in Fig. 4.30. This layer is shown in Fig. 10(a).

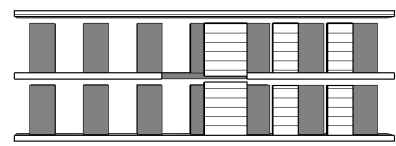
The second layer is responsible for the combining of the other polarization and transferring it to another WR-28 standard waveguide, again using the proposed power combiner that is shown in Fig. 4.28. This layer is shown in Fig. 10(b).



(a)



(b)



(c)

Figure 4.30: Transition between two stacked GGWG. (a) 3D view with the Top removed. (b) Cross-section on Plane B. (c) Cross-section on Plane A.

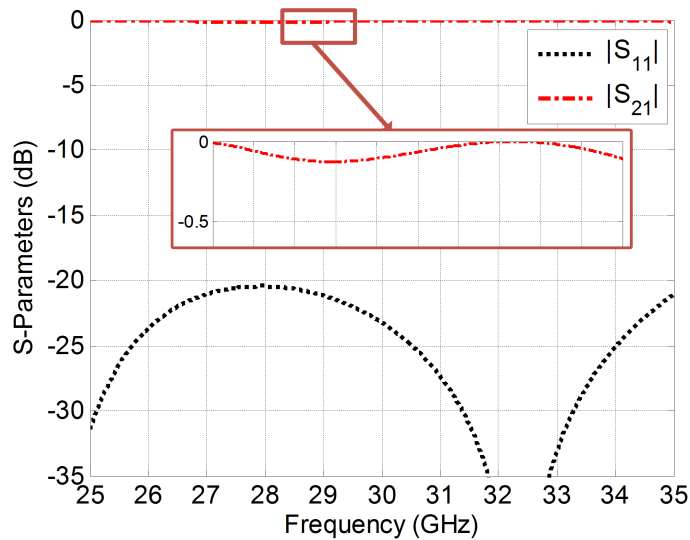


Figure 4.31: Transition between two GGWG layers simulation results (matching and insertion loss).

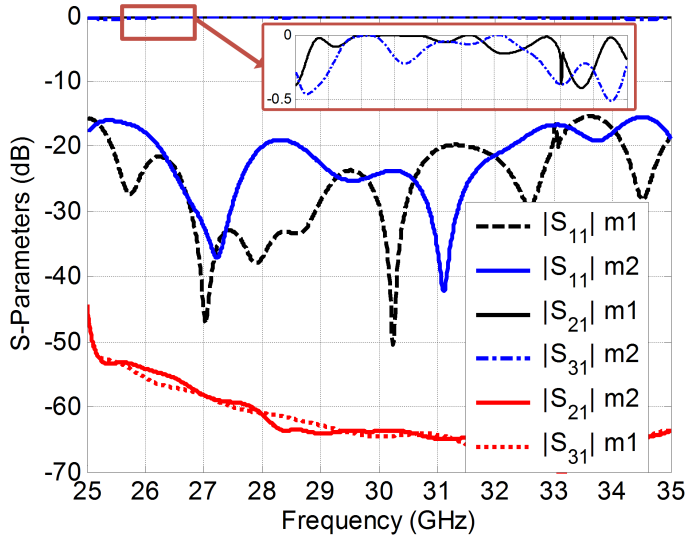


Figure 4.32: Simulation results of the overall OMT excited through the common port (m1 : mode 1, m2 : mode 2).

The top layer of the OMT has three physical ports, one of the two orthogonal propagating signals, and each of the other two ports is for an isolated polarization signal and such a layer is shown in Fig. 10(c).

The three layers are stacked together using plastic screws and nuts to secure their alignment as shown in Fig. 10(d). It is worth to mention that there is no need for any electrical contacts between the OMT layers, and this is why we used plastic screws and nuts instead of metallic ones. The overall dimensions of the whole OMT are  $96.5 \times 50.8 \times 4.9$  mm<sup>3</sup>. The height above the top metallic cover of the OMT of the circular waveguide is 5 mm; such waveguide contains the turnstile responsible for modes separation/combination.

#### 4.3.4 Evaluation of Proposed GGWG OMT

In this subsection, a comparison between the proposed GGWG OMT and some of the other published OMTs is summarized and presented in Table 4.7. The published OMTs are deploying the rectangular waveguide technology. Meanwhile, the presented OMT is implemented by the groove gap waveguide technology. The proposed OMT is compared with those OMTs since there is no any published GGWG OMTs, and they are not discussed yet by other researchers. The GGWG technology has many advantages over the rectangular waveguide, such as the absence of the leakage problem. In other words, the rectangular waveguides are constructed by assembling two halves that they must have complete electrical contact with each other with no gaps. On the other hand, the groove

Table 4.7: Proposed OMT evaluation and comparison.

Points of Comparison	Twofold symmetric OMTs Ref. ( [66, 89, 90] )	Proposed OMT ( This work )
Technology	Rectangular waveguide	Groove gap waveguide
Complexity	Very complex	Simple
Overall size	Very large	Moderate
Isolation Level	20 – 40 dB	45 dB
–15 dB BW	18.2% – 44.4%	33.3%

gap waveguides do not need any electrical contact since the signal cannot propagate between Artificial Magnetic Conductor (AMC), and Perfect Electrical Conductor (PEC) surfaces.

The structure of [66] is very complex, and it has a large size. They deployed four 180° E-bends, two power combiners, and two impedance transformers. In [89], the structure is more complex, but it has a smaller size. They used four E-bends and other four H-bends. Moreover, two impedance transformers and two 180° out-of-phase power combiners are utilized. Meanwhile, in [90], to reduce the number of such components they used a cross-over region and two transitions. Thus, the size of the OMT was reduced while the operating bandwidth was shrunk.

In summary, these three references represent the main concept of the turnstile (twofold symmetric) OMTs, each of them has a different realization by using different components. The presented OMT in this work is more compact, easier in fabrication, and less complex than them.

#### 4.3.5 Fabrication and Measurements

The proposed OMT is fabricated to validate its performance and to prove the proposed concept. The technology used for the fabrication is relatively new. Firstly, the structure is printed via 3D-printer that utilizes a poly-carbonate material that is different from commonly ABS plastic used in 3D-printers. The poly-carbonate material has some impurities that help in the electroplating process. Then, the printed structure is electroplated which results on a deposit of 0.05 mm thick copper material. The surface roughness is around 200-400  $\mu\text{in}$  Ra which is comparable to that of a casting [110]. This process is done for surfaces of all parts of the OMT. Later, layers are assembled together using plastic screws and nuts. They are plastic since there is no need for any electrical contact between the layers. The OMT layers before the assembly are shown in Fig. 4.33. Also, the assembled OMT is shown in the same figure.

The setup used for the measurements is the back-to-back setup in which two OMTs are connected to each other via the common port. Such a setup is selected for its simplicity and reliability. Measurements are taken twice. In the first measurement, the two OMTs are aligned imaging each other. The second setup is by rotating one OMT by 90° from the other. In these setups, there are four ports that are numbered as shown in Fig. 4.34. During the measurements, only two ports of the network analyzer are used. Meanwhile, two matched loads are connected to the other ports as shown in Fig. 4.35(a). The WR-28 calibration kit used for such measurements is shown in Fig. 4.35(b). However, the available band of the WR-28 is from 21.077 GHz to 42.154 GHz, the commercial band is from 26.5 GHz to 40 GHz, to leave a guard band between the first and the second cutoff frequencies. Our structure is operating from 25 GHz to 35 GHz, which is possible since the lower frequency of the OMT is higher than the WR-28 first cutoff frequency. Thus, the traditional calibration of the commercial band cannot be used. A user-defined calibration is done in which the operating band is the same as the OMT band to assure that the measurements are done in a proper way.

The measured and simulated results are compared. The agreement is acceptable. Such comparison is shown in Fig. 4.36. The reflection coefficient in the back-to-back setup is always higher than the single OMT since in such setup the two OMTs are connected to each other. As shown in Fig. 4.36(a), and Fig. 4.36(b) the measured matching levels are better than 12.5 dB over the entire band. Moreover, in Fig. 4.36(c) the measured isolation levels are lower than the simulated results, which is expected due to that the two OMTs are not ideally identical.

The insertion loss in both setups is around 1 dB, which is comparable with the CNC

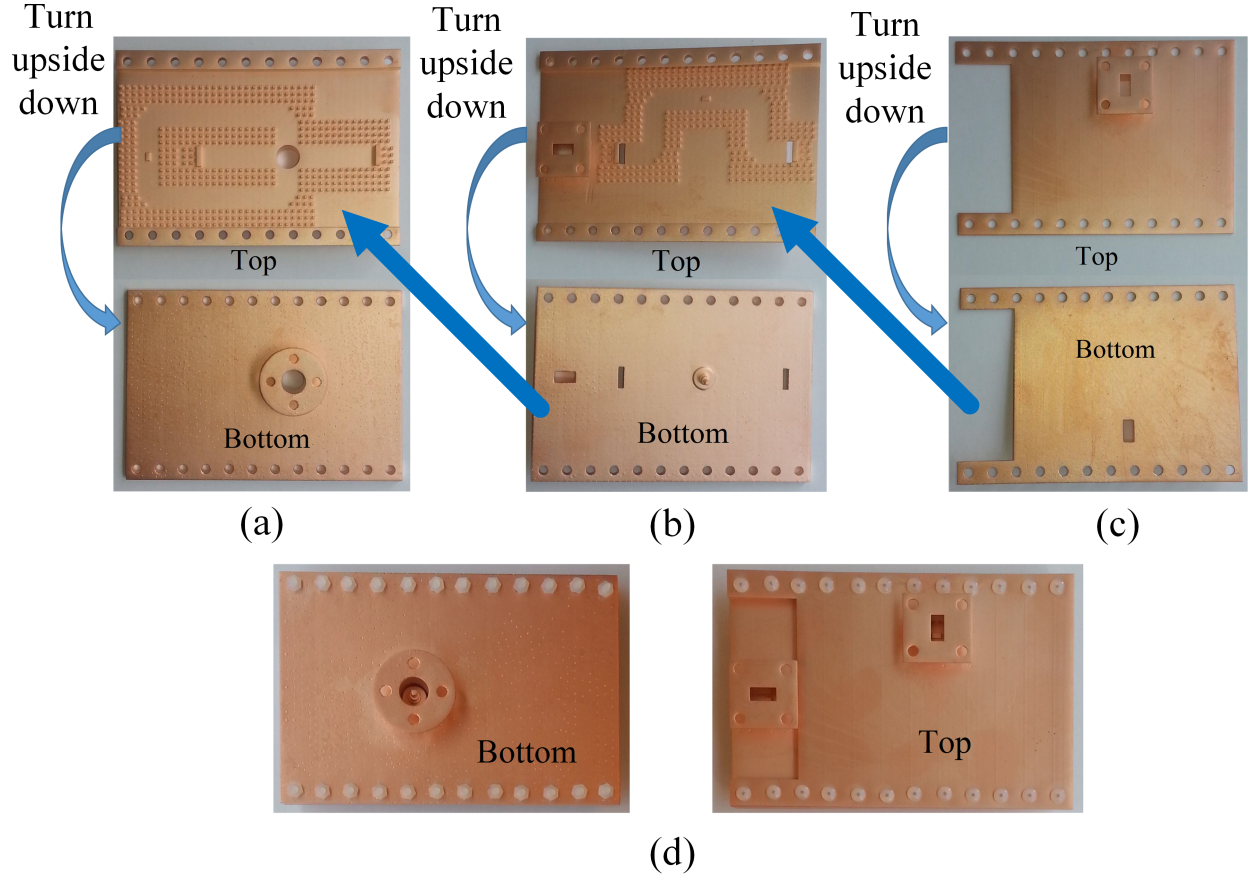


Figure 4.33: Photos of the Fabricated OMT different parts. (a) Lower part. (b) Middle part. (c) Top part. (d) Assembled OMT.

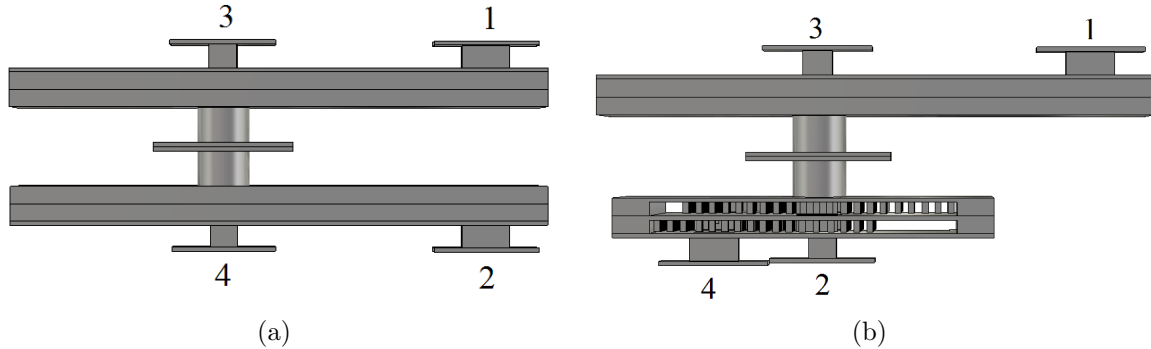


Figure 4.34: OMT back-to-back setup with port numbers. (a) Without rotation. (b) With  $90^\circ$  rotation angle.

machined structures. As mentioned before, the roughness is comparable with casting and CNC machined process [110]. The measured and simulated results represent the performance of two OMTs connected together with or without  $90^\circ$  rotation. Thus, the results of a single

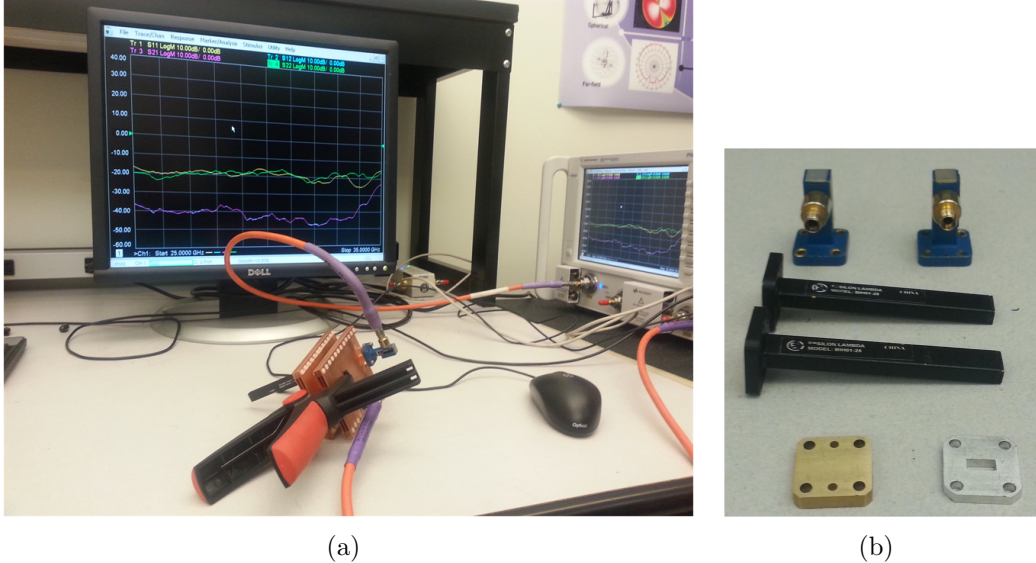


Figure 4.35: (a) OMT back-to-back measurements setup. (b) WR-28 calibration kit and transitions.

OMT are expected to be better than these results. In other words, matching, transmission, and isolation of a single OMT have better levels than the back-to-back setup. The back-to-back set up provide natural transition and separation of the two polarizations of the common mode. Therefore, it is simple, and reliable as explained before.

It is worth mentioning that the accuracy of the 3D-printer used in our fabrication is  $\pm 0.075$  mm in the X-Y plane (length and width), and  $\pm 0.15$  mm in the Z-direction (height). Such accuracy is not the best for the high frequencies. However, it is expected that the accuracy of these printers will improve in the near future due to the fast progress in this technology. The accuracy of the used printer affects the structure dimensions, which can reduce the OMT performance, and produce some ripples in the measurements. It may also increase the losses and increase the reflections. Since the structure is copper plated, the thin layer of copper can oxidize easily, which could reduce the OMT conductivity. Nevertheless, the 3D-printed and plated structures have many advantages compared to the machined devices, such as lighter weight and low fabrication cost.

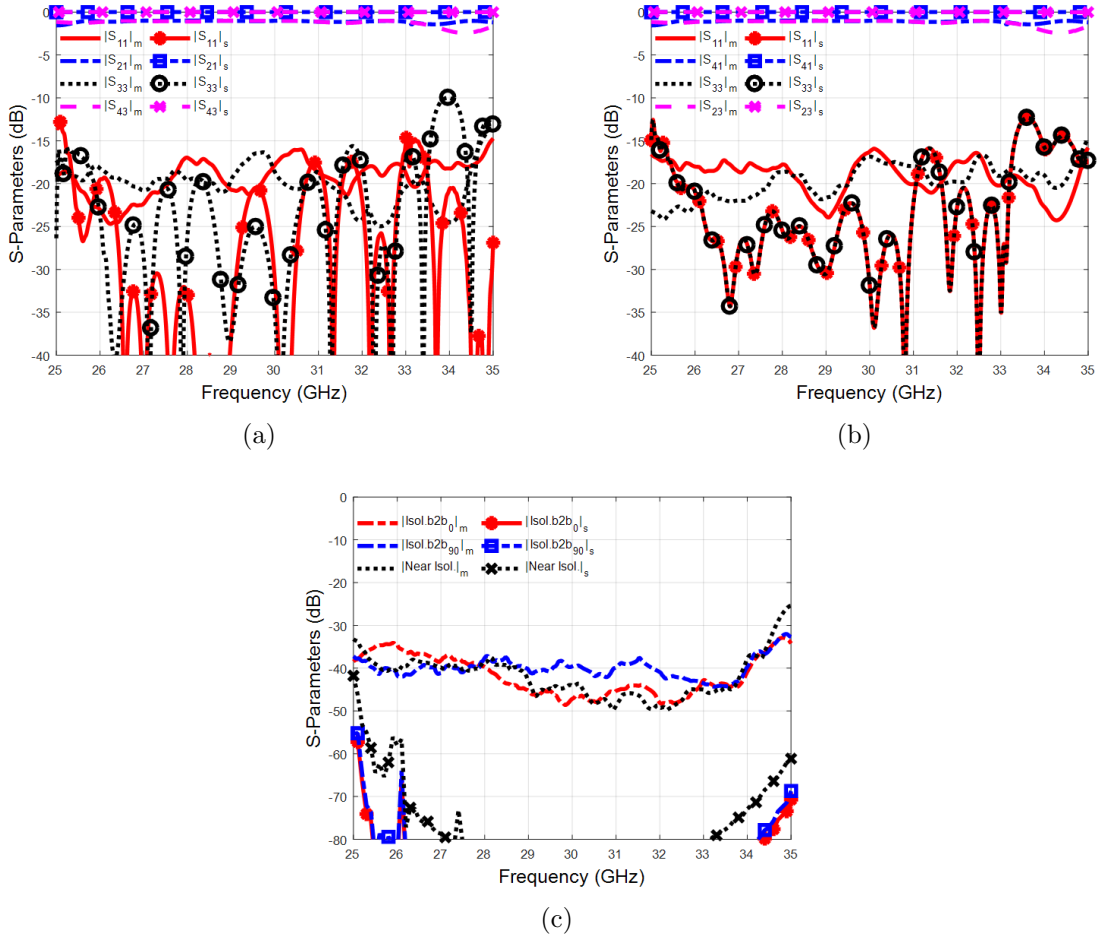


Figure 4.36: OMT simulation and measurement results using a back-to-back setup. (a) Without rotation (matching and insertion loss). (b) With 90° rotation angle (matching and insertion loss). (c) Isolation coefficient magnitudes.

# Chapter 5

## Conclusions and Future Work

### 5.1 Conclusions

The thesis has presented a consistent approach to design different devices for microwave and millimeter-wave applications. Two different types of microwave devices are proposed and presented. The first one is a non-reciprocal structure that supports only one propagating mode, while the second is a reciprocal device that has supported dual mode operation. All the simulated results without measurement verification have been verified by two commercial software (HFSS, which is based on frequency domain finite element method, and CST, which is based on time domain). The conclusions of the work presented in this thesis can be summarized in the following paragraphs.

A full study of the non-reciprocal ferrite based differential phased shifters has been presented showing the main criteria of the material selection and the traditional methodology for designing such shifters. Also, the limitations of this methodology are discussed. Moreover, a homogeneous solution with modeled equations to determine the differential phase occurring in such phase shifters has been proposed. Nevertheless, a novel inhomogeneous model with accurate equations is proposed for such shifters. Later, many cases are studied to validate the proposed modeled equations that have a very good agreement with simulations with a maximum error does not exceed 10%. In conclusion, an accurate model is proposed and validated to obtain the phase shift for the ferrite loaded rectangular waveguide. This structure is an essential building block in duplexers, which are deployed in all radar systems till now. Finally, an example has been selected for prototyping, and then the measured results are compared with the proposed model, the approximate relation, and the numerical simulation. The measurements of the differential phase shift, insertion loss, and matching have accepted values and levels that validate the proposed model.

A new RGW differential phase shifter configuration has been proposed. The presented configuration has a flat response and compact size. The introduced structure has been

designed for millimeter wave applications. It has an operating bandwidth of 5 GHz around the center frequency of 30 GHz. Nevertheless, the results have been validated by simulating the structure through two different numerical solvers; each has a different numerical method. Results extracted from both solvers have shown excellent agreement. The  $90^\circ$  extracted differential phase has a phase variation less than  $10^\circ$  over the entire operating bandwidth (27.5 GHz to 32.5 GHz).

A circularly polarized slot antenna based on the RGW technology has been presented. The antenna has deployed a compact RGW differential phase shifter, which is based on ferrite slabs. It has a matching bandwidth of 5 GHz around the center frequency, 30 GHz with a 3 dB axial ratio. The proposed structure has been validated by using two different computational methods, where both results have achieved an excellent agreement with each other.

An SIW phase shifter design has also been presented, with an ultra-flat response. The presented design is half the size of the corresponding rectangular waveguide phase shifter. The introduced configuration has been tested by designing phase shifter for Ku-band applications. Moreover, the results have been validated by using two different numerical techniques, where both solvers have an excellent agreement. The extracted differential phase between the output phases is centered at  $90^\circ$  with phase shift variation less than  $\pm 15^\circ$  over the entire operating bandwidth (12.4 GHz to 18 GHz). The proposed SIW phase shifter can be deployed in various applications such as isolators, duplexers, and feeding structures for circularly polarized antennas. One more important point that should be addressed is the excitation mechanism of the SIW phase shifter to support the full operating bandwidth with a proper matching level. In other words, the SIW is a low profile waveguide which needs the same excitation of the standard waveguides. Transitions from other types of connections such as the coaxial cable may affect the matching level and the phase variation of the SIW phase shifter.

A novel concept to design a compact OMT has been presented using a dual mode double ridge waveguide. The proposed concept has solved the in-band higher order mode excitation problem through a one-fold symmetric design. Use of one-fold symmetry concept has improved the OMT compactness and manufacturing simplicity by eliminating the need of pins, and irises that might be found in other symmetric OMT structures. The new OMT structure has been simulated, fabricated, and measured showing consistent agreement in a back-to-back configuration. Moreover, the design has achieved the full band measured matching level over 19 dB for the horizontal mode and over 26 dB for the vertical mode. The structure has shown a measured isolation level better than 30 dB. It is possible to increase the bandwidth of the new OMT configuration by utilizing a different common port

size that allows a broader bandwidth in addition to deploying more impedance transformers.

A novel compact asymmetric OMT configuration has been developed, which does not suffer from the matching problems as usually found with most of asymmetric OMTs. The isolation has been enhanced by introducing a slight deviation between the central axes of waveguides of each polarization. Moreover, the size is compact as compared to most published compact asymmetric OMTs. The fabricated prototype has been validated by using a back-to-back setup with and without the 90° rotation. Furthermore, the proposed design achieves matching and isolation level better than 22.5 dB and 60 dB, respectively, over the frequency band from 8.5 GHz to 9.6 GHz.

A novel twofold symmetry OMT has been designed based on the groove gap waveguide technology, which overcomes the problem of the electrical contact between the different fabricated parts of the structure at millimeter wave frequencies. The operating band is 25 GHz to 35 GHz. Two assembly elements have been deployed to combine each polarization. Moreover, the overall isolated ports have been considered to be WR-28 standard waveguide to facilitate the measurements. The OMT core, the assembly elements, and the WR-28 transition have achieved a matching level better than 20 dB over the whole band. The 3D-printing technology has been adapted for fabrication, which is low-cost and provides a lightweight structure. The structure has been plated with a 0.05 mm copper layer. A back-to-back setup measurement has been performed. The measured results have acceptable levels compared to the simulations considering available 3D-printing accuracy.

## 5.2 Main Contributions

Based on the completed tasks through, the contributions of the thesis can be outlined as follow.

### 5.2.1 Non-reciprocal Microwave Devices

The work is related to the non-reciprocal microwave devices can be listed as:

1. Investigating and providing an accurate mathematical model of the propagation constant inside a partially filled waveguide with ferrite slabs.
2. Utilizing the proposed model to design differential phase shifter using waveguide technology, and fabricating an example to test the proposed model.
3. Validating the differential phase shifter idea in the ridge gap waveguide technology.

4. Validating the same idea in with the Substrate Integrated Waveguide (SIW) technology.
5. Implementing the differential phase shifter to design a circularly polarized antenna.

### **5.2.2 Reciprocal Microwave Devices**

The work is related to the reciprocal microwave devices can be listed as:

1. Use of a dual mode of the unconventional double-ridge waveguide to design an improved one-fold symmetry OMT.
2. Introducing a high-performance asymmetric OMT that is compact by using E- and H-bend.
3. A new OMT based on groove gap waveguide technology is designed for the first time.  
In addition, it has a very wideband compared to other published OMTs.
4. Deploying the 3D-printing technology in the fabrication.

## **5.3 Suggested Future Work**

The 5G communication system still in the process of standardization and widening. More improvements are needed to the current microwave devices that serve the 5G. Thus, the new technologies such as the ridge gap waveguide and the groove gap waveguide are expected to play an important role in such a communication system. This is due to the high performance of such technologies at the high frequency bands. Moreover, their immunity to leakage problems and high losses. The future work suggested to continue this research work can be summarized through the following points:

1. Introducing the groove gap waveguide technology in the ferrite phase shifters.
2. Benefiting from ferrite material properties to improve the OMT performance.
3. Introducing compact asymmetric OMTs that are based on groove gap waveguide.
4. Introducing OMTs based on ridge gap waveguide.
5. Introducing low profile OMTs.

# Bibliography

- [1] K. R. Santhi, V. K. Srivastava, G. S. Kumaran, and A. Butare, “Goals of true broad band’s wireless next wave (4G-5G),” in *2003 IEEE 58th Vehicular Technology Conference. VTC 2003-Fall (IEEE Cat. No.03CH37484)*, vol. 4, Oct 2003, pp. 2317–2321 Vol.4.
- [2] T. Halonen, J. Romero, and J. Melero, *GSM, GPRS and EDGE performance: evolution towards 3G/UMTS*. John Wiley & Sons, 2004.
- [3] B. Furht and S. A. Ahson, *Long Term Evolution: 3GPP LTE radio and cellular technology*. CRC Press, 2016.
- [4] C. X. Wang, F. Haider, X. Gao, X. H. You, Y. Yang, D. Yuan, H. M. Aggoune, H. Haas, S. Fletcher, and E. Hepsaydir, “Cellular architecture and key technologies for 5G wireless communication networks,” *IEEE Communications Magazine*, vol. 52, no. 2, pp. 122–130, February 2014.
- [5] M. Fallgren, B. Timus *et al.*, “Scenarios, requirements and KPIs for 5G mobile and wireless system,” *METIS deliverable D*, vol. 1, p. 1, 2013.
- [6] T. K. Sarkar, M. C. Wicks, M. Salazar-Palma, and R. J. Bonneau, *Smart antennas*. John Wiley & Sons, 2005, vol. 170.
- [7] T. K. Sarkar, R. Mailloux, A. A. Oliner, M. Salazar-Palma, and D. L. Sengupta, *History of wireless*. John Wiley & Sons, 2006, vol. 177.
- [8] D. Pozar, *Microwave Engineering, 4th Edition*. Wiley, 2011.
- [9] “IEEE global history network, IEEE, 2013,” accessed: 2017-10-30.
- [10] M. Bozzi, L. Perregrini, K. Wu, and P. Arcioni, “Current and future research trends in substrate integrated waveguide technology,” *Radioengineering*, 2009.
- [11] O. Glubokov and D. Budimir, “Substrate integrated folded-waveguide cross-coupled filter with negative coupling structure,” in *2009 IEEE Antennas and Propagation Society International Symposium*, June 2009, pp. 1–4.

- [12] Z. C. Hao, W. Hong, J. X. Chen, H. X. Zhou, and K. Wu, “Single-layer substrate integrated waveguide directional couplers,” *IEE Proceedings - Microwaves, Antennas and Propagation*, vol. 153, no. 5, pp. 426–431, Oct 2006.
- [13] Y. J. Cheng, W. Hong, and K. Wu, “Design of a monopulse antenna using a dual V-type linearly tapered slot antenna (DVLTS),” *IEEE Transactions on Antennas and Propagation*, vol. 56, no. 9, pp. 2903–2909, Sept 2008.
- [14] P. S. Kildal, E. Alfonso, A. Valero-Nogueira, and E. Rajo-Iglesias, “Local metamaterial-based waveguides in gaps between parallel metal plates,” *IEEE Antennas and Wireless Propagation Letters*, vol. 8, pp. 84–87, 2009.
- [15] Y. Rahmat-Samii and H. Mosallaei, “Electromagnetic band-gap structures: classification, characterization, and applications,” in *2001 Eleventh International Conference on Antennas and Propagation, (IEE Conf. Publ. No. 480)*, vol. 2, 2001, pp. 560–564 vol.2.
- [16] P. S. Kildal, A. A. Kishk, and S. Maci, “Special issue on artificial magnetic conductors, soft/hard surfaces, and other complex surfaces,” *IEEE Transactions on Antennas and Propagation*, vol. 53, no. 1, pp. 2–7, Jan 2005.
- [17] P. S. Kildal, A. U. Zaman, E. Rajo-Iglesias, E. Alfonso, and A. Valero-Nogueira, “Design and experimental verification of ridge gap waveguide in bed of nails for parallel-plate mode suppression,” *IET Microwaves, Antennas Propagation*, vol. 5, no. 3, pp. 262–270, Feb 2011.
- [18] A. U. Zaman, E. Rajo-Iglesias, E. Alfonso, and P. S. Kildal, “Design of transition from coaxial line to ridge gap waveguide,” in *2009 IEEE Antennas and Propagation Society International Symposium*, June 2009, pp. 1–4.
- [19] P.-S. Kildal and A. Kishk, “EM modeling of surfaces with stop or go characteristics artificial magnetic conductors and soft and hard surfaces,” *Applied Computational Electromagnetics Society Journal*, vol. 18, no. 1, pp. 32–40, 2003.
- [20] A. U. Zaman, V. Vassilev, P. S. Kildal, and A. Kishk, “Increasing parallel plate stop-band in gap waveguides using inverted pyramid-shaped nails for slot array application above 60ghz,” in *Proceedings of the 5th European Conference on Antennas and Propagation (EUCAP)*, April 2011, pp. 2254–2257.

- [21] S. I. Shams and A. A. Kishk, “Double cone ultra wide band unit cell in ridge gap waveguides,” in *2014 IEEE Antennas and Propagation Society International Symposium (APSURSI)*, July 2014, pp. 1768–1769.
- [22] E. Rajo-Iglesias and P. S. Kildal, “Groove gap waveguide: A rectangular waveguide between contactless metal plates enabled by parallel-plate cut-off,” in *Proceedings of the Fourth European Conference on Antennas and Propagation*, April 2010, pp. 1–4.
- [23] M. Bosiljevac, A. Polemi, S. Maci, and Z. Sipus, “Analytic approach to the analysis of ridge and groove gap waveguides - comparison of two methods,” in *Proceedings of the 5th European Conference on Antennas and Propagation (EUCAP)*, April 2011, pp. 1886–1889.
- [24] E. Alfonso, M. Baquero, A. Valero-Nogueira, J. I. Herranz, and P. S. KildaL, “Power divider in ridge gap waveguide technology,” in *Proceedings of the Fourth European Conference on Antennas and Propagation*, April 2010, pp. 1–4.
- [25] H. J. Riblet, “The short-slot hybrid junction,” *Proceedings of the IRE*, vol. 40, no. 2, pp. 180–184, Feb 1952.
- [26] ——, “A mathematical theory of directional couplers,” *Proceedings of the IRE*, vol. 35, no. 11, pp. 1307–1313, Nov 1947.
- [27] R. Gupta, S. Anderson, and W. Getsingert, “Impedance transforming 3-dB 90 ° hybrids,” in *1987 IEEE MTT-S International Microwave Symposium Digest*, vol. 1, May 1987, pp. 203–206.
- [28] S. B. Cohn, “The re-entrant cross section and wide-band 3-dB hybrid couplers,” *IEEE Transactions on Microwave Theory and Techniques*, vol. 11, no. 4, pp. 254–258, Jul 1963.
- [29] B. Sheleg and B. E. Spielman, “Broadband (7–18 GHz) 10 dB overlay coupler for MIC application,” *Electronics Letters*, vol. 11, no. 8, pp. 175–176, April 1975.
- [30] E. Alfonso, M. Baquero, P. S. Kildal, A. Valero-Nogueira, E. Rajo-Iglesias, and J. I. Herranz, “Design of microwave circuits in ridge-gap waveguide technology,” in *2010 IEEE MTT-S International Microwave Symposium*, May 2010, pp. 1544–1547.
- [31] S. I. Shams, M. A. Abdelaal, and A. A. Kishk, “SIW Magic Tee fed by printed ridge gap waveguide design,” in *2016 17th International Symposium on Antenna Technology and Applied Electromagnetics (ANTEM)*, July 2016, pp. 1–2.

- [32] M. A. Abdelaal and A. A. Kishk, "Circularly polarized dielectric resonator antenna for UMTS and WLAN applications," in *2015 USNC-URSI Radio Science Meeting (Joint with AP-S Symposium)*, July 2015, pp. 335–335.
- [33] X. Hong, Y. Xia, B. Muneer, and Z. Qi, "Design of polarization-agile antenna by using integrated structure of phase shifter and power divider," in *2015 IEEE 4th Asia-Pacific Conference on Antennas and Propagation (APCAP)*, June 2015, pp. 523–524.
- [34] M. A. Abdelaal and A. A. Kishk, "Wideband circularly polarized dielectric resonator antenna for GPS and GNSS applications," in *2016 17th International Symposium on Antenna Technology and Applied Electromagnetics (ANTEM)*, July 2016, pp. 1–2.
- [35] J. Russat, J. P. Nicolai, P. Morvan, and N. Fel, "A delay line phase shifter for ultrawideband operation," in *1998 28th European Microwave Conference*, vol. 2, Oct 1998, pp. 669–672.
- [36] S. Lucyszyn and I. D. Robertson, "Decade bandwidth hybrid analogue phase shifter using MMIC reflection terminations," *Electronics Letters*, vol. 28, no. 11, pp. 1064–1065, May 1992.
- [37] S. J. Kim and N. H. Myung, "A new active phase shifter using a vector sum method," *IEEE Microwave and Guided Wave Letters*, vol. 10, no. 6, pp. 233–235, Jun 2000.
- [38] B. W. Min and G. M. Rebeiz, "Ka-band biCMOS 4-bit phase shifter with integrated LNA for phased array t/r modules," in *2007 IEEE/MTT-S International Microwave Symposium*, June 2007, pp. 479–482.
- [39] M. Meghdadi, M. Azizi, M. Kiani, A. Medi, and M. Atarodi, "A 6-bit CMOS phase shifter for s -band," *IEEE Transactions on Microwave Theory and Techniques*, vol. 58, no. 12, pp. 3519–3526, Dec 2010.
- [40] J. W. Simon, "Broadband strip-transmission line y-junction circulators," *IEEE Transactions on Microwave Theory and Techniques*, vol. 13, no. 3, pp. 335–345, May 1965.
- [41] F. Reggia and E. G. Spencer, "A new technique in ferrite phase shifting for beam scanning of microwave antennas," *Proceedings of the IRE*, vol. 45, no. 11, pp. 1510–1517, Nov 1957.
- [42] C. E. Fay and R. L. Comstock, "Operation of the ferrite junction circulator," *IEEE Transactions on Microwave Theory and Techniques*, vol. 13, no. 1, pp. 15–27, Jan 1965.

- [43] Y. Konishi and N. Hoshino, "Design of a new broad-band isolator," *IEEE Transactions on Microwave Theory and Techniques*, vol. 19, no. 3, pp. 260–269, Mar 1971.
- [44] F. A. Ghaffar and A. Shamim, "Theory and design of a half-mode SIW ferrite LTCC phase shifter," in *2015 IEEE MTT-S International Microwave Symposium*, May 2015, pp. 1–3.
- [45] C. E. Fay, "Ferrite-tuned resonant cavities," *Proceedings of the IRE*, vol. 44, no. 10, pp. 1446–1449, Oct 1956.
- [46] A. Clavin, "Reciprocal ferrite phase shifters in rectangular waveguide (correspondence)," *IRE Transactions on Microwave Theory and Techniques*, vol. 6, no. 3, pp. 334–334, July 1958.
- [47] A. Suntives, K. Payandehjoo, and R. Abhari, "Design and characterization of periodically-loaded substrate integrated waveguide phase shifters," in *2010 IEEE MTT-S International Microwave Symposium*, May 2010, pp. 1584–1587.
- [48] H. Peng, X. Xia, and T. Yang, "Slotted substrate integrated waveguide phase shifter," in *2016 IEEE Information Technology, Networking, Electronic and Automation Control Conference*, May 2016, pp. 1036–1039.
- [49] A. Benleulmi, N. Y. Sama, P. Ferrari, and F. Domingue, "Substrate integrated waveguide phase shifter for hydrogen sensing," *IEEE Microwave and Wireless Components Letters*, vol. 26, no. 9, pp. 744–746, Sept 2016.
- [50] S. H. V. Wambeck and A. H. Ross, "Performance of diversity receiving systems," *Proceedings of the IRE*, vol. 39, no. 3, pp. 256–264, March 1951.
- [51] R. D. Tompkins, "A broad-band dual-mode circular waveguide transducer," *IRE Transactions on Microwave Theory and Techniques*, vol. 4, no. 3, pp. 181–183, July 1956.
- [52] R. W. Jackson, "A planar orthomode transducer," *IEEE Microwave and Wireless Components Letters*, vol. 11, no. 12, pp. 483–485, Dec 2001.
- [53] J. M. Rebollar, J. Esteban, and J. D. Frutos, "A dual frequency OMT in the Ku-band for tt amp;c applications," in *IEEE Antennas and Propagation Society International Symposium. 1998 Digest. Antennas: Gateways to the Global Network. Held in conjunction with: USNC/URSI National Radio Science Meeting (Cat. No.98CH36)*, vol. 4, June 1998, pp. 2258–2261 vol.4.

- [54] S. J. Skinner and G. L. James, "Wide-band orthomode transducers," *IEEE Transactions on Microwave Theory and Techniques*, vol. 39, no. 2, pp. 294–300, Feb 1991.
- [55] J. Lahtinen, J. Pihlflyckt, I. Mononen, S. J. Tauriainen, M. Kemppinen, and M. T. Hallikainen, "Fully polarimetric microwave radiometer for remote sensing," *IEEE Transactions on Geoscience and Remote Sensing*, vol. 41, no. 8, pp. 1869–1878, Aug 2003.
- [56] G. L. James, "Wideband feed systems for radio telescopes," in *1992 IEEE MTT-S Microwave Symposium Digest*, June 1992, pp. 1361–1363 vol.3.
- [57] I. Dilworth, "A microwave receiver and transmitter system for a propagation experiment'," in *Proc. Radio receivers and associated systems*, 1981, pp. 319–323.
- [58] J. Brain, "The design and evaluation of a high performance 3m antenna for satellite communication," *Marconi Review*, vol. 41, pp. 218–236, 1978.
- [59] C. G. Montgomery, R. H. Dicke, and E. M. Purcell, *Principles of microwave circuits*. IET, 1948, no. 25.
- [60] A. M. Bøifot, E. Lier, and T. Schaug-Pettersen, "Simple and broadband orthomode transducer (antenna feed)," *IEE Proceedings H - Microwaves, Antennas and Propagation*, vol. 137, no. 6, pp. 396–400, Dec 1990.
- [61] M. Ludovico, B. Piovano, G. Bertin, G. Zarba, L. Accatino, and M. Mongiardo, "Cad and optimization of compact ortho-mode transducers," *IEEE Transactions on Microwave Theory and Techniques*, vol. 47, no. 12, pp. 2479–2486, Dec 1999.
- [62] P. Sarasa, A. Baussois, and P. Regnier, "A compact single-horn c/x dual band and circular polarized Tx Rx antenna system," in *IEEE Antennas and Propagation Society Symposium, 2004.*, vol. 3, June 2004, pp. 3039–3042 Vol.3.
- [63] J. A. Ruiz-Cruz, J. R. Montejo-Garai, and J. M. Rebollar, "Optimal configurations for integrated antenna feeders with linear dual-polarisation and multiple frequency bands," *IET Microwaves, Antennas Propagation*, vol. 5, no. 8, pp. 1016–1022, June 2011.
- [64] A. Dunning, S. Srikanth, and A. Kerr, "A simple orthomode transducer for centimeter to submillimeter wavelengths," in *Proc. Int. Symp. Space Terahertz Technol.*, 2009, pp. 191–194.

- [65] O. A. Peverini, R. Tascone, G. Virone, A. Olivieri, and R. Orta, “Orthomode transducer for millimeter-wave correlation receivers,” *IEEE Transactions on Microwave Theory and Techniques*, vol. 54, no. 5, pp. 2042–2049, May 2006.
- [66] A. Navarrini and R. L. Plambeck, “A turnstile junction waveguide orthomode transducer,” *IEEE Transactions on Microwave Theory and Techniques*, vol. 54, no. 1, pp. 272–277, Jan 2006.
- [67] G. Pisano, L. Pietranera, K. Isaak, L. Piccirillo, B. Johnson, B. Maffei, and S. Melhuish, “A broadband wr10 turnstile junction orthomode transducer,” *IEEE Microwave and Wireless Components Letters*, vol. 17, no. 4, pp. 286–288, April 2007.
- [68] J. L. Cano, A. Tribak, R. Hoyland, A. Mediavilla, and E. Artal, “Full band waveguide turnstile junction orthomode transducer with phase matched outputs,” *International Journal of RF and Microwave Computer-Aided Engineering*, vol. 20, no. 3, pp. 333–341, 2010.
- [69] A. Tribak, J. L. Cano, A. Mediavilla, and M. Boussouis, “Octave bandwidth compact turnstile-based orthomode transducer,” *IEEE Microwave and Wireless Components Letters*, vol. 20, no. 10, pp. 539–541, Oct 2010.
- [70] M. A. Meyer and H. B. Goldberg, “Applications of the turnstile junction,” *IRE Transactions on Microwave Theory and Techniques*, vol. 3, no. 6, pp. 40–45, December 1955.
- [71] J. Uher, J. Bornemann, and U. Rosenberg, *Waveguide components for antenna feed systems: Theory and CAD*. Artech House Publishers, 1993.
- [72] D. Henke and S. Claude, “Minimizing RF performance spikes in a cryogenic orthomode transducer (OMT),” *IEEE Transactions on Microwave Theory and Techniques*, vol. 62, no. 4, pp. 840–850, April 2014.
- [73] G. Chattopadhyay and J. E. Carlstrom, “Finline ortho-mode transducer for millimeter waves,” *IEEE Microwave and Guided Wave Letters*, vol. 9, no. 9, pp. 339–341, Sep 1999.
- [74] A. Dunning, “Double ridged orthogonal mode transducer for the 16–26 GHz microwave band,” in *Proceedings of the Workshop on the Applications of Radio Science*, 2002.
- [75] C. A. Leal-Sevillano, Y. Tian, M. J. Lancaster, J. A. Ruiz-Cruz, J. R. Montejos-Garai, and J. M. Rebollar, “A micromachined dual-band orthomode transducer,” *IEEE Transactions on Microwave Theory and Techniques*, vol. 62, no. 1, pp. 55–63, Jan 2014.

- [76] M. A. Abdelaal, S. I. Shams, M. A. Moharram, M. Elsaadany, and A. A. Kishk, “Rectangular waveguide differential phase shifter based on horizontal ferrite tiles: Accurate model for full-band operation,” *IEEE Access Journal*, (Accepted) 2018.
- [77] J. R. Bray and L. Roy, “Development of a millimeter-wave ferrite-filled antisymmetrically biased rectangular waveguide phase shifter embedded in low-temperature cofired ceramic,” *IEEE Transactions on Microwave Theory and Techniques*, vol. 52, no. 7, pp. 1732–1739, July 2004.
- [78] M. Kales, H. Chait, and N. Sakiotis, “A nonreciprocal microwave component,” *Journal of Applied Physics*, vol. 24, no. 6, pp. 816–817, 1953.
- [79] M. A. Abdelaal, S. I. Shams, and A. A. Kishk, “Compact RGW differential phase shifter for millimeter-wave applications,” in *2018 18th International Symposium on Antenna Technology and Applied Electromagnetics (ANTEM)*, Aug 2018, pp. 1–2.
- [80] ——, “90 ° phase shifter based on substrate integrated waveguide technology for Ku-band applications,” in *2017 XXXIIInd General Assembly and Scientific Symposium of the International Union of Radio Science (URSI GASS)*, Aug 2017, pp. 1–3.
- [81] Q. Wu, H. Wang, C. Yu, and W. Hong, “Low-profile circularly polarized cavity-backed antennas using siw techniques,” *IEEE Transactions on Antennas and Propagation*, vol. 64, no. 7, pp. 2832–2839, July 2016.
- [82] P. S. Hall and M. S. Smith, “Sequentially rotated arrays with reduced sidelobe levels,” *IEE Proceedings - Microwaves, Antennas and Propagation*, vol. 141, no. 4, pp. 321–325, Aug 1994.
- [83] S. I. Shams, M. A. Abdelaal, and A. A. Kishk, “Broadside uniform leaky-wave slot array fed by ridge gap splitted line,” in *2015 IEEE International Symposium on Antennas and Propagation USNC/URSI National Radio Science Meeting*, July 2015, pp. 2467–2468.
- [84] W. Tatinian and J. Lanteri, “Electronical beam scanning using integrated CMOS continuous 0° – 360° phase shifter,” in *2014 IEEE Conference on Antenna Measurements Applications (CAMA)*, Nov 2014, pp. 1–4.
- [85] M. A. Abdelaal and A. A. Kishk, “Dielectric resonator antenna gain improvement using electromagnetic band gap surface for radar applications,” in *2016 17th International Symposium on Antenna Technology and Applied Electromagnetics (ANTEM)*, July 2016, pp. 1–2.

- [86] M. A. Abdelaal, S. I. Shams, and A. A. Kishk, “Circularly polarized RGW slot antenna fed by ferrite based phase shifter,” in *2018 18th International Symposium on Antenna Technology and Applied Electromagnetics (ANTEM)*, Aug 2018, pp. 1–2.
- [87] M. A. Abdelaal, S. I. Shams, M. A. Moharram, M. Elsaadany, and A. A. Kishk, “Compact full band OMT based on dual-mode double-ridge waveguide,” *IEEE Transactions on Microwave Theory and Techniques*, vol. 66, no. 6, pp. 2767–2774, June 2018.
- [88] M. A. Abdelaal, S. I. Shams, and A. A. Kishk, “Asymmetric compact OMT for X-Band SAR applications,” *IEEE Transactions on Microwave Theory and Techniques*, vol. 66, no. 4, pp. 1856–1863, April 2018.
- [89] D. Dousset, S. Claude, and K. Wu, “A compact high-performance orthomode transducer for the atacama large millimeter array (ALMA) band 1 (31-45 GHz),” *IEEE Access*, vol. 1, pp. 480–487, 2013.
- [90] G. Engargiola and A. Navarrini, “K-band orthomode transducer with waveguide ports and balanced coaxial probes,” *IEEE Trans. Microw. Theory Techn.*, vol. 53, no. 5, pp. 1792–1801, May 2005.
- [91] A. Navarrini and R. Nesti, “Symmetric reverse-coupling waveguide orthomode transducer for the 3-mm band,” *IEEE Trans. Microw. Theory Techn.*, vol. 57, no. 1, pp. 80–88, Jan 2009.
- [92] G. Narayanan and N. Erickson, “Full-waveguide band orthomode transducer for the 3 mm and 1 mm bands,” in *Proceedings of the 14th International Symposium on Space Terahertz Technology*, 2003, pp. 508–512.
- [93] G. Narayanan and N. R. Erickson, “A novel full waveguide band orthomode transducer,” in *Proc. of the 13th International Space Terahertz Symposium, held at Harvard University*, vol. 94. Citeseer, 2002, p. 116.
- [94] S. Asayama and M. Kamikura, “Development of double-ridged waveguide orthomode transducer for the 2 mm band,” *Journal of Infrared, Millimeter, and Terahertz Waves*, vol. 30, no. 6, pp. 573–579, 2009.
- [95] N. Reyes, P. Zorzi, J. Pizarro, R. Finger, F. P. Mena, and L. Bronfman, “A dual ridge broadband orthomode transducer for the 7-mm band,” *Journal of Infrared, Millimeter, and Terahertz Waves*, vol. 33, no. 12, pp. 1203–1210, 2012.

- [96] N. Yoneda, M. Miyazaki, M. Tanaka, and H. Nakaguro, “Design of compact-size high isolation branching OMT by the mode-matching technique,” in *1996 26th European Microwave Conference*, vol. 2, Sep 1996, pp. 848–851.
- [97] U. Rosenberg and R. Beyer, “Compact T-junction orthomode transducer facilitates easy integration and low cost production,” in *2011 41st European Microwave Conference*, Oct 2011, pp. 663–666.
- [98] P. N. Choubey and W. Hong, “Novel wideband orthomode transducer for 70-95GHz,” in *2015 IEEE International Wireless Symposium (IWS 2015)*, Mar 2015, pp. 1–4.
- [99] Y. Li, “A simple waveguide omt designed for millimeter wave applications,” in *2016 IEEE International Conference on Microwave and Millimeter Wave Technology (ICMWT)*, vol. 2, June 2016, pp. 576–578.
- [100] A. Berenguer, V. Fusco, D. E. Zelenchuk, D. Snchez-Escuderos, M. Baquero-Escudero, and V. E. Boria-Esbert, “Propagation characteristics of groove gap waveguide below and above cutoff,” *IEEE Transactions on Microwave Theory and Techniques*, vol. 64, no. 1, pp. 27–36, Jan 2016.
- [101] M. Rezaee and A. U. Zaman, “Realisation of carved and iris groove gap waveguide filter and e-plane diplexer for v-band radio link application,” *IET Microwaves, Antennas Propagation*, vol. 11, no. 15, pp. 2109–2115, 2017.
- [102] P. Kildal, “Three metamaterial-based gap waveguides between parallel metal plates for mm/submm waves,” in *2009 3rd European Conference on Antennas and Propagation*, March 2009, pp. 28–32.
- [103] E. Rajo-Iglesias, M. Ferrando-Rocher, and A. U. Zaman, “Gap waveguide technology for millimeter-wave antenna systems,” *IEEE Communications Magazine*, vol. 56, no. 7, pp. 14–20, July 2018.
- [104] M. Ferrando-Rocher, J. I. Herranz-Herruzo, A. Valero-Nogueira, and A. Vila-Jimnez, “Single-layer circularly-polarized Ka-band antenna using gap waveguide technology,” *IEEE Transactions on Antennas and Propagation*, vol. 66, no. 8, pp. 3837–3845, Aug 2018.
- [105] A. Tamayo-Dominguez, J. Fernandez-Gonzalez, and M. S. Castaner, “Low-cost millimeter-wave antenna with simultaneous sum and difference patterns for 5G point-to-point communications,” *IEEE Communications Magazine*, vol. 56, no. 7, pp. 28–34, July 2018.

- [106] R. Sorrentino and O. A. Peverini, “Additive manufacturing: a key enabling technology for next-generation microwave and millimeter-wave systems [point of view],” *Proceedings of the IEEE*, vol. 104, no. 7, pp. 1362–1366, July 2016.
- [107] J. S. Silva, M. Garcia-Vigueras, T. Debogovic, J. R. Costa, C. A. Fernandes, and J. R. Mosig, “Stereolithography-based antennas for satellite communications in Ka-band,” *Proceedings of the IEEE*, vol. 105, no. 4, pp. 655–667, April 2017.
- [108] A. Tamayo-Dominguez, J. Fernandez-Gonzalez, and M. Sierra-Perez, “Groove gap waveguide in 3-D printed technology for low loss, weight, and cost distribution networks,” *IEEE Transactions on Microwave Theory and Techniques*, vol. 65, no. 11, pp. 4138–4147, Nov 2017.
- [109] M. A. Abdelaal and A. A. Kishk, “Ka-band 3D-printed wideband groove gap waveguide orthomode transducer,” *IEEE Transactions on Microwave Theory and Techniques*, (Accepted) 2018.
- [110] “Protolabs,” <https://www protolabs com/resources/white-papers/rapid-manufacturing-for-metal-prototypes-and-production-parts/>, accessed: 2018-10-15.
- [111] M. F. Farooqui, A. Nafe, and A. Shamim, “Inkjet printed ferrite-filled rectangular waveguide X-band isolator,” in *2014 IEEE MTT-S International Microwave Symposium (IMS2014)*, June 2014, pp. 1–4.
- [112] J. Helszajn, *Ridge waveguides and passive microwave components*. IET, 2000, no. 49.
- [113] S. B. Cohn, “Properties of ridge waveguide,” *Proceedings of the IRE*, vol. 35, no. 8, pp. 783–788, Aug 1947.
- [114] J. R. Whinnery and H. W. Jamieson, “Equivalent circuits for discontinuities in transmission lines,” *Proceedings of the IRE*, vol. 32, no. 2, pp. 98–114, Feb 1944.

# List of Publications

1. **M. A. Abdelaal**, and A. A. Kishk, “Ka-band 3D-Printed Wideband Groove Gap Waveguide Orthomode Transducer,” *Transactions on Microwave Theory and Techniques*, 2018. (Accepted)
2. **M. A. Abdelaal**, S. I. Shams, and A. A. Kishk, “Rectangular Waveguide Differential Phase Shifter Based on Horizontal Ferrite Tiles: Accurate Model for Full-band Operation,” *IEEE Access Journal*, 2018. (Accepted)
3. **M. A. Abdelaal**, S. I. Shams, M. A. Moharram, M. Elsaadany, and A. A. Kishk, “Compact Full band Based on Dual Mode Double Ridge Waveguide,” *Transactions on Microwave Theory and Techniques*, vol. 66, no. 6, pp. 2767-2774, June 2018.
4. **M. A. Abdelaal**, S. I. Shams, and A. A. Kishk, “Asymmetric Compact OMT for X-Band SAR Applications,” *Transactions on Microwave Theory and Techniques*, vol. 66, no. 4, pp. 1856-1863, April 2018.
5. **M. A. Abdelaal**, S. I. Shams, and A. A. Kishk, “Compact RGW Differential Phase Shifter for Millimeter-Wave Applications,” *2018 18th International Symposium on Antenna Technology and Applied Electromagnetics (ANTEM)*, Waterloo, ON, pp. 1-2, Aug 2018.
6. **M. A. Abdelaal**, S. I. Shams, and A. A. Kishk, “Circularly Polarized RGW Slot Antenna Fed by Ferrite Based Phase Shifter,” *2018 18th International Symposium on Antenna Technology and Applied Electromagnetics (ANTEM)*, Waterloo, ON, pp. 1-2, Aug 2018.
7. **M. A. Abdelaal**, S. I. Shams, and A. A. Kishk, “90° Phase Shifter Based on Substrate Integrated Waveguide Technology for Ku-band Applications,” *32 URSI General Assembly and Scientific Symposium*, pp. 1-3, Aug 2017.
8. **M. A. Abdelaal**, and A. A. Kishk, “Dielectric resonator antenna gain improvement using electromagnetic bandgap surface for radar applications,” *2016 17th International Symposium on Antenna Technology and Applied Electromagnetics (ANTEM)*, Montreal, QC, pp. 1-2, July 2016.

9. S. I. Shams, **M. A. Abdelaal**, and A. A. Kishk, "SIW Magic Tee fed by printed Ridge Gap Waveguide design," *2016 17th International Symposium on Antenna Technology and Applied Electromagnetics (ANTEM)*, Montreal, QC, pp. 1-2, July 2016.
10. **M. A. Abdelaal**, and A. A. Kishk, "Wideband circularly polarized dielectric resonator antenna for GPS and GNSS applications," *2016 17th International Symposium on Antenna Technology and Applied Electromagnetics (ANTEM)*, Montreal, QC, pp. 1-2, July 2016.
11. **M. A. Abdelaal**, and A. A. Kishk, "Circularly polarized dielectric resonator antenna for UMTS and WLAN applications," *2015 USNC-URSI Radio Science Meeting (Joint with AP-S Symposium)*, Vancouver, BC, Canada, pp. 335-335, July 2015.
12. S. I. Shams, **M. A. Abdelaal**, and A. A. Kishk, "Broadside uniform leaky-wave slot array fed by ridge gap splitted line," *2015 IEEE International Symposium on Antennas and Propagation & USNC/URSI National Radio Science Meeting*, Vancouver, BC, pp. 2467-2468, July 2015.

# Appendices

# Appendix A

## Ferrite Material Selection Criteria

Designing differential phase shifters based on ferrite materials need many considerations to assure that the selected ferrite material will perform the required operation. The selection of such materials depends mainly on basic parameters such as the saturation magnetization factor ( $4\pi M_s$ ), magnetic DC bias ( $H_0$ ), Larmor frequency ( $f_0$ ), and the saturated magnetic frequency ( $f_m$ ). These parameters are related to each other, and these relations are shown in the following equations [8].

$$f_0(\text{MHz}) = 2.8 \times H_0(\text{Oe}) \quad (\text{A.1})$$

$$f_m(\text{MHz}) = 2.8 \times 4\pi M_s(\text{G}) \quad (\text{A.2})$$

The criteria for selecting ferrite material must consider the following notes:

- The ferrite must be at least saturated. However, it is always recommended to operate above saturation. This ensures that some slight deterioration of the magnets will not lead to losing the saturation of the ferrite.
- The operating frequency band of the differential phase shifter must be outside the resonance frequency band of the ferrite; this means the prohibited band is between  $\sqrt{f_0 \times (f_0 + f_m)}$  and  $f_0 + f_m$  [111].
- The operating band can be above resonance (i.e.  $< \sqrt{f_0 \times (f_0 + f_m)}$ ) or below resonance (i.e.  $> f_0 + f_m$ ).
- In the below resonance band as the frequency increases the differential phase decreases till it reaches almost zero at very high frequencies. This means in order to have a reasonable phase shift the upper frequency of the operating band of the differential phase shifter must be at least around  $1.1 \times (f_0 + f_m)$  or slightly higher.

An example of the phase constant versus frequency in the ferrite medium case is illustrated in Fig. A.1. The phase constant  $\beta$  inside the ferrite material can be defined by the following

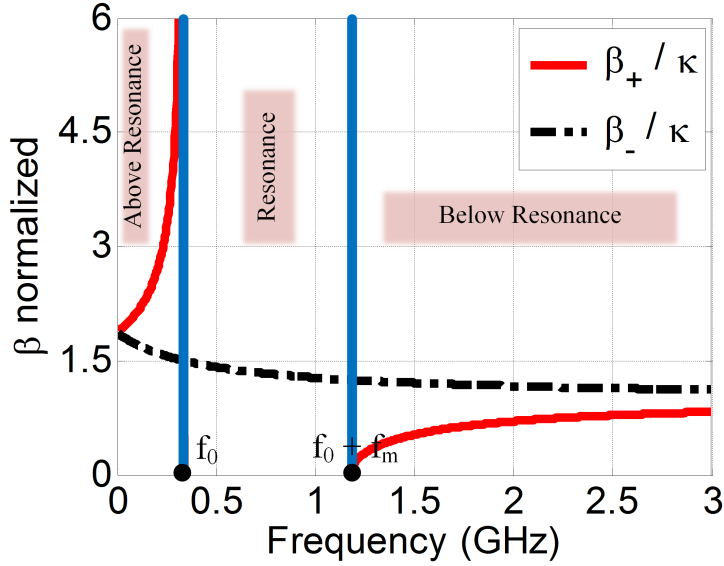


Figure A.1: Normalized phase constant vs. frequency of ferrite sample ( $4\pi M_s = 300$  G, and  $H_0 = 120$  Oe).

equation:

$$\beta_{\pm}/\kappa = \omega \sqrt{(\mu \pm \kappa)/\mu_0} \quad (\text{A.3})$$

$\beta_+$  and  $\beta_-$  corresponds to the RHCP and LHCP waves, respectively. Fig. A.1 also shows the three bands of operation; above resonance, resonance, and below resonance.

As a summary, the key factors to select the suitable ferrite material are the saturation magnetization factor and the magnetic DC bias, which subsequently determine the values of Larmor frequency and saturated magnetic frequency.

# Appendix B

## Mathematical Formulation of Dual Mode Double Ridge Waveguide OMT

The proposed OMT input is a square cross-section waveguide that supports two degenerate propagating modes (vertical and horizontal). The OMT achieves the separation of the two orthogonal propagating modes by using double ridge waveguide that can support two propagating modes after that two septums are used to separate these modes, each septum has a thickness of 0.254 mm. In other words, the main problem now is how to match the square cross-section waveguide to double ridge waveguide. Assuming that the propagating mode is  $TE_{10}$  in all waveguides (input and outputs), the operating frequencies are in between the cutoff frequency, and the next propagating mode frequency of both waveguides. The primary target now is finding the impedance of the input square waveguide and the output double ridge waveguide so that no reflections happen to the propagating signals. These calculations are done using mathematical formulations and presented in the next coming two sections.

### B.1 Square Waveguide Impedance Calculations

The input of the proposed OMT is a square waveguide, this means that the first impedance that can be calculated is the wave impedance  $Z_{TE}$  [8], and then the characteristic impedance, based on geometry shown in Fig. 4.2(a) considering that  $TE_{10}$  is the propagating mode, then the wave impedance is  $Z_{TE_{10}}$ .

$$Z_{TE_{10}} = \frac{\eta}{\sqrt{1 - \left(\frac{f_c}{f}\right)^2}} \quad (\text{B.1})$$

The cutoff frequency of the mode  $TE_{10}$  is:

$$f_{c10} = \frac{1}{2a\sqrt{\mu\epsilon}} \quad (\text{B.2})$$

The wave impedance  $Z_{TE_{10}}$  is different from the characteristic impedance. The characteristic impedance is a function of the waveguide geometry and the relation between the incident voltage and current. The characteristic impedance can be defined in terms of voltage, current, and power ( $Z_{VI}$ ,  $Z_{PV}$  and  $Z_{PI}$ ) [112]. The power voltage definition  $Z_{PV}$  is used here as a characteristic impedance and is given by:

$$Z_0 = Z_{PV} = \frac{2b_w}{a_w} Z_{TE_{10}} \quad (\text{B.3})$$

Where  $a_w$  and  $b_w$  are the waveguide width, and height, respectively.

## B.2 Double Ridge Waveguide Impedance Calculations

The output of the presented OMT is double ridge waveguide, so the impedance calculation is different from the conventional rectangular waveguides. The expressions for the cutoff frequency and the characteristic impedance of the double ridge waveguide has been presented by Cohn [113]. Based on the geometry shown in Fig. 4.2(b) where  $h$  and  $w$  are the half the gap height and the ridge width, respectively. The phases  $\theta_1$  and  $\theta_2$  are defined as:

$$\theta_1 = \frac{2\pi(a - w)/2}{\lambda'_c} \quad (\text{B.4})$$

$$\theta_2 = \frac{2\pi(w)/2}{\lambda'_c} \quad (\text{B.5})$$

where  $\lambda_c$  is the cutoff wavelength of the guide in the absence of the ridge, while  $\lambda'_c$  is the cutoff wavelength in the presence of the ridge. They can be related to each other by the following equation:

$$\lambda'_c = \frac{\pi/2}{\theta_1 + \theta_2} \lambda_c \quad (\text{B.6})$$

The double ridge can be modeled by three parallel admittances, an open-circuited line, a short-circuited line, and the discontinuity. This discontinuity has been modeled by Whinnery and Jamieson [114], it is denoted by  $B_c$ . The lowest root of the following equation is satisfied if the cutoff of the mode  $TE_{10}$  occurs, this leads to:

$$\frac{b}{h} = \frac{\cot \theta_1 - (B_c/Y_{01})}{\tan \theta_2} \quad (\text{B.7})$$

The impedance of the guide at the infinite frequency for TE<sub>10</sub> mode is:

$$Z_{0,\infty} = \frac{120\pi^2 h}{\lambda'_c [\sin \theta_2 + \frac{h}{b} \cos \theta_2 \tan \frac{\theta_1}{2}]} \quad (\text{B.8})$$

The impedance at any frequency as a function of  $Z_{0,\infty}$ , and  $\lambda'_c$  can be defined as:

$$Z_0 = Z_{0,\infty} \frac{1}{\sqrt{1 - \left(\frac{\lambda}{\lambda'_c}\right)^2}} \quad (\text{B.9})$$

Using (8) and (9) the initial value of the characteristic impedance of the double ridge waveguide can be estimated and calculated. The matching sections between the square waveguide input section and the double ridge waveguide output section are done using a regular Chebyshev matching problem. These matching sections are double ridge waveguides; they have impedances that can be expressed as a function of half the gap height  $h$  of the double ridge waveguide, using (8)  $h$  can be written as:

$$h = \frac{b \sin \theta_2}{\frac{120\pi^2 b}{Z_{0,\infty} \lambda'_c} - \cos \theta_2 \tan \frac{\theta_1}{2}} \quad (\text{B.10})$$

The dimensions of the transformer used for this matching problem are shown in Table 4.2 in Chapter 4.